RUPRECHT-KARLS-UNIVERSITÄT HEIDELBERG

Sebastian Weber

Studies and Improvements of the Bunch-crossing Identification for the ATLAS Level-1 Calorimeter Trigger

Masterarbeit

HD-KIP-16-116

KIRCHHOFF-INSTITUT FÜR PHYSIK

Department of Physics and Astronomy

University of Heidelberg

Master thesis

in Physics

submitted by

Sebastian Weber

born in Heilbronn

2016

Studies and Improvements of the Bunch-crossing Identification for the ATLAS Level-1 Calorimeter Trigger

This Master thesis has been carried out by Sebastian Weber

at the

Kirchhoff-Institute for Physics

under the supervision of

Herrn Prof. Dr. Hans-Christian Schultz-Coulon

Studien und Verbesserungen der Strahlkreuzungsidentifikation des ATLAS Level-1 Kalorimeter Triggers

Die Bestimmung der Strahlkreuzung (BCID) ist eine wichtige Aufgabe des ATLAS Level-1 Kalorimeter Triggers. Sie stellt sicher, dass für ein getriggertes Kollisionsereignis die richtige Detektorinformation ausgelesen wird.
In dieser Arbeit werden Fehlidentifikationen der Strahlkreuzung untersucht, welche für einige hochenergetische Kollisionsereignisse aufgetreten sind. Für diese Studien werden Elektronen und Photonen genutzt. Tritt eine Fehlidentifikation auf, geht die Detektorinformation für das betroffene Kollisionsereignis verloren. Um eine falsche BCID zukünftig zu verhindern, wurde eine neue Entscheidungslogik implementiert. Diese wird in der vorliegenden Arbeit mit Hilfe von Kalibrationssignalen der Kalorimeter validiert. Die erfolgreiche Validierung ermöglichte die Aktivierung der neuen Entscheidungslogik in ATLAS im April 2016.
Ebenfalls beschrieben wird die Validierung eines neuen und verbesserten Algorithmus für die BCID von saturierten Kalorimetersignalen. Es wurde festgestellt, dass dieser Algorithmus empfindlich für Nichtlinearitäten in der Pulsform der Kalibrationssignale bei hohen Energien ist, was eine korrekte BCID für diese Signale verhindert. Es konnte gezeigt werden, dass die Nichtlinearitäten in einer modifizierten Konfiguration des Algorithmus berücksichtigt werden können, sodass er über den kompletten Energiebereich korrekt funktioniert.
Der neue, verbesserte BCID Algorithmus wird seit Oktober 2016 erfolgreich in ATLAS eingesetzt.

Studies and Improvements of the Bunch-crossing Identification for the ATLAS Level-1 Calorimeter Trigger

The Bunch-crossing identification (BCID) is a crucial task of the ATLAS Level-1 Calorimeter Trigger. It ensures that the correct detector information is read out for a triggered event.
In this thesis misidentifications of the bunch-crossing for several highly energetic events are investigated using energy depositions from electrons and photons in the calorimeter. The misidentifications cause the loss of detector information for the affected events and have to be avoided. The solution implemented to prevent the wrong BCID, called „the new decision logic“, is validated using calibration pulses generated by the calorimeter calibration system. The results of this validation allowed for the new decision logic to be activated for ATLAS physics data taking in April 2016.
This thesis also describes the validation of a new, improved BCID algorithm for saturated calorimeter signals. It was found that the algorithm is sensitive to non-linearities in the shape of the calibration pulses at high energies. This prevents a correct BCID for those pulses. It could be shown that the algorithm configuration can be modified to take the non-linearities into account. In this way a correct BCID is guaranteed over the whole energy range.
The new, improved BCID algorithm was successfully activated for ATLAS data taking in October 2016.

Contents

1 Introduction

The Large Hadron Collider (LHC) at CERN is the most powerful particle accelerator ever built. It allows to study the fundamental particles at unprecedented energies and might open a windows to new physics. The LHC collides proton bunches with a frequency of 40 MHz and in each collision 25 interactions take place on average. This corresponds to an interaction rate of 1 GHz. For the ATLAS detector the raw event size is about 1 MB, which leads to a data volume of 1 PB that is produced at the LHC every second.

The recording capabilities to permanent storage available today however, are not able to cope with this amount of data and the rate at which it is produced. Only one in 10^6 events can be recorded. Therefore, it is necessary to select those events that are interesting for physics analyses and that could lead to new discoveries. To achieve this selection, the ATLAS experiment has implemented an efficient and reliable trigger system.

This trigger system has two levels. The first level (Level-1) is based on fast, custom-built hardware and uses information from the calorimeters and the muon detectors. The Level-1 trigger decision is taken within 2.5 µs. During this time the complete event information recorded by the detector is stored in buffers. The second trigger level is called High Level Trigger. It is software based and can use the full detector information in combination with offline algorithms to provide a final selection of events to be recorded to disk.

The Level-1 Calorimeter Trigger (L1Calo) is a main component of the ATLAS trigger system. It operates on calorimeter information with reduced granularity to identify significant energy depositions. A very important step is the association of these energy depositions to the correct LHC collision event. This procedure is called bunch-crossing identification (BCID). When an event is triggered on Level-1, the information corresponding to the identified bunch-crossing is read out from the buffers. If the wrong bunch-crossing is identified, the detector information for the triggered event is lost.

The BCID is a challenging task, since the calorimeter signals are several bunch-crossings wide. For low energy depositions the BCID consists in finding the peak in a digitized calorimeter signal. This is accomplished by a finite-impulse-response (FIR) filter in combination with a peakfinder algorithm. For high energy depositions, typically above 256 GeV, the analogue-to-digital converters that digitize the calorimeter signal, start to saturate. In case of saturation the peak of the signal is no longer visible and the peakfinder algorithm cannot be used. Instead, a dedicated saturated algorithm that operates on the rising edge of the pulse is employed.

Until the upgrade of the ATLAS detector in 2014 the ASIC based "Multi Chip Module" was responsible for the digitization of the calorimeter signals and the BCID. During the upgrade it was replaced by the FPGA based "new Multi Chip Module" (nMCM), which implemented several improvements. Amongst others, a novel type of filter coefficients for the FIR, called autocorrelation coefficients and an enhanced threshold algorithm for saturated BCID were introduced.

The use of the autocorrelation coefficients caused a wrong BCID by the peakfinder for around 120 events, containing high energy physics objects. Consequently most of the detector information was lost for the affected events. This problem was termed "peakfinder mistiming" and it is related to the saturated pulses caused by the high energy physics objects. Since these objects are especially interesting for physics analyses, a study of the peakfinder mistiming was

conducted as part of this thesis.

To solve the peakfinder mistiming the firmware of the nMCM was modified. A new decision logic was introduced that allows for the peakfinder decision to be ignored for highly saturated pulses and to rely on the saturated algorithm alone. As part of this thesis the new decision logic was validated for use in physics data taking. The validation was performed using the calorimeter calibration system, which is able to inject test pulses into the calorimeter electronics.

The calorimeter calibration system was also used to study the performance of the new enhanced threshold algorithm for saturated BCID. These studies were part of the commissioning effort that lead to the activation of the new algorithm for ATLAS physics data taking in October 2016.

An important tool used in the operations of L1Calo at CERN is the monitoring. It is accessible for shifters and system experts and gives detailed information about the status of L1Calo. The monitoring also includes a complete simulation of the L1Calo hardware related to the BCID. As part of this thesis several contributions to the monitoring and the simulation were made.

The first chapter gives a brief introduction to the LHC and its main experiments. In the second chapter the ATLAS detector is described with the focus on the inner tracking system and especially the calorimeters. A detailed description of L1Calo is presented in the third chapter with special emphasis on the BCID. The fourth chapter offers an overview of the reconstruction and identification of electrons and photons with the ATLAS detector. In the fifth chapter the analysis of the PeakFinder mistiming, using physics data, is presented.

The sixth chapter has two main parts. In the first part, the PeakFinder mistiming is reproduced using the calorimeter calibration system. The second part describes the validation of the new decison logic with this system. In the seventh chapter the attempt to validate the enhanced threshold algorithm for saturated pulses is described. The chapter also contains the current status of pulse shape studies, which are still ongoing. The eighth chapter presents the contributions to the monitoring of L1Calo. In the ninth chapter a summary of the thesis is given.

2 The Large Hadron Collider

The Large Hadron Collider (LHC) is the most powerful particle accelerator ever built. After 24 years of design and construction the LHC began operation in 2009. It is located at the headquarters of the European Organization for Nuclear Research (CERN) in the canton of Geneva, Switzerland. Built in the circular tunnel originally constructed for the Large Electron Positron Collider (LEP), the LHC has a length of 26.7 km and is situated between 45 m and 170 m below the surface. The machine is designed to reach a center of mass energy of 14 TeV in proton-proton collisions, thanks to its superconducting magnet technology. During 2016 luminosities of up to $L = 1.37 \times 10^{34}\,\mathrm{cm}^{-2}\mathrm{s}^{-1}$ were delivered to two of the four main experiments ATLAS and CMS located around the ring, exceeding the design luminosity of $L = 10^{34}\,\mathrm{cm}^{-2}\mathrm{s}^{-1}$. For the remaining experiments LHCb and ALICE lower luminosities are required. Collisions of heavy ions are also possible with a luminosity of $L \approx 10^{27}\,\mathrm{cm}^{-2}\mathrm{s}^{-1}$ and a beam energy of 8.16 TeV per nucleon pair [1].

2.1 Preaccelerators and Beam Properties

Particles injected into the LHC have already been preaccelerated. The injector chain for protons is formed by a linear accelerator (Linac 2), the Proton Synchrotron Boosters (PSB), the Proton Synchrotron (PS) and the Super Proton Synchrotron (SPS), as shown in Figure 2.1. The first three stages form the PS complex that has been in operation since 1959 [2, 3], whereas the SPS became operational in 1976. For heavy ion injection Linac 3 is used in combination with the Low Energy Ion Ring (LEIR) [4] followed by PS and SPS. To serve as injectors for the LHC, the preaccelerators had to undergo major upgrades [5].

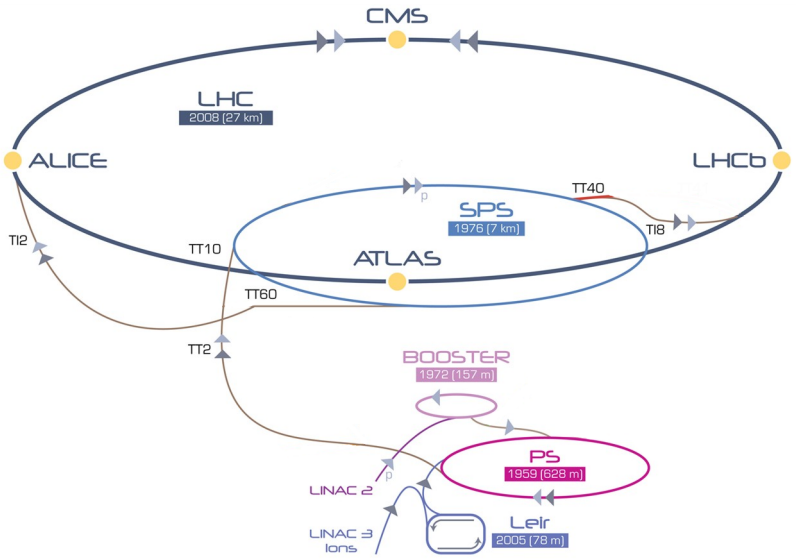

Figure 2.1: The CERN accelerator complex: The LHC injector chain, the LHC and the main experiments ATLAS, ALICE, CMS and LHCb [6].

In the linear acceleration stage the protons gain an energy of 50 MeV and then further 1.4 GeV in the four rings of the PSB. The PS provides acceleration to 25 GeV and generates the basic LHC bunch structure, a train of proton bunches with a spacing of usually 25 ns. Each bunch contains around 10^{11} protons, depending on the filling scheme [7]. Finally the SPS accelerates the protons to an energy of 450 GeV and injects them into the two LHC rings [8]. Several fills of each machine in the injection chain are needed to fill the subsequent accelerator and finally the LHC which can contain up to 2808 proton bunches [1]. Two proton beams circulate the machine in opposite direction and are crossed at four points around the ring, to produce the collisions for the experiments, as shown in Figure 2.2. A "bunch crossing" (BC) typically happens every 25 ns, depending on the bunch spacing. This leads to a collision frequency of 40 MHz. The location of beam crossing defines the Interaction Point (IP). A small crossing angle as opposed to head-on collisions guarantees the absence of unwanted collisions near the IP. However during a BC usually more than one p-p collision takes place. The number of p-p collisions during one BC is called pile-up or physics background and is denoted by μ. At design luminosity an average pile-up of $\langle\mu\rangle = 23$ is expected, but this value has already been exceeded.

2.2 Detectors and LHC Insertions

The schematic layout of the LHC is shown in Figure 2.2. The two general purpose experiments ATLAS [9] and CMS [10] are located opposite each other at Point 1 (P1) and Point 5 (P5) in the corresponding octants. They are designed to record high luminosity in proton-proton and Pb-Pb running and aim at the discovery of new phenomena at the TeV scale. These include amongst others the search for new gauge bosons, supersymmetric particles, quantum gravity and miniature black holes. However, the benchmark process used to establish the performance of these detectors, was the search for the (Standard Model) Higgs Boson. It was discovered by both experiments in 2012 [11].

The more specialized experiments ALICE [12] and LHCb [13], are located at Point 2 (P2) and Point 8 (P8). ALICE is a heavy-ion experiment with its main focus on the strong interaction of the Standard Model and the quark-gluon plasma that is produced in the Pb-Pb collisions at the LHC. Accordingly the detector is designed for high particle multiplicity and has excellent particle identification capabilities. LHCb focuses on heavy flavor physics especially concentrating on particles containing beauty and charm quarks. The physics motivation is the very precise measurement of CP violation that might receive contributions from physics beyond the the Standard Model, as well as rare decays of B and D mesons. In order to detect the decay of long-lived B mesons, the detector has an excellent vertex resolution. Different from ATLAS and CMS, LHCb aims to operate at the lower luminosity of $L \approx 2 \times 10^{32}\,\mathrm{cm}^{-2}\mathrm{s}^{-1}$, in order to reduce pile-up and radiation damage. The reduced luminosity is achieved by changing the beam focus at the IP.

P2 and P8 also contain the injection system for beam 1 and beam 2 respectively, where beam 1 circulates clockwise and beam 2 counterclockwise. Beam collimation is performed at P3 and P7. P3 contains the momentum cleaning system of the beams. It uses primary collimators to scatter particles with too high momentum offsets into secondary collimators where they are absorbed. At P7 "betatron cleaning" takes place. Betatron oscillations appear when particle

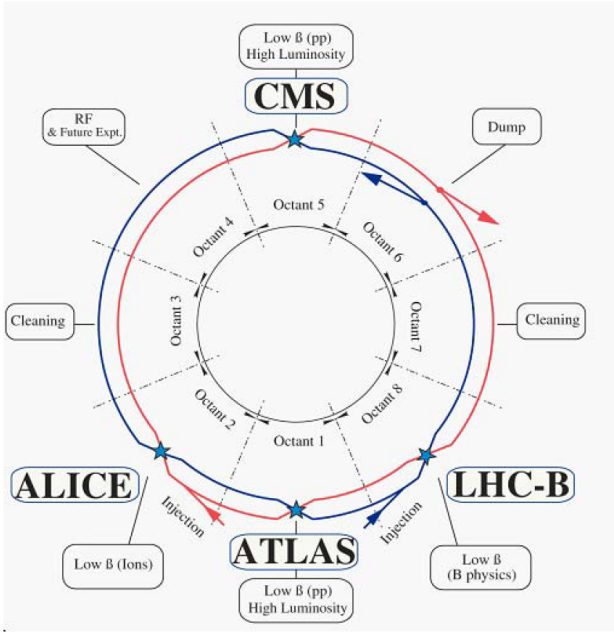

Figure 2.2: Schematic layout of the LHC and the main insertions. Each octant contains a cavern either for an experiment or for beam utilities. The experiments are located at P1, P2, P5 and P8, where the beams are crossed and collisions are produced [1].

trajectories deviate from the primary circular orbit. The magnetic fields provide a restoration force that leads to oscillations around the primary orbit. If the amplitude of these oscillations becomes too large, the particles are removed from the beam by the collimators. The actual acceleration in the LHC happens in the radio-frequency (RF) system at P4. It houses the 400 MHz superconducting RF cavities, as well as the klystrons that produce approximately 4800 kW RF power in total. The beam dump system is located at P6. The energy of over 350 MJ stored in the beam would suffice to melt half a ton of copper. A situation where the beam becomes unstable could lead to severe damage to the LHC or the experiments. Therefore the beam dump system is designed to extract the beams from the accelerator very fast and lead them into a nearly 8 m long carbon absorber.

2.3 Magnets and Cryo-System

The LHC magnet system relies on superconducting technology to produce the field strength necessary to keep the high energetic particles on their tracks. NbTi Rutherford cables are used to wind the electromagnetic coils and they are cooled by superfluid helium to approximately 1.9 K. This setup allows for field strengths above 8 T. Figure 2.3 shows a section of one of the 1232 main “cryo dipoles”. Both beam pipes are integrated into one cold mass and cryostat. This “twin-bore” design was necessary because of the limited space in the LEP tunnel. It complicates the magnet structure as the two beam lines are so close that they become coupled both mechanically and magnetically. All components that need to be cooled by superfluid helium

are contained in the cold mass. In addition to the the beam pipe, these are the superconducting magnet coils, the iron return yoke for the magnetic flux and the actively cooled beam screen. The screen is necessary to shield the cryogenic system from heat sources, like synchrotron light and image currents. This is especially important to prevent quenches in the magnets.

A quench happens when a magnet heats up and looses its superconductivity. This return to the normal-conductive state leads to a strong increase in resistance and consequently to high temperatures that can destroy the magnet. In case of a quench happens in a magnet, dedicated heaters bring the other magnets to the normal-conductive state to spread the energy release over a larger volume and reduce the maximum temperature.

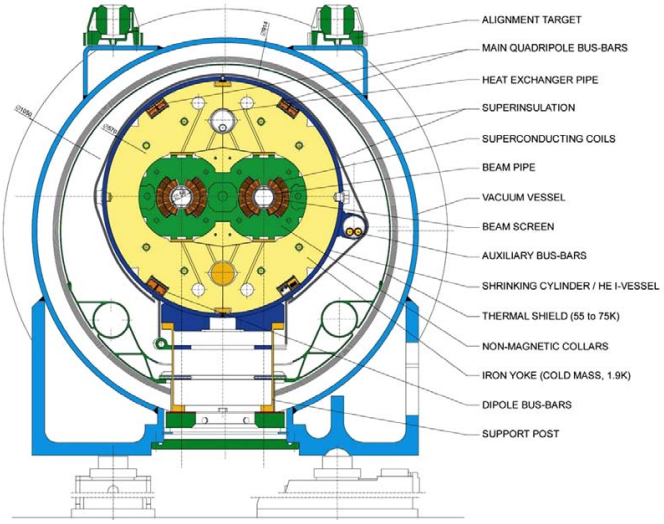

Figure 2.3: Schematic of a LHC cryo dipole. Both beam pipes are contained in a single cold mass, due to space constraints in the LHC tunnel. All components cooled by superfluid helium are contained in the cold mass [1].

2.4 LHC Run Schedule

The LHC is not operated continuously but run periods are interleaved with long shutdowns (LS) where improvements and repairs for detectors and the accelerators are applied. The run schedule since the the start of operations in 2009 is shown in Figure 2.4. The official start of the LHC operations was in September 2008. However an accident only nine days later required one year of repairs. Therefore actual the Run 1 started only in November 2009.

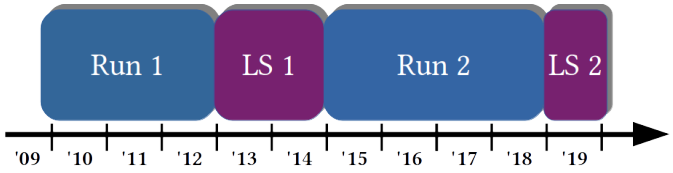

Figure 2.4: Run schedule of the LHC until the end of LS2.

3 The ATLAS detector

ATLAS (A Large Toroidal ApparatuS) is a general purpose particle detector, which is located at the CERN Large Hadron Collider [9]. It is designed for the discovery of new phenomena at the TeV scale. To observe rare events such as the Higgs boson ($\sigma = 5.6 \times 10^1$ pb at $\sqrt{s} = 13$ TeV), a high luminosity is required that in turn brings challenges in operating the detector. The high collision rate of 40 MHz requires fast detection components and electronics that have to be radiation-hard to perform well during the lifetime of the experiment. The particle multiplicity in proton-proton collisions is high, on the order of 1000 charged particles, and requires fine detector granularity and good particle identification capabilities. Full 4π calorimetry coverage is necessary for measurements of missing transverse energy $\not{E}_T$ and jet multiplicities that play an important role in many experimental signatures. The QCD jets copiously produced in proton-proton collisions, due to their high cross-section, present a very large background for physics analyses and require very efficient triggering and event selection.

The ATLAS detector shown in Figure 3.1 is forward-backward symmetric with respect to the nominal IP, which is also the origin of the coordinate system. The z-axis points along the beam, while the x-axis points towards the center of the LHC ring and the y-axis points upwards. The transverse plane is defined to be spanned by the x- and y-axis. Usually angular coordinates are used to describe the detector, due to its rotational symmetry. The azimuthal angle ϕ is measured around the z-axis and the polar angle θ is measured from the z-axis. Typically the polar angle is expressed as the pseudorapidity η, where

$$\eta = -\ln \tan\left(\frac{\theta}{2}\right). \tag{3.1}$$

The outer dimensions of the ATLAS detector are determined by the muon spectrometer. It is formed by an air-core toroid system consisting of a long barrel magnet with two inserted endcaps and three layers of high precision tracking chambers. The magnet system has been chosen to provide strong fields up to 1 T with the return yoke in air to minimize multiple scattering. The ATLAS calorimetry is based on high granularity sampling calorimeters using Liquid Argon technology as well as scintillating tiles. It is placed inside the muon spectrometer. The innermost part of the detector is the tracking system that is immersed in a 2 T magnetic field and provides very fine granularity to cope with the very large track density close to the IP. Both the calorimetry and the tracking system are covered in more detail in the following sections, since they play an important role for the studies presented here.

3.1 The Inner Tracking System

The ATLAS tracking system consists of three independent tracking sub-detectors and the central solenoid, a magnet with a 2 T axial field. The detectors, namely Pixel, Semi-Conductor Tracker (SCT) and Transition-Radiation-Tracker (TRT), all consist of a barrel and two endcap parts as can be seen in Figure 3.2. Together they form the Inner Detector (ID) [14]. The central solenoid has barrel shape and is placed around the ID, however inside the Liquid Argon cryostat to reduce the material budget. The magnet is superconducting and uses a single-layer coil made from NbTi. The hadronic calorimeter and its support structure work as the return yoke.

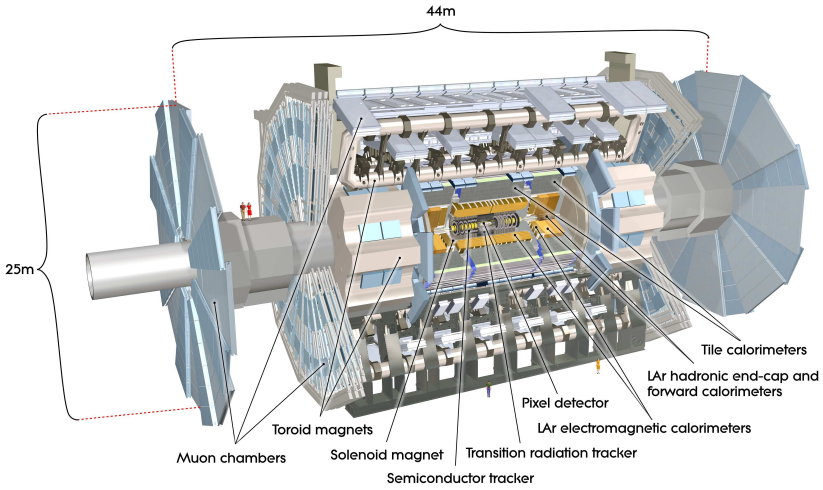

Figure 3.1: Schematic layout of the ATLAS detector [9].

The magnetic field is used for the measurement of the transverse momentum p_T of charged particles. Their tracks are bent by the Lorentz's force and p_T can be determined from the bending radius R by

$$p_T = 0.3BR, \tag{3.2}$$

where the magnetic field strength B has to be known accurately. For a precise measurement of R it is necessary to have a sufficient number of track points and to be able to distinguish the track points for different particles. The reconstructed tracks are used to determine the primary and possible secondary interaction vertices. This is important for background rejection and B physics studies.

The highest track density is present directly at the IP. For this reason the innermost part of the ID is a pixel detector in the region $|\eta| < 2.5$ that was initially installed with three layers. The pixels sensors are made of n-type silicon with a thickness of 250 µm and the pixels on the sensors have mostly dimensions of 50 µm^2 $\times$ 400 µm^2. The pixel detector provides discrete space-point resolution with over 80 million readout channels. To achieve this high density, the front-end readout is performed directly on the chip where the pixels are connected via bump-bonding-technique. During LS1 a fourth pixel layer, the Insertable B-Layer (IBL), was installed [15].

Around the pixel detector, four layers of stereo pairs of silicon microstrip sensors form the SCT that covers $|\eta| < 2.5$. The strips have a length of 12 cm and a width of 80 µm and only require one readout link, thus reducing the complexity of the readout. The strip pairs are stacked and rotated with respect to each other. The position information is gained from the crossing point of two hit strips.

The outer sub-detector of the ID is the TRT which extends up to $|\eta| < 2$. It uses drift tubes, called straw tubes, with a diameter of 4 mm, surrounded by polypropylene fibers to detect energy loss of passing particles as well as low energy transition radiation photons for tracking.

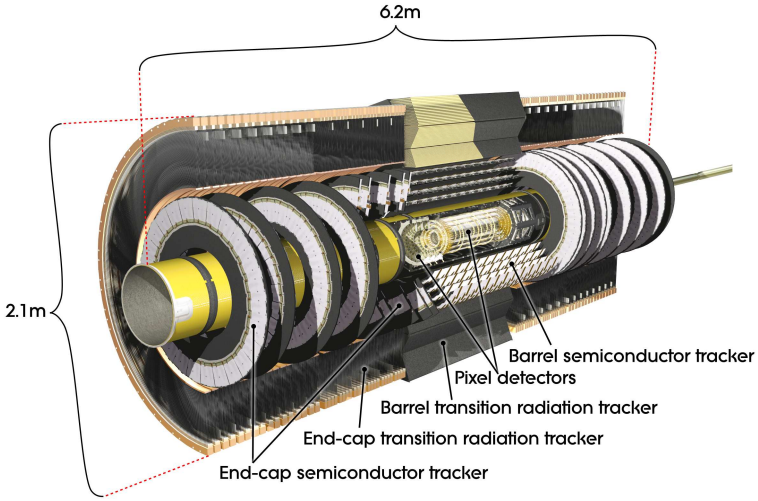

Figure 3.2: Schematic layout of the ATLAS inner detector [9].

The straw tubes are filled by a gas mixture of Xe, CO_2 and O_2 and are arrayed in up to 73 layers. The TRT can be used to identify electrons up to energies of 150 GeV and discriminate them from heavier particles like pions. This can be understood by considering the energy of the transition radiation photons for a particle with mass m. It is given by

$$E \approx \gamma \hbar \omega_p, \tag{3.3}$$

with the plasma frequency

$$\omega_p = \sqrt{\frac{1}{m}}. \tag{3.4}$$

To be detectable, the transition radiation photons have to be at least in the X-ray energy range, since they would otherwise be absorbed in the passive material. As the plasma frequency is inversely proportional to $\sqrt{m}$, the onset of the transition radiation for heavier particles requires higher energies. When an electron passes through the TRT it deposits energy via transition radiation photons in addition to the energy loss by ionization. This makes the distinction to other particles possible [16]. On average the TRT contributes with 36 hits to a track, compensating for its lower resolution as compared to the silicon detectors.

3.2 ATLAS Calorimetry

The ATLAS detector uses sampling calorimeters that provide coverage up to $\eta = 4.9$ and full coverage in ϕ. The calorimetry is divided into two parts as shown in Figure 3.3. The inner part is the electromagnetic calorimeter which is designed for the measurement of electromagnetic particles. The showers produced by hadronic particles, also called "jets", are not so easily absorbed and they deposit the largest part of their energy in the surrounding hadronic

calorimeter, mainly by the strong interaction. More information on the showers produced by electromagnetic particles can be found in Section 5.

Both calorimeters are constructed from interleaved layers of passive high-Z absorber material that induces the particle showers and an active material that samples the energy deposition of the charged shower components. The advantage of the sampling technique, with respect to the exclusive use of active material, is a compacter design at usually lower cost. However sampling fluctuations lead to a slightly reduced energy resolution [17]. The ATLAS calorimeters use different combinations of absorber and active material, the details are discussed in the next section. Apart from a precise energy measurement, calorimeter information is also used for triggering. The calorimeters deliver fast but reduced readout information to the Level-1 Calorimeter Trigger (L1Calo), described in more detail in Section 3.2.3 and Section 4.

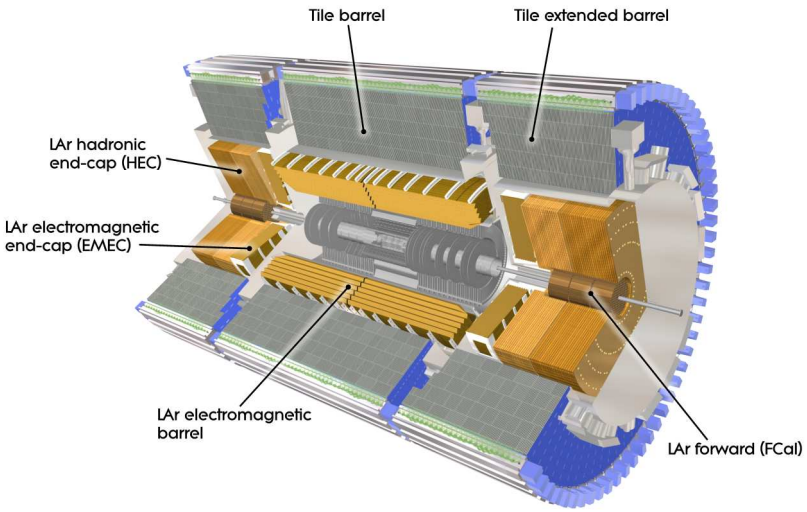

Figure 3.3: Schematic layout of the ATLAS Calorimeter [9].

3.2.1 The Electromagnetic Calorimeter

The electromagnetic calorimeter is entirely based on Liquid Argon (LAr) as active material and lead as absorber. The absorbers and the electrodes have an accordion geometry to provide full coverage in ϕ without cracks. In addition, the accordion shape enables fast charge collection and extraction of the signal, which is necessary for the high rate environment at the LHC.

The calorimeter is split in a barrel part (EMB) and two endcaps (EMEC) [18] as shown in Figure 3.3. The barrel extends up to $|\eta| < 1.475$ and the end caps cover the region $1.375 < |\eta| < 3.2$. Each EMEC is divided into two parts. The outer wheel for $1.375 < |\eta| < 2.5$ and the inner wheel for $2.5 < |\eta| < 3.2$. Calorimetry in higher η regions ($3.1 < |\eta| < 4.9$) is covered by the forward calorimeter (FCal). A presampler is installed for $|\eta| < 1.8$ to estimate the energy loss due to material in front of the electromagnetic calorimeter. The EMB and the EMEC outer wheel match the ID and constitute the high-precision physics region ($|\eta| < 2.5$)

with higher granularity and three layers that is used for central electron identification (c.f. Section 5).

Figure 3.4 shows a sketch of a barrel module. The accordion shape is clearly visible as well as the different layers, with varying thickness and granularity. The first layer has the highest segmentation ("strips") to provide an accurate shower position measurement, the second layer contains the bulk of the shower and the third layer is used to measure the tail. The overlap region around $|\eta| = 1.4$ between EMB and EMEC is an exception and has coarser granularity and only two layers. It is usually excluded from physics analyses [19]. The EMEC inner wheel is divided in two layers with coarser granularity as well. The thickness of the calorimeter is chosen to be at least 22 radiations lenghts X_0. This ensures that even high energetic electromagnetic showers are contained [20].

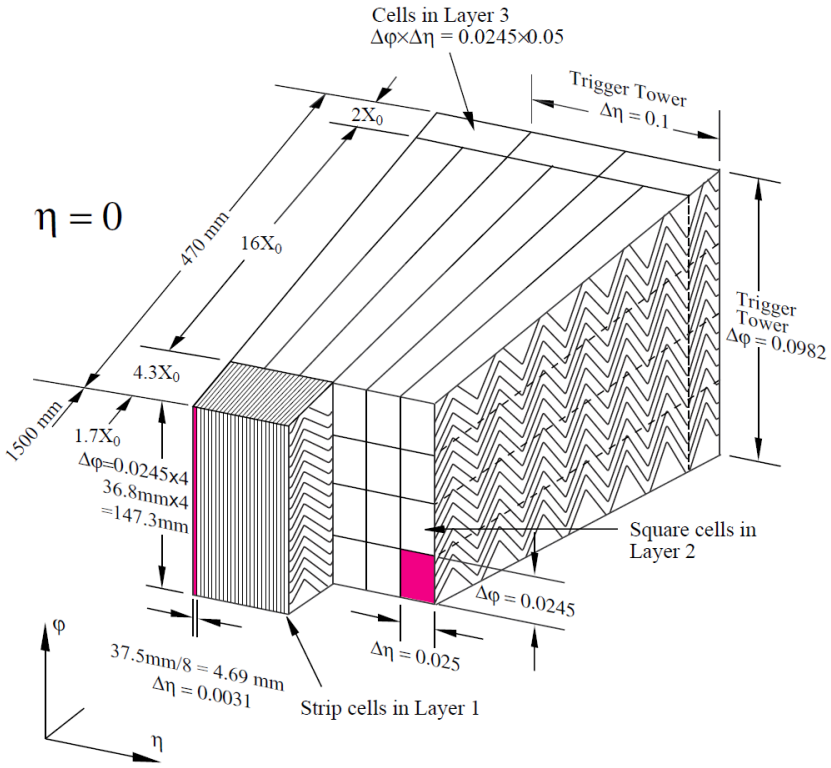

Figure 3.4: Schematic layout of a Liquid Argon barrel module. The different layers and granularities are shown, as well as the accordion structure of the absorbers and readout electrodes. The cells inside a wedge of roughly $\Delta\eta \times \Delta\phi = 0.1 \times 0.1$ form a trigger tower and their output is summed to give one of the input signals of the Level 1 Calorimeter Trigger [9].

3.2.2 The Hadronic Calorimeter

The hadronic calorimeter is split into three parts, the Tile Calorimeter (Tile), the Hadronic End-Cap Calorimeter (HEC) and the Forward Calorimeter (FCAL). The region $|\eta| < 1.7$ is covered by the Tile calorimeter. It is seperated into a barrel part ($|\eta| < 1.0$) and an extended barrel part ($0.8 < |\eta| < 1.7$) and relies on scintillating tiles as active medium and steel plates as absorber. The scintillation photons are read out via wavelength shifting fibres and photomultiplier tubes (PMT). This comparably less expensive technology allows for a high radial depth of 7.2 hadronic interaction lengths λ for the Tile calorimeter [21]. The HEC and FCAL share a cryostat with the EMEC and use Liquid Argon as active medium. The HEC covers the η region $1.5 < |\eta| < 3.2$. It relies completely on copper absorbers and overlaps with the FCAL and the Tile calorimeter. The FCAL spans $3.1 < |\eta| < 4.9$ and is closest to the beam. It has three layers stacked in beam direction. The innermost layer is equipped with copper absorbers and optimized for electromagnetic showers, whereas the outer two layers use tungsten absorbers and are used for hadronic measurements [22].

3.2.3 Liquid Argon signal generation and readout

The signal produced by the LAr calorimeter is due to ionization. When charged particles traverse the LAr, they loose energy and ionize the Argon atoms. The number of electrons freed in this process is proportional to the energy deposition. In the electric field between the accordion shaped electrodes the ions and the free electrons are separated and drift towards the electrodes in approximately 450 ns, thereby inducing a voltage. Since the drift velocity is constant, this induced voltage will decrease linearly with time, yielding the typical triangular signal pulse shape shown in Figure 3.5.

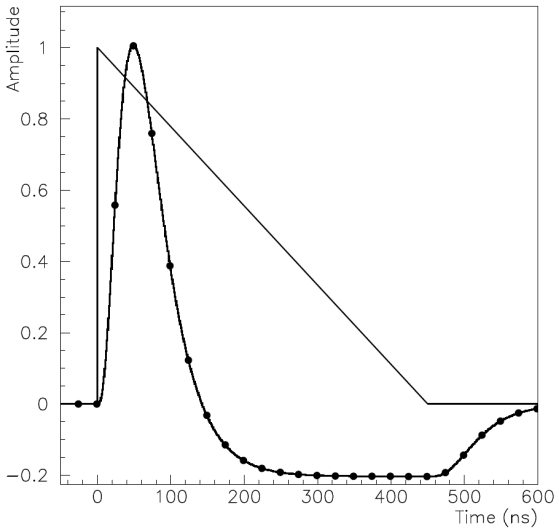

Figure 3.5: Physical pulse of a LAr electromagnetic barrel cell with typical triangular shape. Overlayed is the same pulse after shaping with sampling points every 25 ns [23].

The energy deposition of the incoming particle could be extracted directly from this pulse. In practice however the pulse is first processed by shaper electronics. This has several reasons. Firstly the signal has a very long tail that spans several BCs. It is caused by the lower drift velocity of the ions as compared to the electrons, due to their higher mass. Therefore the collection of the complete charge takes a long time. This tail is removed by differentiating the signal in the shaper. Secondly the analogue signal is not a perfect triangle, but overlayed by fluctuations due to electronic noise. This noise is reduced in two integration steps. A longer integration time generally leads to lower electronic noise. However it increases pile-up noise, since the time between two collisions is much smaller than the time needed for signal collection. Therefore pulses from subsequent collisions are overlayed with the still decaying pulses from previous collisions. A longer integration "collects" more of this pile-up. The relation between electronic and pile-up noise and the dependence on the integration time are shown in Figure 3.6.

The output of the shaper is a bi-polar signal. It is depicted in Figure 3.5. The information of the original signal amplitude is contained in the peak after a typical rise time of 50 ns. Notice also the long undershoot of the signal. In case of ideal shaper electronics, the area spanned by the peak is equal to the area spanned by the undershoot, due to charge conservation.

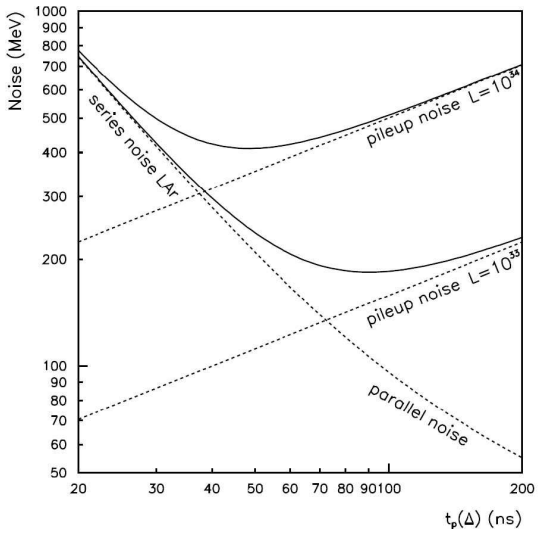

Figure 3.6: Dependence of different noise sources on the integration time. Note the strong dependence on the luminosity L [24].

The LAr signal processing takes place on the Front-End-Boards (FEBs) that are located very close to the calorimeter just outside the LAr cryostat. A block diagram of the overall LAr readout electronics including the FEB is shown in Figure 3.7. After preamplification the signal path to L1Calo is separated from the rest of the LAr processing and data acquisition, for which more information can be found in [25].

The focus of the remaining section is on the readout to L1Calo. The raw calorimeter signals are shaped as described above by a bipolar $CR-(RC)^2$ analogue filter. Each shaper processes the input signals from four calorimeter cells. As discussed in Section 4 L1Calo operates on the summed input signals from all cells in projective trigger towers. The first step of the summation

is done in the shaper by the linear mixer, which adds the four shaped signals. The next adding step happens in the Layer Sum Boards (LSB). Each LSB sums the output of all linear mixers belonging to one calorimeter layer within one trigger tower. The outputs for the different layers are then summed in the Tower Builder Board (TBB) to give the final input signal to L1Calo [25, 26, 27].

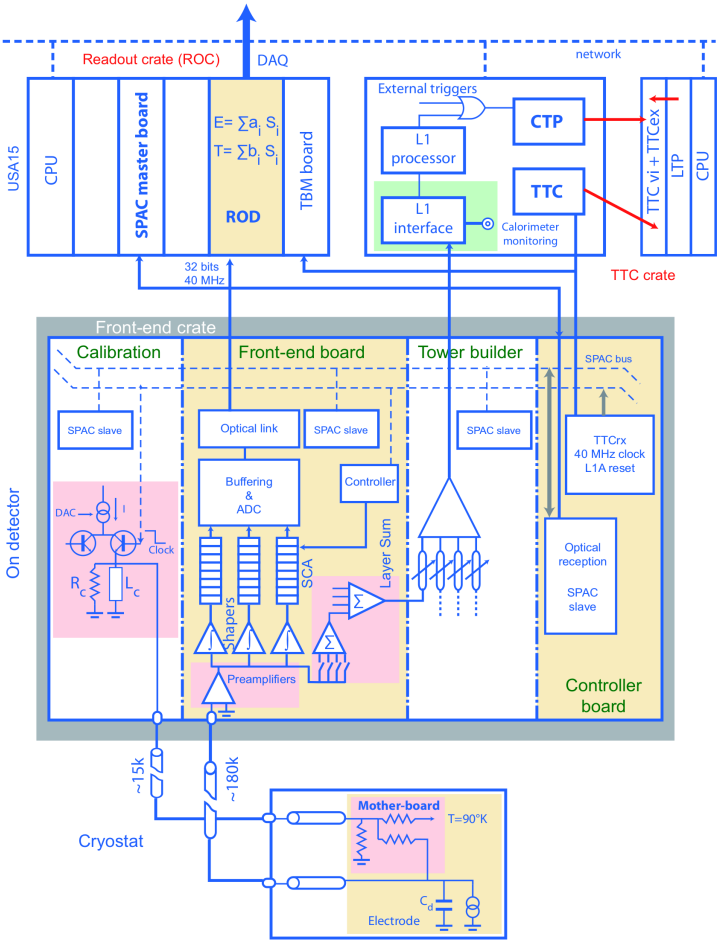

Figure 3.7: Schematic of the Liquid Argon readout from the detector electrodes to data acquisition (DAQ) and L1Calo [26].

3.2.4 The LAr Calibration System

To convert the electrical signal current measured in µA to an energy in units of GeV a precise calibration is necessary. Initially these conversion factors are determined from simulation and test beam measurements [28]. However during the operation of the fully assembled calorimeter a constant monitoring and calibration is necessary [20]. For this purpose the LAr calorimeter is equipped with an electronics calibration system. The pulses produced by this

system are directly delivered to calorimeter electrodes. This is necessary because the shaping scheme described above makes the pulse sensitive to the time dependence of the ionization signal. To correctly model this, a voltage pulse, designed to be similar to the physics pulse, is applied across an injection resistor R_{inj} on the electrodes. This calibration pulse is however not triangular as the physics pulse shown in Figure 3.5, but exponential, as shown in Figure 3.8.

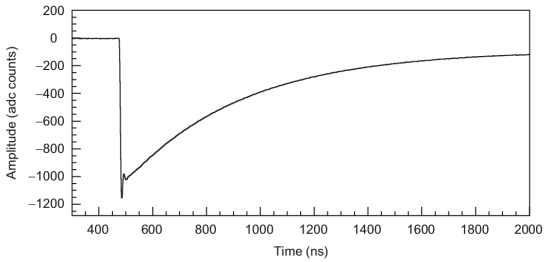

Figure 3.8: Shape of voltage pulse as injected by the LAr calibration system [29].

The pulses are guaranteed to have an integral linearity with energy of better than 0.1 % up to 3 TeV [29]. The peak height is expected to behave linear at least up to 256 GeV [30]. This is important for the L1Calo calibration. Other properties of the pulse, like its height at points before and after the peak, are not necessarily linear with energy. After injection in the electrodes the calibration pulses go through the normal LAr readout chain and also through LSB and TBB to L1Calo. A typical calibration pulse after shaping and readout via the LAr readout chain is shown in Figure 3.9.

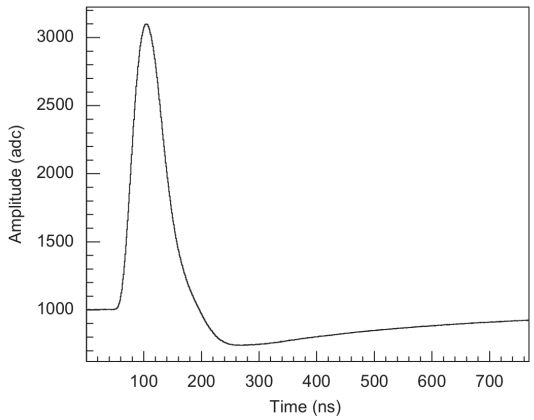

Figure 3.9: Pulse of the LAr calibration system after shaping [29].

3.3 The ATLAS Trigger System

An enormous amount of information is produced in the collisions at the LHC every second. At design luminosity the interaction rate is around 1 GHz, whereas the event data recording capabilities are limited to around 1 kHz. For this reason a highly efficient trigger system is

necessary to provide the needed rejection factor of 10^6, while keeping the interesting physics events. To accomplish the rate reduction ATLAS uses a two-tier trigger, the Level-1 Trigger (L1) and the High-Level Trigger (HLT) that perform a stepwise rate reduction, enriching the stored dataset with interesting physics events. The Run 2 setup of the trigger system is shown in Figure 3.10.

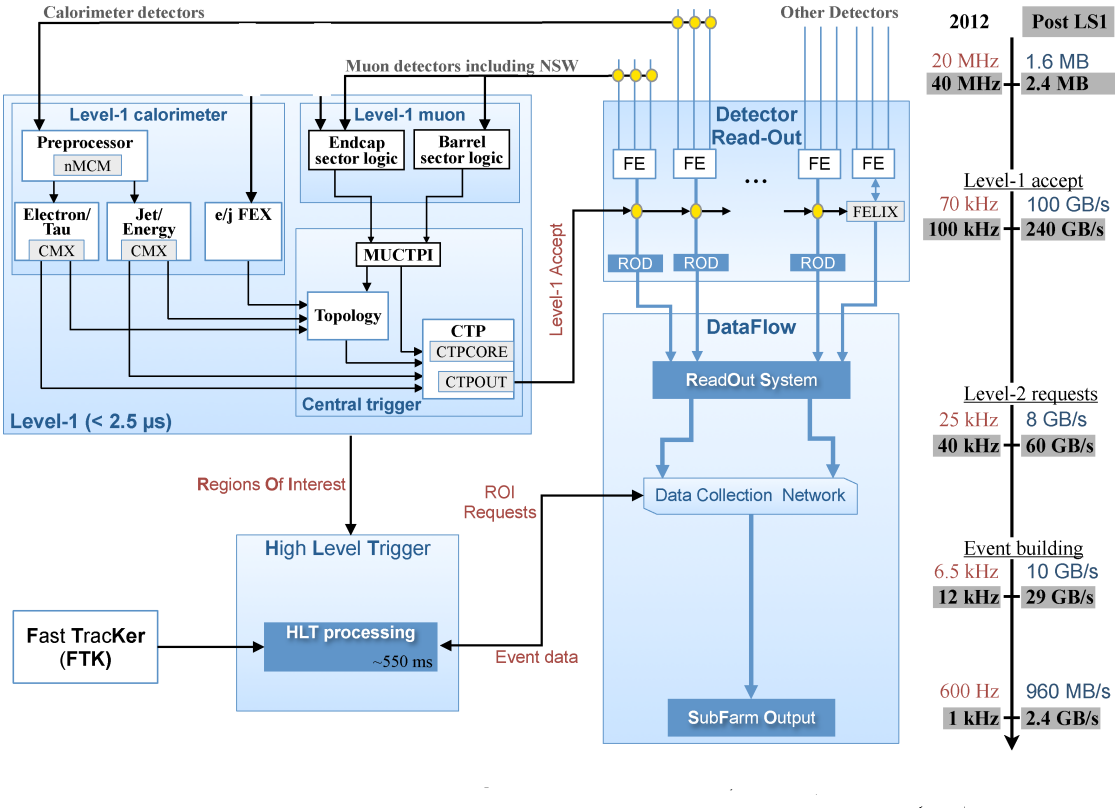

Figure 3.10: The ATLAS Trigger and DAQ System used in Run 2. Adapted from [31].

In a first stage L1 employs custom built, highly parallelized hardware which processes reduced detector information to bring the data rate down to 100 kHz. It is mainly formed by three subsystems, the Level-1 Calorimeter Trigger (L1Calo), the Level-1 Muon Trigger (L1Muon) and the Central Trigger Processor (CTP). L1Calo searches for jets, electromagnetic clusters, τ leptons, missing transverse energy and total energy. L1Muon uses Resistive Plate Chambers (RPC) and Thing-Gap Chambers (TGC) to trigger on muons with high transverse momentum. The time limit for the L1 decision is 2.5 µs. In addition to the readout to data acquisition (DAQ), L1Calo and L1Muon produce so-called Regions-of-Interest (RoI), which contain details of found objects and their coordinates. These are used to seed the HLT.

The HLT uses a farm of over 6000 commercial computers to process the full detector information for L1 seeded events with offline reconstruction algorithms to make a final decision. This can take up to 4 s per event. During the selection process, the event data from the different sub detectors is stored in pipeline buffers, from where it can be accessed by the HLT. The

selected events are then assembled and moved to permanent storage. In the original ATLAS design the HLT was split into two disjunct computing farms, the Level-2 trigger (L2) and the Event filter. During the LS1, both were integrated into the HLT [9, 31, 32].

4 The Level-1 Calorimeter Trigger

The Level-1 Calorimeter Trigger (L1Calo) is one of the main components of the ATLAS trigger system, as explained in the previous chapter. An overview of the Run 2 of L1Calo and its components is shown in Figure 4.1. Analog input signals, carrying reduced granularity information from both calorimeters, are first digitized on the Pre-Processor (PPr).

In further processing steps the PPr identifies pulses and associates them to the correct LHC bunch crossing, applies a dynamic pedestal correction to mitigate pile-up effects and suppresses low energy noise. The PPr output consists of the calibrated E_T depositions in the calorimeters. These depositions are then processed by the Cluster Processor (CP) and the Jet Energy Processor (JEP).

The CP searches for candidate electrons, photons and τ, while the JEP identifies jet candidates and calculates the total, missing and jet-sum E_T. The information about the E_T, the location and the type of these trigger objects (TOBs) is transmitted to the new Common Merger Module (CMX).

The CMX calculates hit count information for the number of objects that passed configurable E_T thresholds. This information is transmitted to the CTP. In addition the TOBs are sent to the Level-1 Topological Trigger Processor (L1Topo). L1Topo is designed to identify event topologies of interest, using criteria such as the angle between TOBs or their effective mass.

Based on a trigger menu the CTP evaluates the information from L1Calo, L1Topo and L1Muon to make the final Level-1 decision. On a positive decision, a Level-1 Accept signal (L1A) is issued and the data from the subdetectors corresponding to the event is transmitted off-detector and buffered for further processing by the HLT and final data storage [32].

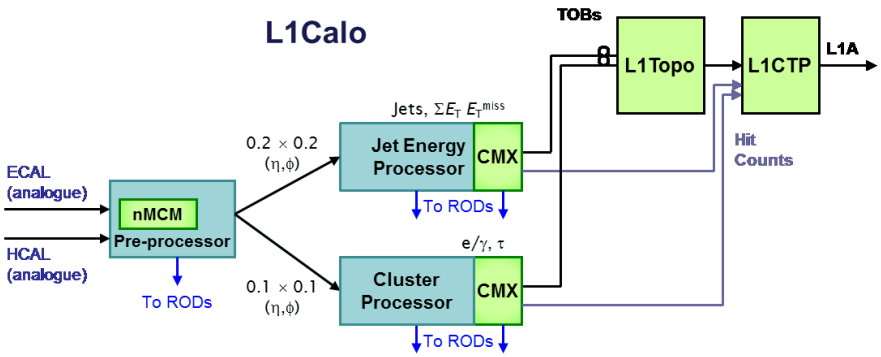

Figure 4.1: L1Calo architecture during Run 2. Components in green were installed or upgraded during LS1 and Run 2 [31].

4.1 The Analogue Input Path

L1Calo operates on analog signals from the LAr and the Tile calorimeters. The calorimeter cells are grouped to form projective trigger towers towards the nominal IP. The towers have typically a size of 0.1×0.1 in $\Delta\eta \times \Delta\phi$ and become larger for higher η. The trigger towers in the electromagnetic and the hadronic calorimeter are summed independently and have the

same size for a given $\eta \times \phi$ coordinate in most of the calorimeter, except the FCAL. An overview of the trigger tower granularity in the electromagnetic calorimeter is given in Figure 4.2.

In LAr up to 60 calorimeter cells are contained in a given trigger tower, where the number of cells depends on the calorimeter granularity and the number of layers. For Tile usually five photomultiplier signals are added together.

The signals from the about 7200 towers are routed from the ATLAS experimental cavern to the adjacent electronics cavern via cables with up to 70 m length. There they are first processed by a receiver system. The receivers convert the energy sent from the hadronic calorimeter to E_T for the calorimeter regions where this is not already done, using linear variable-gain amplifiers (VGAs). The signals from the electromagnetic calorimeter are already converted to E_T on the frontend electronics. The receivers also use the VGAs to compensate for the signal attenuation in the cables and set the E_T calibration. The resulting signals are transmitted to the PPr.

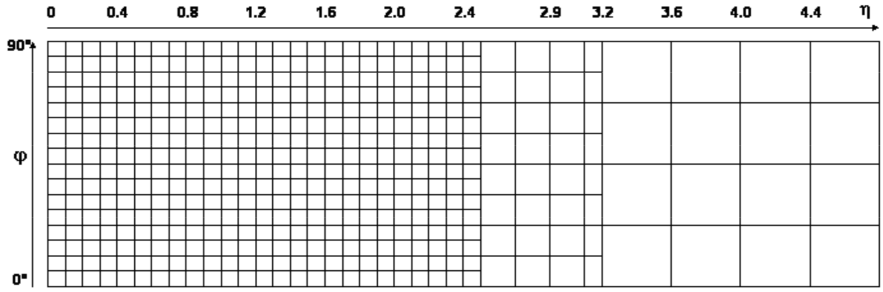

Figure 4.2: Granularity of trigger towers in the electromagnetic calorimeter for $\eta > 0$ and the first quadrant in ϕ. The layout for the other quadrants is identical and mirrored for $\eta < 0$ [32].

4.2 The PreProcessor

The PPr consists of 124 PreProcessor Modules (PPMs), each processing the signals of 64 trigger towers. First analogue input (AnIn) cards prepare the signals for digitization. The AnIn cards set an appropriate gain such that the analog signals with a maximum amplitude of up to 2.5 V fit in the 1 V dynamic range of the analog-to-digital converters (ADCs). In addition an analog voltage offset is added to ensure the digitization starts from a common ground.

The following signal processing steps on the PPM are done by the new Multi Chip Modules (nMCMs) that were installed during LS1 to replace the original Multi Chip Module (MCM) [31]. The main difference between the MCM and the nMCM is that the ASIC responsible for the signal processing was replaced by an FPGA, which offers more flexibility. Each nMCM processes four trigger tower signals, which it synchronizes and digitizes at 80 MHz to 10 bit precision. This yields one ADC sample every 12.5 ns and a sample height ranging from 0 to 1023 ADC counts. The configuration is such that the analog pedestal in absence of any signal has a digitized value of 32 ADC counts. One count in the signal peak corresponds to an E_T deposition of ≈ 0.25 GeV. The ADCs saturate at 1023 counts, which corresponds to an energy deposition

of approximately $E_T \approx 256\,\text{GeV}$ and some information on the shape of the calorimeter pulse is lost.

The digitized pulses are routed to a Field Programmable Gate Array (FPGA), which performs the bunch-crossing identification, dynamic pedestal subtraction and the final E_T calibration as well as noise suppression using a look-up table (LUT). This functionality is discussed in the following sections [31, 32].

4.2.1 Bunch Crossing Identification

The association of the signal pulses from the trigger towers to the correct LHC BC is called bunch-crossing identification (BCID). A correct BCID is very important, since the detector is read out for the identified BC, if the corresponding event passes all trigger selections. In case the BC is misidentified, the event information is at least partially lost. In addition the HLT algorithms operate on the wrong detector information, which makes it likely that the event is rejected.

Therefore a very efficient and stable mechanism is required in L1Calo to guarantee a correct BCID from the lowest to the highest energies available at the LHC. The task consists in finding the the peak in the shaped calorimeter signal. This task is complicated by several factors. Firstly, the pulses are several bunch-crossings wide and the peak sample must be accurately determined in presence of high pile-up. Secondly, the pulse shape and width vary with η and from the electromagnetic to the hadronic layer. This is due to the different technologies used in the different parts of the calorimeters, as explained in Section 3.2. Thirdly, when pulses saturate for a trigger tower the determination of the correct BC becomes more difficult, since the peak is not visible anymore.

Given these conditions, different BCID algorithms are employed for the non-saturated and the saturated regime. For non-saturated pulses a finite-impulse-response (FIR) filter is used followed by a peakfinder algorithm. This combination is often referred to as the "PeakFinder" algorithm, even if the peakfinder is only one part. This nomenclature is also kept for this thesis. For saturated pulses a threshold algorithm, called SatBCID, that operates on the leading edge of the pulse is used.

On the MCM the SatBCID operated on samples digitized with 40 MHz sampling. From the beginning of Run 2 the finer sampling of the nMCM allows for an improved threshold algorithm that operates on 80 MHz samples. To distinguish between the two thresholds algorithms they are referred to as Sat40 and Sat80.

There exists also a third algorithm, operating directly on the analog input signals on the AnIn cards. This "External BCID algorithm" uses a voltage comparator logic on the leading edge of the pulse and can be used for consistency checks. It is not used for active triggering and is also not calibrated. The Sat40, Sat80 and the PeakFinder are discussed in the following section.

The Peakfinder Algorithm The PeakFinder is designed to operate on non-saturated pulses that show a well-defined peak. In a first step a FIR filter is used to enhance the peak and improve the signal-to-noise ratio. Figure 4.3 shows a block diagram of the algorithm. Five ADC samples $a_1 \ldots a_5$ are kept in a pipeline and with each clock tick a new sample is moved into the pipeline

and the sample longest in the pipeline is moved out. The clock frequency is the LHC frequency of about 40 MHz. The FIR filter multiplies the samples in the pipeline with configurable filter coefficients $d_1 \ldots d_5$ and sums up the multiplication results. For three consecutive clock ticks n-1, n and n+1 the sums are

$$S_{n-1} = \sum_{i=1}^{5} a_{i-1} d_i, \qquad S_n = \sum_{i=1}^{5} a_i d_i, \qquad S_{n+1} = \sum_{i=1}^{5} a_{i+1} d_i. \tag{4.1}$$

In the next step a dynamic baseline correction is applied by subtracting a value ped_i. The correction depends on the position of the BC in the LHC bunch train and accounts for the varying pedestal that is caused by out-of-time pile-up. The corrected sums

$$f_i = S_i - ped_i \tag{4.2}$$

are evaluated by a peak finder that compares the current sum with the sum from the previous and the following clock tick. If for the three consecutive clock ticks the condition

$$f_{n+1} \leq f_n > f_{n-1} \tag{4.3}$$

is fulfilled then n is identified as the correct BC. It is easily seen that the PeakFinder needs to process seven ADC samples in order to make a decision.

The performance of the PF depends strongly on the FIR filter coefficients and they have to be optimized for the different calorimeter regions to account for the different pulse shapes and backgrounds. The optimal set of coefficients also depends on the pile-up situation and there are different strategies to react to low- and high pile-up. These are described in the following.

Matched Filters In a low pile-up environment a set of filter coefficients called "matched filters" is used. In this case white noise with a flat power spectrum dominates and the noise contribution to different ADC samples is not correlated. It follows that the influence of the noise will be smallest for the largest sample. Hence, to optimize the signal-to-noise ratio, the largest sample should be given the highest weight in the filtering. This leads to a set coefficients that match the pulse shape that is to say $d_i \propto A_i$, where the A_i are the samples of a normalized physics pulse [34, 35]. Hence the filter coefficients can be determined with knowledge of the pulse shape. The different pulse shapes in different calorimeter regions lead to an η dependent set of matched filter coefficients, which have been used during Run 1 and for low $\langle\mu\rangle$ runs during Run 2. A set of filters for the electromagnetic calorimeter layer is shown in Figure 4.4 [36].

Autocorrelation Filters For the high pile-up regime the assumption of white noise being dominant is no longer valid for the whole calorimeter. The overlap of calorimeter signals from several collisions and the structure of the bunch train in the LHC lead to a correlation of background in different ADC samples. This is especially the case in the forward region, where the pile-up contribution is largest. For this reason a new set of filters has been derived that take the correlations in the noise into account. These "autocorrelation filters" depend on the pile-up

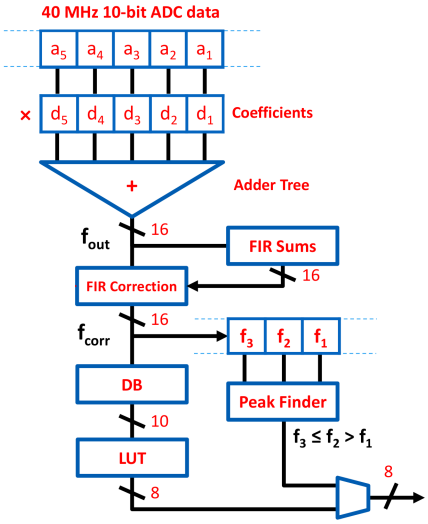

Figure 4.3: From top to bottom: FIR filter to sharpen the pulse, dynamic pedestal correction (FIR Correction), PeakFinder to identify signal peak and LUT (c.f. Section 4.2.2) to convert the reduced FIR sum into transverse energy. The reduced FIR sum is obtained by dropping bits from the FIR sum [33].

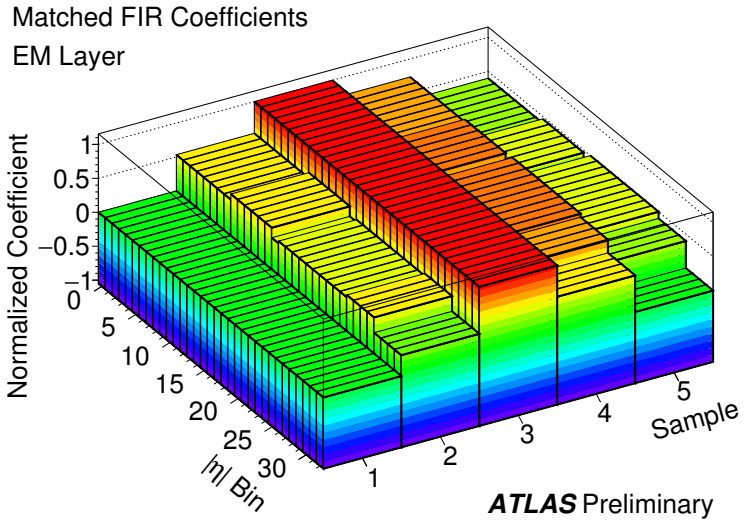

Figure 4.4: Matched Filters in bins of $|\eta|$ [37].

and need to be re-derived for changing values of $\langle\mu\rangle$. They do not follow the pulse shape like the matched filters and can have negative values for d_1, d_2, d_4, d_5. A set of coefficients for $\langle\mu\rangle = 34$ is shown in Figure 4.5 [38].

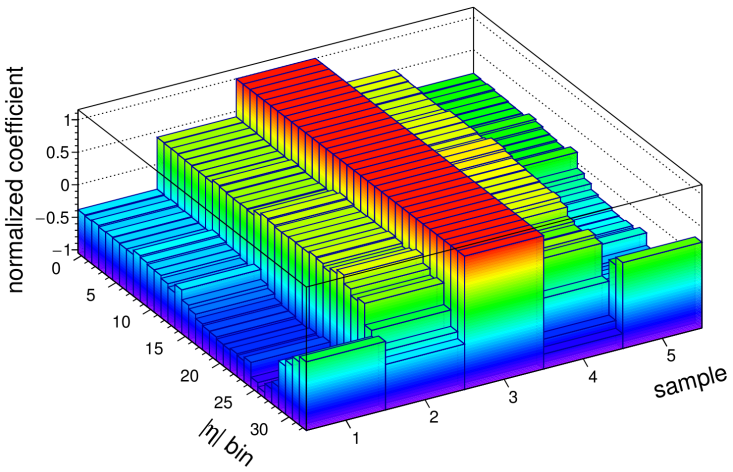

Figure 4.5: Autocorrelation Filters for $\langle\mu\rangle = 34$ in bins of $|\eta|$ [38].

The 40 MHz Saturated BCID Algorithm A physics event that leads to an energy deposition in a trigger tower causing digital saturation ($E_T \approx 256$ GeV) is considered important enough to be triggered in any case. Therefore L1Calo makes sure that an L1A is issued whenever an ADC sample saturates. However the correct BC still needs to be determined for the saturated pulse.

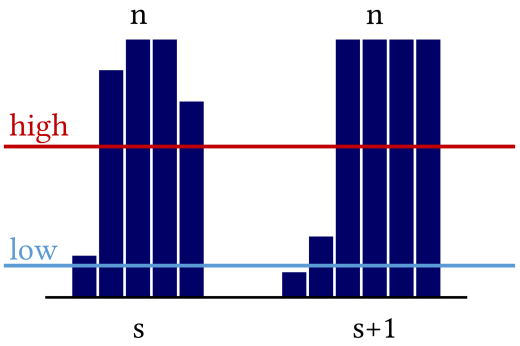

Figure 4.6: Two saturated trigger tower pulses together with the low and high thresholds of the Sat40. The pulse on the left hand side has the BC in the first saturated sample ($n = s$), the pulse on the right has the BC in the second saturated sample ($n = s+1$).

The BCID becomes difficult at higher energies, when more samples start to saturate, since the peak is no longer visible. The Sat40 threshold algorithm is foreseen to correctly identify the BC even in high saturation. The algorithm operates directly on the ADC samples and becomes active as soon as one sample saturates. Consider the two pulses shown in Figure 4.6. We call the first saturated sample s. The algorithm compares the two samples before s with a low threshold (LT) and a high threshold (HT) and decides if the BC n is in s or $s + 1$, using the

following logic

$$ADC(s-1) > HT \quad \&\& \quad ADC(s-2) > LT \qquad n = s \tag{4.4}$$
$$ADC(s-1) > HT \quad \&\& \quad ADC(s-2) < LT \qquad n = s+1 \tag{4.5}$$
$$ADC(s-1) < HT \qquad\qquad\qquad\quad n = s+1 \tag{4.6}$$

The thresholds are configurable for each trigger tower to take into account differences in the pulse shapes. During the commissioning phase of the Sat40 in Run 1 it was discovered that for certain areas no valid set of thresholds could be derived that covered the whole energy range in the saturated regime. This would have lead to an energy limit below the LHC design energy of 7 TeV for that correct BCID can still be guaranteed. An η-ϕ map of this energy limit for each trigger tower in the electromagnetic layer is shown in Figure 4.7.

To compensate for this inefficiency, a special combination of the Sat40 and the PeakFinder has been chosen during Run 1 and the beginning of Run 2. With the introduction of the nMCM and its 80 MHz sampling capability an enhanced threshold algorithm, the Sat80, has been implemented. It is designed to extend the energy range of the Sat40. Both solutions are discussed in the following.

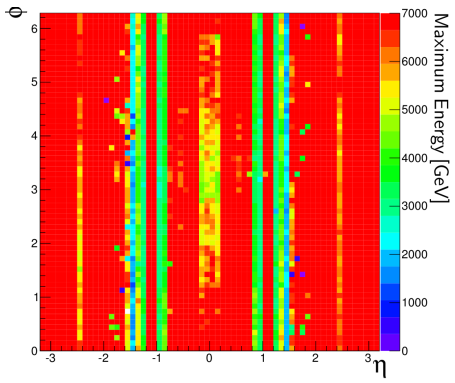

Figure 4.7: Maximum energy with full BCID efficiency for the Sat40 algorithm per trigger tower in the electromagnetic calorimeter [31].

Combination of PeakFinder and Sat40 To assure a correct BCID over the full energy range, even without the Sat40 covering the whole saturated regime, PeakFinder and Sat40 were running in a special configuration during Run 1 and the beginning of Run 2. It is based on the observation that the PeakFinder still works reliably for light saturation (up to $E_T \sim 600$ GeV) [39]. So the PeakFinder is not stopped in saturation but allowed to take a decision in parallel to the Sat40. The system is designed such that the earliest identified BC is taken as the BCID result. For this to work, the Sat40 thresholds were set to the following values for all trigger towers: $LT = 5, HT = 1023$ ADC counts. Considering the Sat40 logic shown in Equation 4.6 this effectively forces the Sat40 to always identify the second saturated sample $s + 1$. The behaviour of this combination for pulses with increasing saturation is shown in Figure 4.8.

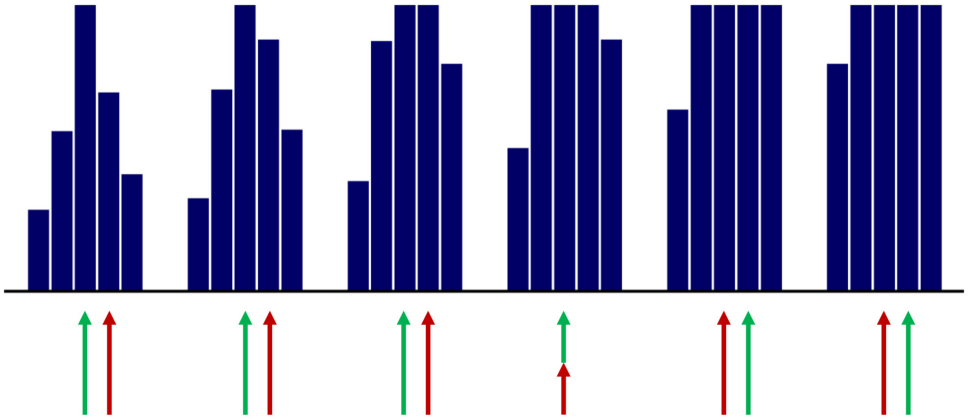

Figure 4.8: Combination of PeakFinder (green) and Sat40 (red) during Run 1 and in the beginning of Run 2.

At low energies the PeakFinder decides correctly, while the Sat40, pointing at $s+1$, is too late. This is not a problem since the earlier BC is taken. In the medium energy range, when more samples start to saturate there is an overlap where both algorithms identify the correct BC. In the regime of high saturation, the PF fails and starts to identify the BC one sample too late. There however the Sat40 identifies the BC correctly and the final decision is correct.

The 80 MHz Saturated BCID Algorithm The Sat80 is a threshold algorithm similar to the Sat40. However, using the improved sampling capabilities of the nMCM, it operates on 80 MHz samples, denoted here by half-integer values. This increases the amount of information available from the leading edge of the pulse allowing for a logic with higher precision and triggering even in cases of extreme saturation, when the two samples before the peak are both saturated. This $n = s + 2$ case can not be triggered with the Sat40 and constitutes its upper limit. The Sat80 operates similar to the Sat40 and also compares the samples before the first saturated sample s with a low threshold (LT) and a high threshold (HT) to decide the BC n. However it uses a different logic, with s the first saturated 40 MHz sample:

$$ADC(s-1) > HT \quad ADC(s-1.5) > LT \qquad n = s \tag{4.7}$$
$$ADC(s-1) > HT \quad ADC(s-1.5) < LT \qquad n = s+1 \tag{4.8}$$
$$ADC(s-1) < HT \quad ADC(s-0.5) > HT \qquad n = s+1 \tag{4.9}$$
$$ADC(s-1) < HT \quad ADC(s-0.5) < HT \qquad n = s+2 \tag{4.10}$$

As for the Sat40 the thresholds are configurable for each trigger tower. The determination procedure is described in Section 8.1. After careful commissioning the Sat80 was activated for physics triggering at the end of the 2016 data taking and did not cause any mistriggered events. The attempt to validate it using the calibration system explained in Section 3.2.4 is part of this thesis and described in Section 8.

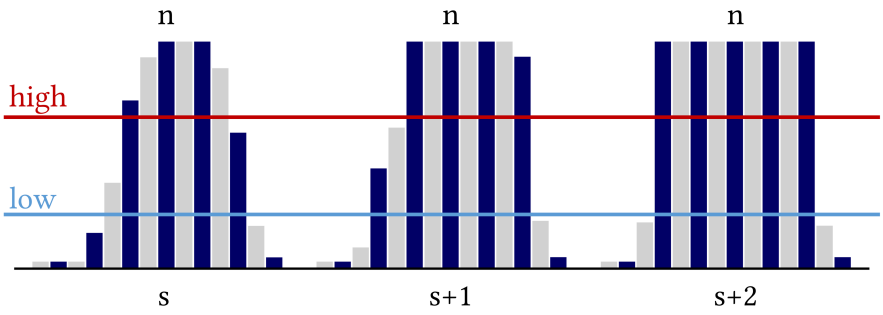

Figure 4.9: Visualization of the logic of the Sat80 algorithm.

4.2.2 E_T determination

The final E_T that is transmitted to the downstream L1 systems is determined in the nMCM. There are two possible cases. Saturation will always cause an L1A and the E_T that is transmitted on the correct BC is set to the maximum value of 8 bit.

For non saturated-pulses the pedestal corrected output sum of the FIR filter is first converted from a 16 bit number to a 10 bit number, by dropping bits (DB). This 10 bit number is input to two independent look-up tables (LUTs), one for the CP and one for the JEP, to convert it to E_T. So far a linear function has been used for the conversion, though non-linear look-up tables are under study.

4.2.3 Readout to Data Acquisition

The LUT output values are transmitted to Cluster Processor and Jet-/Energy Processor on the realtime path. In addition, information is read out to the ATLAS Data Acquisition System (DAQ) in case of an L1A. The readout contains a fixed number A of ADC samples centered around the triggered BC. These can be 40 MHz or 80 MHz samples. Furthermore for L BCs around the triggered BC the output of both the CP-LUT and JEP-LUT are read out, as well as two 3 bit words. In the original design these are the "PSE"-bits and the "RHL"-bits. The first word contains the decision of the PeakFinder (P), the Sat40 (S) and the External BCID (E) algorithm. The second word contains the Sat80 result bit (R) and information whether the high threshold (H) and the low threshold (L) were passed. In addition the value of the pedestal correction is transmitted for the same L BCs. The exact readout choice is referred to as $A + L$ readout mode. For physics data taking it is usually $5 + 1$ with 40 MHz ADC samples, since the readout of more information limits the maximum read-out rate, thus limiting the maximum trigger rate. However there are special scenarios where more information is read out, for example $7 + 1$ mode or $15 + 1$ mode with 80 MHz ADC samples.

4.3 The Cluster Processor - Electron / Photon Identification at L1

The Cluster Processor (CP) identifies electron, photon and tau/hadron candidates at Level-1 using sliding window algorithms. It operates on the trigger tower E_T sent by the PPr at every

BC for $|\eta| < 2.5$. This matches the high-precision tracking and calorimetry (c.f. Section 3.1 and Section 3.2) region.

Electron and photon candidates are treated as identical on Level-1, since no track information is available and the granularity of the trigger towers is much too coarse to resolve the differences in the shower development. The e/γ algorithm hence searches for narrow, high-E_T clusters that do not penetrate into the hadronic calorimeter and have some transverse isolation. These requirements help to reduce hadronic jet background. In contrast the τ/hadron algorithm allows energy deposition in the hadronic calorimeter.

The basic elements of the two algorithms are shown in Figure 4.10. Both calculate energy sums of towers. A 4×4 trigger tower window is considered and the possible 2×1 and 1×2 sums in the central four trigger towers are calculated. For the e/γ algorithm one of these sums has to pass a minimum threshold, while for the τ/hadron algorithm each single sum is added to the four central hadronic towers and one of these sums is required to pass the threshold. The summing of always two towers in done to account for a possible "splitting" of the electromagnetic shower over two trigger towers, when an electron impacts on the border. This behavior is studied in more detail in Section 6.3.4. The 12 surrounding towers in the electromagnetic layer are summed and checked against an energy dependent EM isolation threshold. The same comparison is also done with the towers in the hadronic layer against an independent hadronic threshold. The penetration in the hadronic layer is controlled by comparing the four central hadronic towers with a hadronic veto threshold. To create different trigger items, several combinations of these thresholds can be predefined in the trigger menu.

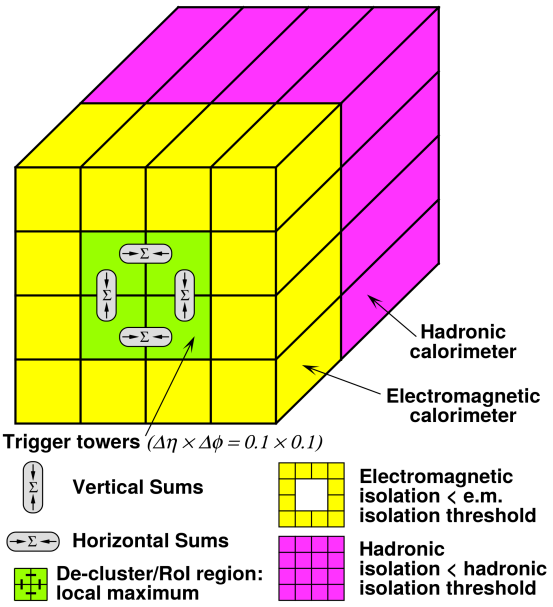

Figure 4.10: Basic Elements of the CP algorithms [32].

4.4 The Jet/Energy-sum Processor

The Jet/Energy-sum Processor (JEP) searches the electromagnetic and hadronic calorimeters for jets in the region $|\eta| < 4.9$ and calculates total-E_T and missing E_T for $|\eta| < 4.9$. The JEP operates on jet elements, which are the sums of 2×2 trigger towers in the electromagnetic layer summed with the same 2×2 windows in the hadronic layer. The coarser granularity of $\Delta\eta \times \Delta\phi = 0.2\times0.2$ is sufficient for triggering jets, since they typically produce wider showers than electromagnetic objects. The jet algorithm also relies on sliding windows. Different windows sizes can be used depending on the desired jet multiplicity as shown in Figure 4.11. The jet algorithm requires the energy deposited inside the window to exceed a minimum threshold. The shaded area is called Region-of-Interest (RoI) and the energy in it is required to be a local maximum, to resolve possible ambiguities when the threshold is exceeded in several windows. It is further used to define the $\eta \times \phi$ position of the jet candidate.

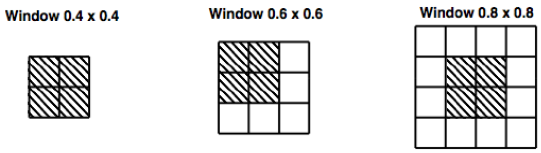

Figure 4.11: Jet algorithm windows. The shaded region is an RoI and each square corresponds to 0.2×0.2 jet element [32].

5 Electron and Photon Identification

The studies described in this thesis are largely based on electrons and photons. Therefore a thorough understanding of these objects is required. This chapter describes the interaction of electromagnetic particles with the ATLAS detector and the reconstruction and identification of electrons and photons.

5.1 Interaction of Electromagnetic Particles with Matter

Electrons and photons interact with matter through different processes depending on their energy. The most important processes are shortly described in the following. For electrons these are ionization and Bremsstrahlung. Ionization occurs when a charged particle passes through a medium. The particle interacts electromagnetically with the atomic electrons and transfers a part of its energy to them. Consequently the atoms are ionized. The energy loss by ionization depends on the particle velocity $v = \beta c$ and the material the particle passes through which is characterized by its atomic number Z and number density n. The mean energy loss per unit length is given by the Bethe-Bloch equation,

$$\frac{dE}{dx} = -4\pi\hbar^2 c^2 \alpha^2 \frac{nZ}{m_e v^2} \left(ln \left[\frac{2\beta^2\gamma^2 c^2 m_e}{I_e} \right] - \beta^2 \right), \tag{5.1}$$

where $I_e \approx 10Z$eV is the averaged ionization potential of the material. The mean energy loss curve that follows from the Bethe-Bloch equation is shown in Figure 5.1. For small energies the energy loss is largest and decreases up to a minimum around $\beta\gamma \approx 3-4$. Particles with this velocity are called “mimimum ionizing”. For higher energies the energy loss increases again, but only logarithmically.

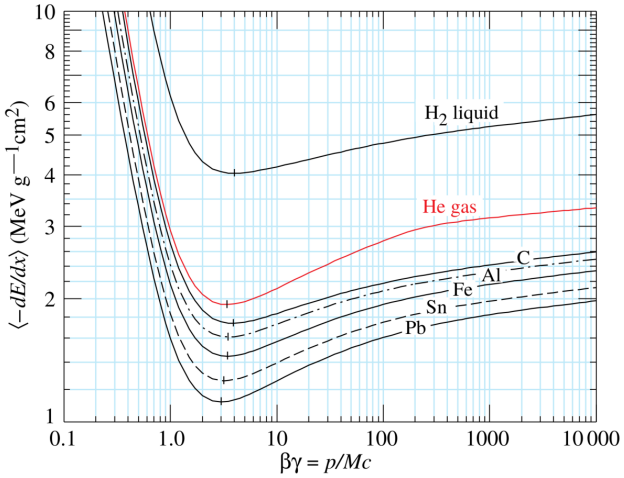

Figure 5.1: Mean ionisation energy loss for a charged particle traversing different media. Shown are liquid hydrogen (H_2), helium (He) gas, carbon (C), Aluminum (Al), Iron (Fe), Tin (Sn) and lead (Pb) [40].

When an electron is deflected or decelerated it emits a photon. The issuing radiation is called "Bremsstrahlung" and it can be produced in the electrostatic field of a nucleus or another electron. The energy loss per unit length due to Bremsstrahlung for a particle with energy E is typically parametrized as

$$\frac{dE}{dx} = -\frac{E}{X_0}, \tag{5.2}$$

where X_0 is called the radiation length and is a material dependent constant. While Bremsstrahlung also occurs for other charged particles, it is suppressed by $\frac{1}{m^2}$. Therefore it is usually negligible for particles heavier than the electron.

Figure 5.2 shows the contribution of Ionization and Bremsstrahlung to the total energy loss of an electron in copper. Since the energy loss via ionization rises much slower than the energy loss via Bremsstrahlung (logarithmic versus linear), there is an energy where both are equal. It is called the critical energy E_C. Beyond it the electron looses energy mainly via Bremsstrahlung. This is usually the case for particles produced at the LHC, which have energies in the order of GeV. With $Z = 18$ the liquid argon used in the ATLAS electromagnetic calorimeter has only a critical energy of $E_C \approx 32\,\text{MeV}$.

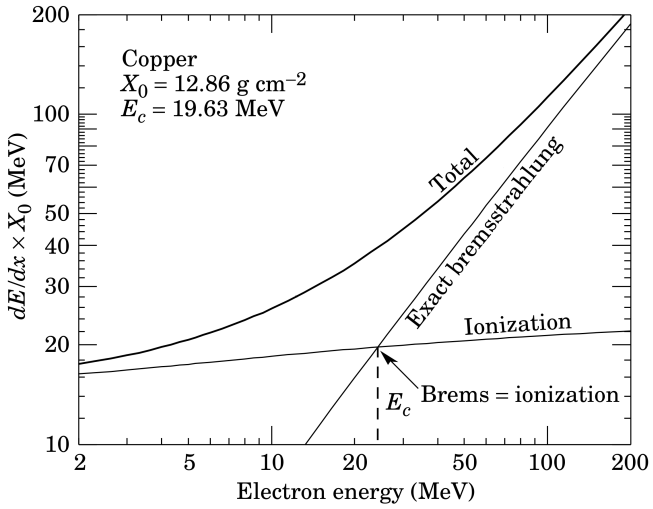

Figure 5.2: Energy loss of electrons per radiaton length X_0 as a function of the electron energy. Beyond the critical energy E_C the energy loss is dominated by Bremsstrahlung [40].

The main processes for the energy loss of photons in matter are the photoelectric effect, Compton and Rayleigh scattering and pair production. The photoelectric or photo effect (p.e.) is the absorption of a photon by an electron bound in an atom, where the electron gains enough energy to be freed. Compton and Rayleigh scattering both describe the scattering of a photon off an electron where a part of the photon energy is transferred to the electron. While Compton scattering happens with a lightly bound or free electron, in Rayleigh scattering a tightly bound inner electron is involved and the recoil momentum is absorbed by the whole atom. Therefore the energy loss is much smaller in Rayleigh scattering. At the high energies present at the LHC

electron-positron pair production dominates. The conversion of the photon into the electron-positron pair can either happen in the field of an electron or of the nucleus. The probability to produce an electron-photon pair depends on the radiation length X_0 and is given by

$$\frac{dw}{dx} = \frac{9}{7} X_0 e^{-\frac{7}{9}\frac{x}{X_0}}. \tag{5.3}$$

The cross sections for the main energy loss processes for photons are shown in Figure 5.3.

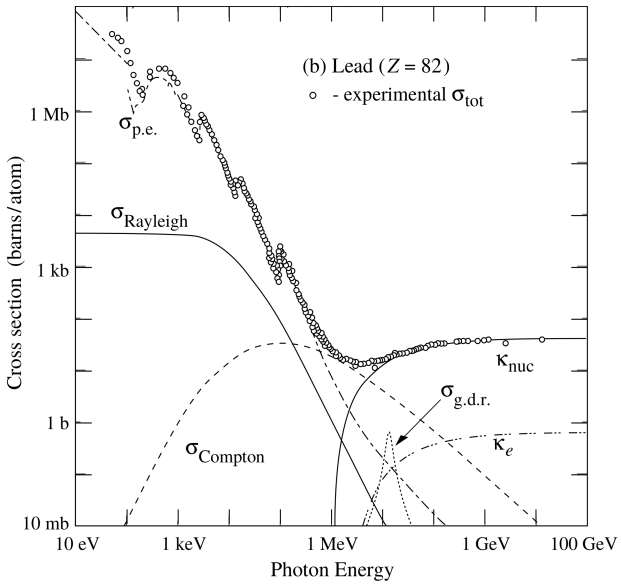

Figure 5.3: Total photon interaction cross-section as a function of energy. The contribution of different physics processes is shown. The photoelectric effect (p.e.), Rayleigh and Compton scattering are most important at lower energies, while at higher energies pair production in the nuclear (κ_{nuc}) and the electron (κ_e) field dominates [40].

5.2 Interaction of Electromagnetic Particles with the Detector

The interactions explained in the previous section govern the behavior and energy depositions of electrons and photons in the different parts of the ATLAS detector. First the particles pass through the ID, where electrons deposit some energy in the different layers due to ionization. The high granularity and good space-point resolution allows for these energy deposits to be located precisely and to be used in the reconstruction of the electron track. In addition electrons can also emit Bremsstrahlung, which causes a larger energy loss than ionization. Photons pass without leaving a track, as they are not charged and do not deposit energy via ionization. However in the material of the ID pair production can happen, where the photon is converted into an electron-positron pair. Both Bremsstrahlung and photon conversion are taken into account during the reconstruction, described in the next section.

Electrons and Photons usually deposit the largest part of their energy in the electromagnetic calorimeter. An interplay of Bremsstrahlung and pair production leads to the development of

an electromagnetic particle cascade, called a shower. As discussed in the next chapter the shape of this shower is detected using the fine calorimeter granularity and used to identify electromagnetic objects. To understand the shower development and shape an analytic model is presented in the following.

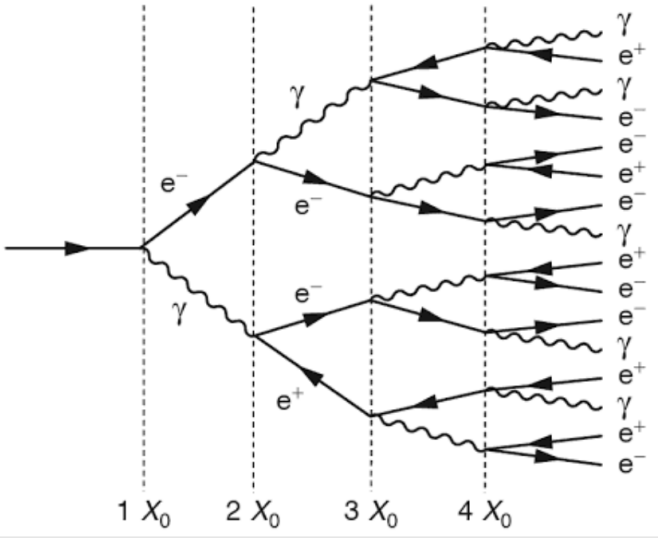

Figure 5.4: Simple model of electromagnetic shower development. After a length of X_0 electrons emit a Bremstrahlung photon and photons undergo pair production. The energy is split equally between the daughter particles [17].

A simplified electromagnetic shower is shown in Figure 5.4. Since both Bremsstrahlung (c.f. Equation 5.2) and pair production (c.f. Equation 5.3) are governed by the radiation length X_0, the incoming electromagnetic particles interact with the material each time after passing a distance of approximately X_0. Photons undergo pair production, electrons emit Bremsstrahlung and the energy is divided equally among the daughter particles. In this way a shower develops and the number of particles doubles in each step, while the energy per particle decreases by a factor of two. This process continues until the energy per particle drops below the critical energy E_C. Then ionization and Compton scattering start to dominate and the cascade comes to an end. This point marks the position of the shower maximum in units of X_0, given by

$$t_{max} \propto ln\left(\frac{E_0}{E_C}\right) + C, \tag{5.4}$$

where $C = 0.5$ for a shower caused by a photon and $C = -0.5$ for an electron-induced shower and E_0 is the initial particle energy. The electrons and positrons are stopped quite rapidly after the maximum within one radiation length X_0. The low energy photons however are not absorbed so fast and extend the length of the shower for further 7 to 9 X_0. The ATLAS electromagnetic calorimeter has for example an depth of 25 to 30 X_0 in the EMB to ensure shower containment.

The width of the shower is also determined by low energetic particles since the photons

and electron-positrons pairs produced in the showering process are emitted in a very forward direction, making up the narrow core of the shower. The low energy electrons at the shower edge however undergo multiple scattering before they are absorbed. This defines the transverse shower size. As discussed in [41, 42] multiple scattering is described by the Molière theory and the shower width is given by the Molière Radius

$$R_M = \frac{21\,\text{MeV}}{E_C} X_0, \tag{5.5}$$

which again depends on the radiation length X_0, but not on the initial particle energy E_0.

An example for a real electromagnetic shower is shown in Figure 5.5, together with a hadronic shower that is discussed in detail in [43]. It illustrates the shape differences of these two shower types, where the proton-induced hadronic shower is typically wider and longer. These differences are used for particle identification, which is discussed in the next section [41, 42, 44, 45].

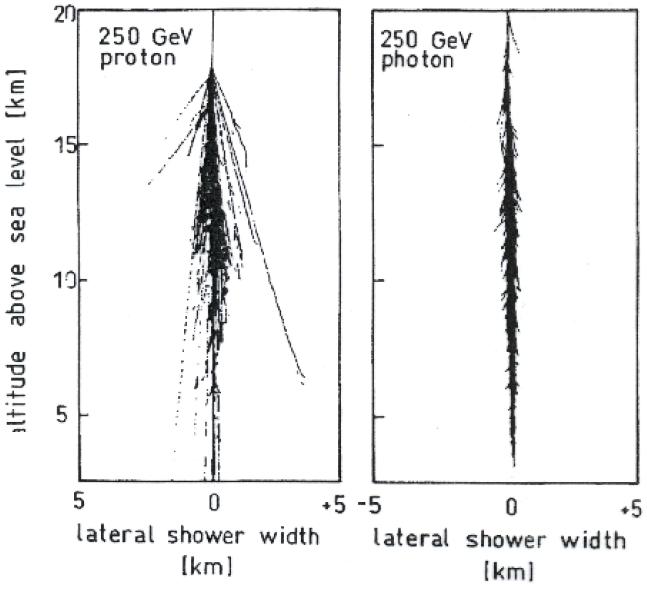

Figure 5.5: Shower shape of hadronic (left) and electromagnetic (right) particle in air. Hadronic showers are considerably wider and longer [44].

5.3 Electron and Photon Reconstruction

Electrons and Photon produce very similar showers in the calorimeter. For this reason their reconstruction proceeds in parallel. The important steps in the reconstruction process are clustering, track reconstruction and association and the separation of electrons from converted and unconverted photons. Here only objects with $|\eta| < 2.5$ are considered, which corresponds to the high precision tracking and calorimetry region (c.f. Section 3.1 and Section 3.2).

The first step is to reconstruct "seeds" in the electromagnetic calorimeter using a sliding window algorithm with a window size of 0.075×0.125 in $\eta \times \phi$. This size corresponds to 3×5 calorimeter cells in the middle calorimeter layer. If a deposition with $E_T > 2.5\,\text{GeV}$ is found, a seed is formed. A clustering algorithm finds the electromagnetic clusters around the seeds and removes duplicates [46].

For track reconstruction a pattern recognition algorithm determines track candidates from the hits in the ID. It takes energy losses in the material as well as Bremsstrahlung into account. The track candidates are fitted using different track fitters that decide on the final track selection and reject fake tracks caused e.g. by noise or combinatorial effects.

The next step is track association. The tracks are extrapolated into the middle layer of the calorimeter and matched to the electromagnetic clusters using the distance between the tracks and the cluster barycenter. Furthermore tracks are required to be compatible with the primary vertex.

Electromagnetic candidates that have hits in the innermost layer of the pixel detector and which are compatible with the primary vertex are reconstructed as prompt electrons. Candidates that have no associated hits in the precision layers of the ID are considered to be unconverted photons. In addition unconverted photons that have been misidentified as electrons, due to the misassociation of a track, are recovered by placing cuts on low p_T tracks.

Photons that have undergone pair production before reaching the calorimeter are called "converted photons". A dedicated algorithm searches for these photons by identifying conversion vertices. These are typically associated to tracks of oppositely charged particles with a high probability to belong to electrons. The tracks associated to a conversion vertex are also required to be parallel in the vicinity of the vertex. Furthermore the algorithm can also identify "single track conversion", a case that happens when the tracks are either very close or one of the produced electrons is too soft to be reconstructed.

5.4 Electron Identification

Dedicated algorithms for electron identification are used to refine the selection made during reconstruction and reject background caused by hadronic jets and converted photons. Amongst others, these algorithms use shower shape information from the electromagnetic calorimeter, track information and information on transition radiation from the TRT (c.f. Section 3.1). This is illustrated in Figure 5.6. A full list of discriminating variables can be found in [47]. The algorithms are optimized using Monte Carlo (MC) samples and distributions corrected with information derived from recorded data.

A likelihood-based approach is used for electron identification. The likelihood-based method uses a discriminant d_L, which is constructed from the probabilities for the electron to be signal (L_S) or background (L_B)

$$d_L = \frac{L_S}{L_S + L_B}. \tag{5.6}$$

The probabilities L_S and L_B are in turn constructed from the corresponding probability density functions (PDFs) $P_{s(b),i}$ of the n discriminating variables x_i

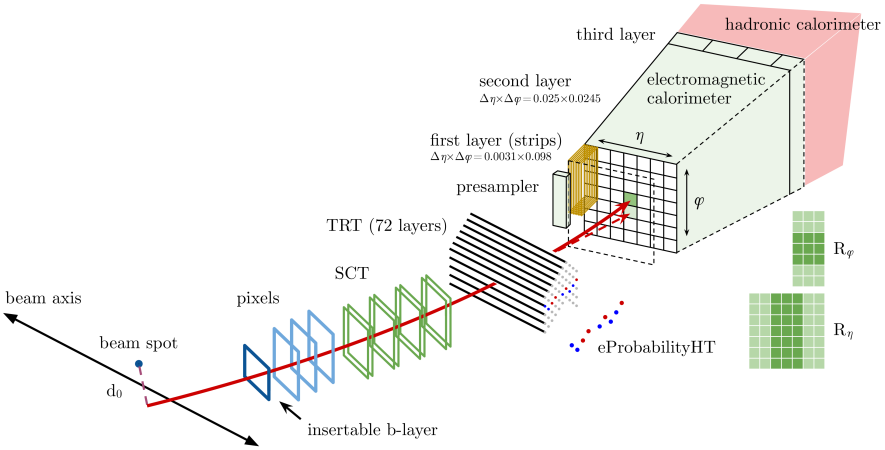

Figure 5.6: Reconstruction and identification of electromagnetic objects in the ATLAS detector. Precision hits in IBL, pixels, SCT and TRT are used to reconstruct the electron track / photon conversion vertices and determine the location of the interaction vertex with respect to the beam spot (d_0). Transition radiation in the TRT helps to distinguish electrons from heavier particles like pions. The shower shape in the electromagnetic calorimeter can be recorded due to the high granularity and provides additional distinguishing power [47].

$$L_{S(B)} = \prod_{i=1}^{n} P_{s(b),i}\left(x_i\right). \tag{5.7}$$

The electron identification algorithm has three working points of increasing background rejection, called *Loose*, *Medium* and *Tight*. These are inclusive, which means that all electrons selected by *Tight* will also be selected by *Medium* and all electrons selected by *Medium* will also be selected by *Loose*.

The working points are optimized in bins of η and E_T as the shape of the electromagnetic showers depends on the amount of material in front of the calorimeter that varies with η. The optimization in bins of E_T accounts for the energy dependence of the shower shape as well as the track properties.

The identification efficiency for electrons from Z->ee decays as determined from simulation is shown in Figure 5.7. It is higher for weaker selection criteria, at the price of a lower background rejection. The efficiency improves with energy, especially for the stricter working points [19, 47, 48].

5.5 Photon Identification

Photon identification in ATLAS relies on the shape of the electromagnetic shower in the calorimeter. It is usually narrower than hadronic showers and deposits much less energy in the hadronic calorimeter. Photons from hadron decays are usually produced in pairs and very close together. They can be detected and seperated using the fine granularity of the first calorimeter layer.

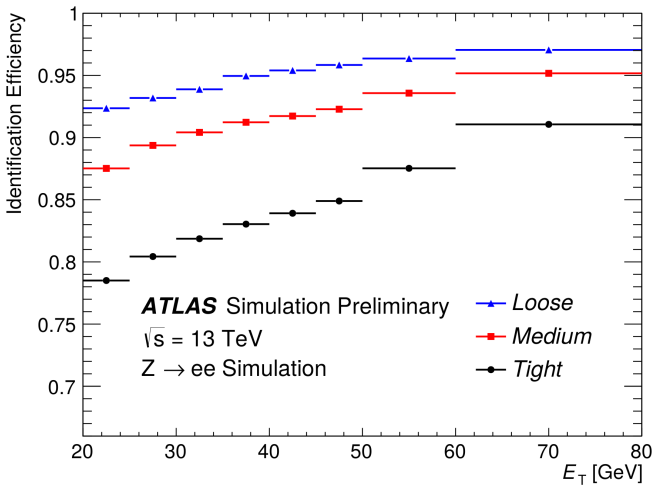

Figure 5.7: Identification efficiency of electrons from Z→ee decays. The efficiency increases for looser selection criteria, which however also include more background. For higher energies the identification efficiencies become larger [47].

The algorithms used to identify photons rely on different variables containing information about the shower shape and the energy deposition in the hadronic calorimeter. These are listed in [49]. The algorithm has two working points, *Loose* and *Tight*. The *Loose* identification uses only information from the hadronic calorimeter and the second layer of the electromagnetic calorimeter, while *Tight* uses the finely segmented first layer in addtion and imposes stricter requirements than *Loose* on the other variables.

Photons leave no track in the detector unless photon conversion takes place and the use of the tracker in identifying photons is limited. Therefore isolation requirements are especially important for photon identification. The isolation is defined using the transverse energy and momentum in a cone around the photon candidate.

The transverse energy isolation is calculated by summing the calorimeter E_T in the cone after subtracting the photon candidate and the pile-up contribution. The isolation p_T is defined by summing the p_T of all tracks with transverse momentum larger than 1 GeV in the cone, while not considering tracks from conversion vertices. Cuts on these variable help to reduce background photons, which are usually surrounded by hadronic activity.

The photon identification relies heavily on the shower shape and therefore is only efficiently possible where the depth of the electromagnetic calorimeter is large enough to contain the shower and where the segmentation of the first calorimeter layer is fine enough to reject photons from hadron decays. This is not the case in the overlap region ($1.37 < |\eta| < 1.52$), which is therefore usually excluded from photon analyses [49, 50].

6 Analysis of the PeakFinder Mistiming in Physics Data

The introduction of autocorrelation filters for the PeakFinder in Run 2 together with the special configuration chosen for the BCID algorithms at that time (see Section 4.2.1) lead to a wrong BCID decision for highly saturated events. As part of the work for this thesis, the effect on physics events, specifically electromagnetic objects, has been studied. These studies are described in this chapter.

6.1 Discovery of the PeakFinder Mistiming

After the first months of proton-proton running in Run 2 approximately 120 events were discovered for which the BC was misidentified by the BCID algorithms. In all cases the events were triggered one BC too early. An overview of some of the first of these events containing electromagnetic objects is given in Table .1.

Run	Event number	EM object p_T [GeV]	η
279 685	1 150 956 342	1088	−1.11
280 319	1 710 774 724	1515	−1.15
280 423	1 151 249 857	1333	1.25
281 143	1 710 563 265	941	−0.75
283 074	263 868 207	1333	1.25
283 074	639 876 830	1088	−1.25

Table 6.1: Selection of events affected by the PeakFinder mistiming, which involve a high-p_T electromagnetic object.

The events are characterized by a high-p_T object that caused the early trigger. This is known because the CP input is not only read out for the triggered BC (n), but also for the previous $(n-1)$ and the subsequent $(n+1)$ BCs. Here and in the following, the correct BC is always called n and the other samples are referenced relative to it.

Figure 6.1 shows an $\eta-\phi$ map with the energy depositions in the electromagnetic calorimeter as seen by the CP for event 263 868 207 from Table .1. The triggered BC $(n-1)$ is shown in the top panel and the following BC (n) in the bottom panel. For $n-1$ there is one saturated tower at $\eta = 1.25, \phi = -0.25\,(346°)$, while for n the rest of the event is recorded, with the saturated tower missing.

The calorimeters allow to recover some energy information about the mistimed event from the pulse that is read out. The information from other detector systems however is lost. This is the case for ID that is only read out for the triggered BC n, due to the large amount of data contained in the tracks. Therefore it is also not possible to know if the electromagnetic object was an electron or photon, since no track information is available.

The readout of the subdetectors at the wrong time is likely to prevent the event from passing the HLT selection. The HLT operates on the full detector readout at $n-1$ that does not contain the event information. Therefore the event is likely to be rejected.

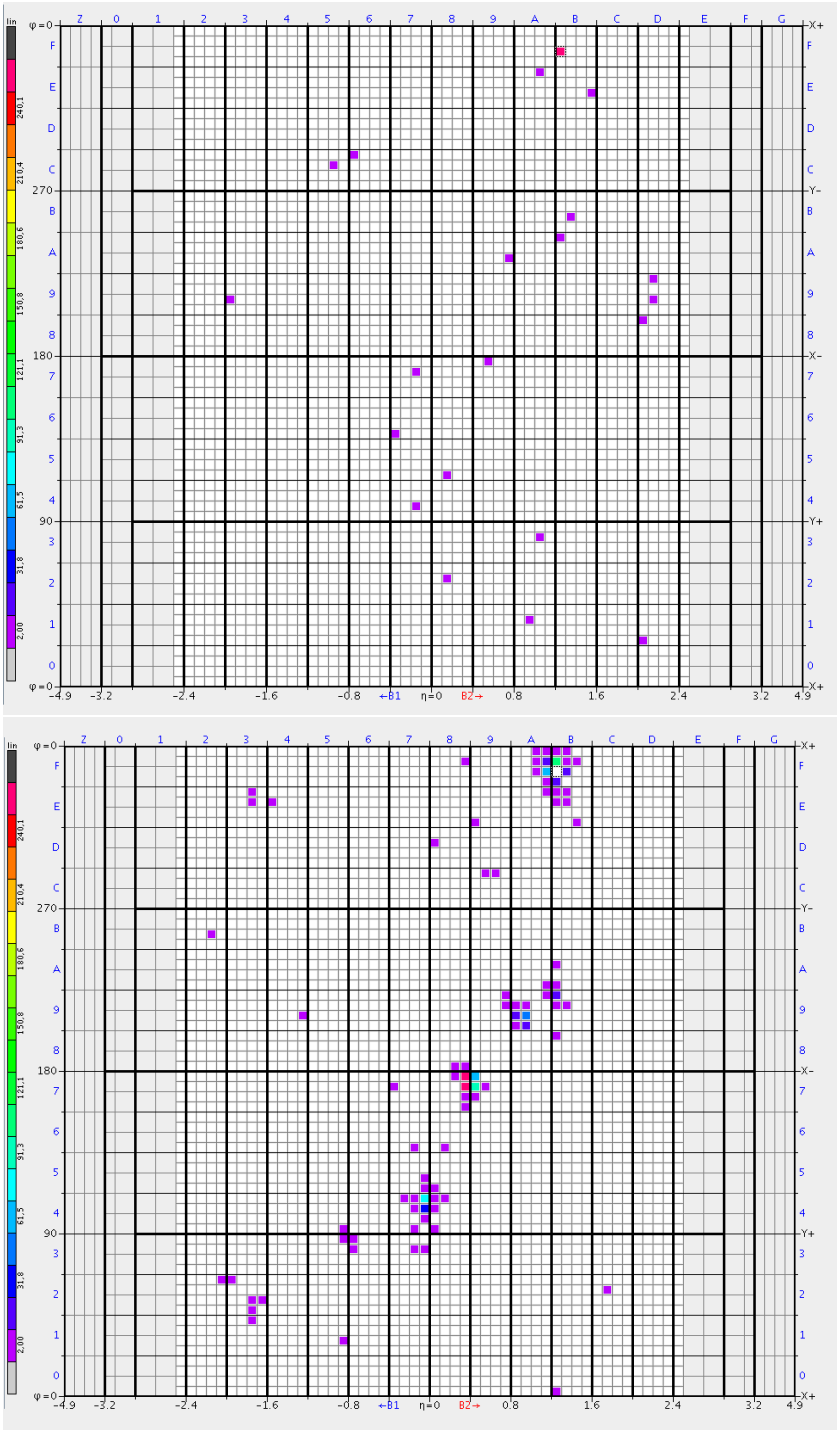

Figure 6.1: η-ϕ map of the energy deposition in the electromagnetic calorimeter for the mistimed event 263 868 207 from run 283 074. The top panel shows the readout for the triggered BC $n-1$, the bottom panel shows the readout one BC later (n).

6.2 Cause of the PeakFinder Mistiming

The pulse of the mistimed trigger tower from the event in Figure 6.1 is shown in the top panel of Figure 6.2. The correct BC (n) is indicated by a green arrow, the actual triggered BC ($n-1$) by a red one. Since the Sat40 is configured to always fire on the second saturated sample, which is in this case n (compare Section 4.2.1), it must have been the PeakFinder that fired early.

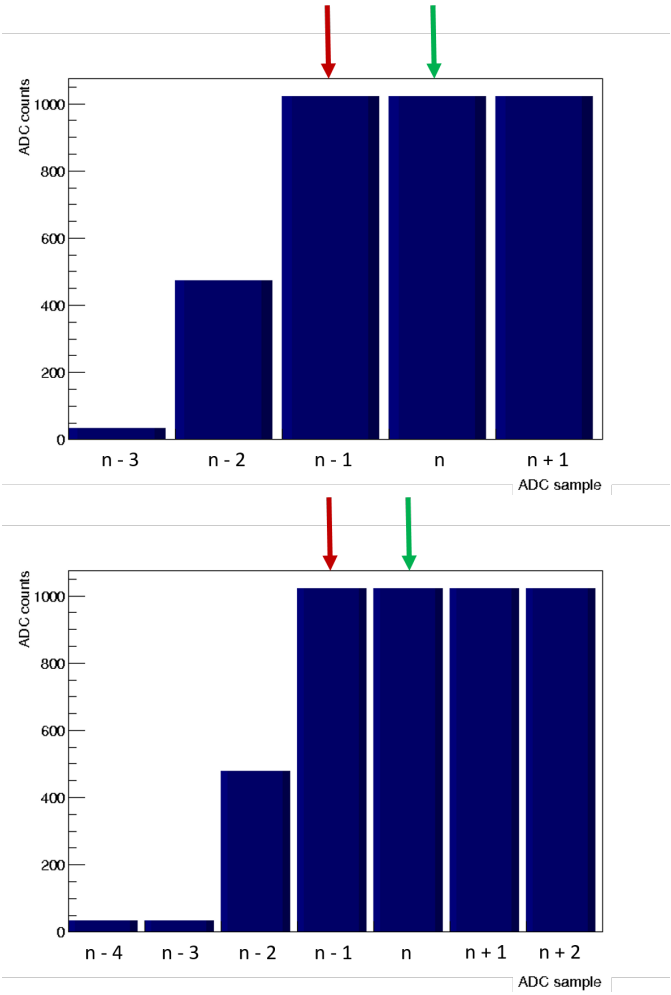

Figure 6.2: Top panel: Pulse from the mistriggered tower ($\eta = 1.25$,$\phi = -0.25$) shown in Figure 6.1. The arrows indicate the BC wrongly identified by the PeakFinder (red) and the correct BC (green). Bottom panel: Same pulse, with the assumed $n-4$ and the $n+2$ sample added.

It is in principle possible to recalculate the PeakFinder decision with knowledge of the ADC samples. However this is not the case for the standard $5+1$ readout mode, since at least seven ADC samples are necessary.

However, the missing samples ADC_{n+2} and ADC_{n-4} can be guessed by making some

reasonable assumptions. From the high offline p_T, reconstructed by the calorimeters for the misidentified objects, a good assumption is that ADC_{n+2} is saturated. Another safe assumption is that the value of ADC_{n-4} sample equals the pedestal, since this is already the case for the ADC_{n-3} sample. The bottom panel of Figure 6.2 shows the pulse from the readout with $ADC_{n-4} = 32$ and $ADC_{n+2} = 1023$ samples added.

Using this information and the autocorrelation filters, the PeakFinder decision can be calculated. This is done in Table 6.2 according to the prescription given in Section 4.2.1.

ADC samples	Filter Coefficients	FIR Sum
$a_{n-4} = 32$		
$a_{n-3} = 34$	$d_{-2} = -6$	
$a_{n-2} = 476$	$d_{-1} = 4$	$S_{n-2} = 9819$
$a_{n-1} = 1023$	$d_0 = 10$	$S_{n-1} = 17045$
$a_n = 1023$	$d_1 = 4$	$S_n = 16581$
$a_{n+1} = 1023$	$d_2 = 1$	
$a_{n+2} = 1023$		

Table 6.2: Calculation of the FIR sums for an early triggered event.

The FIR sums fulfill the relation $S_{n-2} < S_{n-1} > S_n$, causing the PeakFinder to identify $n-1$ as the correct BC for the tower. Since the BCID algorithms are configured such that the earliest BC decision is taken and the Sat40 identifies n as the BC in this case, the early trigger is caused.

The reason for the misidentification of the BC by the PeakFinder is the negative value of the d_{-2} autocorrelation filter coefficient. It decreases the sum S_n of the correct BC with respect to the sum of the earlier BC S_{n-1}, where d_{-2} is only multiplied with an ADC value close to the pedestal and therefore has a much lower weight. It is possible to derive a critical value ADC_{crit} for ADC_{n-2}. As soon as the energy is high enough for ADC_{n-2} to be larger than this critical value, the PeakFinder mistiming starts to occur.

Consider the PeakFinder sums for S_{n-1} and S_n. Mistiming will happen, once the following condition is fulfilled

$$S_{n-1} > S_n. \tag{6.1}$$

This equals

$$\sum_{i=-2}^{2} d_i a_{n-1+i} > \sum_{i=-2}^{2} d_i a_{n+i}. \tag{6.2}$$

Here the d_i are the autocorrelation filter coefficients and a_{n-x} is the value of the ADC_{n-x} sample. To simplify Equation 6.2 we assume saturation in samples ADC_{n-1}, ADC_n, ADC_{n+1} and ADC_{n+2}. This assumption is motivated by the behavior of the pulse shape. For the PeakFinder mistiming to occur, the ADC_{n-2} sample has to reach a sufficient height. This is only the case in high saturation.

The simplification leads to

$$d_{-2}a_{n-3} + d_{-1}a_{n-2} > d_{-2}a_{n-2} + d_{-1}a_{n-1}. \tag{6.3}$$

The sample ADC_{n-3} is assumed to have the pedestal value, $a_{n-3} = 32$. This gives

$$32 \cdot d_{-2} + d_{-1}a_{n-2} > d_{-2}a_{n-2} + 1024 \cdot d_{-1}, \tag{6.4}$$

which can be used to determine a condition on the height a_{n-2} sample

$$a_{n-2} > \frac{1023 \cdot d_{-1} - 32 \cdot d_{-2}}{d_{-1} - d_{-2}} =: ADC_{crit}. \tag{6.5}$$

The critical ADC value of the ADC_{n-2} sample depends on the filter coefficients, which results in a dependency on η. ADC_{crit} is shown in Figure 6.3 as a function of η for the autocorrelation filter coefficients used at the beginning of Run 2.

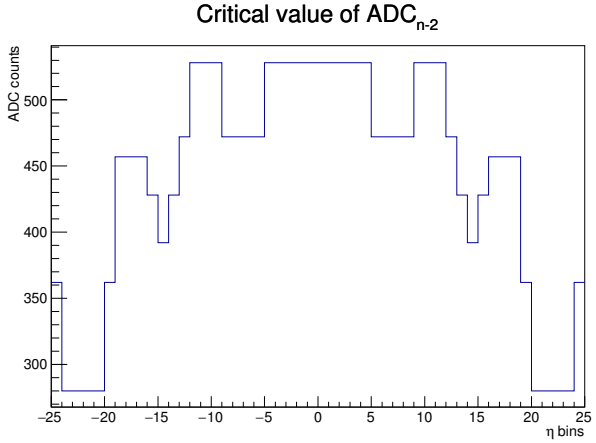

Figure 6.3: Critical value for the ADC_{n-2} sample, calculated with Equation 6.5 for the autocorrelation coefficients used at the beginning of Run 2.

6.3 Investigation of the PeakFinder Mistiming

The PeakFinder mistiming affects high-p_T physics events. To assess the impact on physics analyses it is necessary to know the minimum p_T, which will cause the PeakFinder to trigger early. This critical object p_T can be determined from the critical ADC_{n-2} value. In a first step physics objects are matched to the pulses they cause in the trigger towers. In a second step the value of the ADC_{n-2} sample of these pulses is correlated to the p_T of the physics objects. An example for this correlation is shown in Figure 6.4. Given a clear functional correlation, the desired critical value is the p_T corresponding to the critical ADC count.

The goal of the analysis is to find the critical p_T for each trigger tower and to identify the regions of the calorimeter, in which the PeakFinder mistiming can occur.

A suitable choice for these studies are electrons and photons. They produce only narrow showers. This is important since the splitting of the energy over several trigger towers makes the matching and correlation difficult.

In a first step, only electrons are used, as they allow for a clearer selection than photons, due to the additional track information. In a second step, photons are added to the analysis to improve the available statistics.

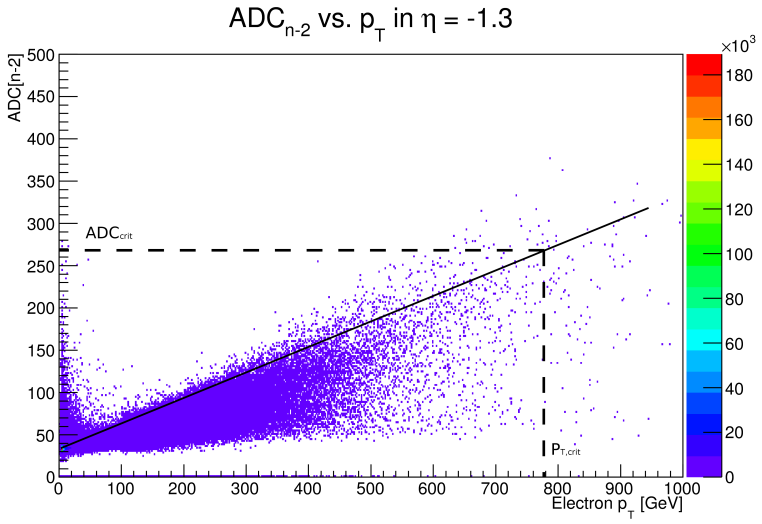

Figure 6.4: Example for the procedure to extract the critical p_T value given the critical ADC value.

6.3.1 Data Samples

The analysis presented here is based on ATLAS data from 2015 and 2016, with integrated luminosities of 3.9 fb^{-1} and 36 fb^{-1} respectively. The code has been developed using the 2015 dataset and the results have been produced with the 2016 datasets. The receiver gains in the analogue trigger chain from the calorimeters to L1Calo that determine the conversion signal pulses from V to GeV have slightly changed from 2015 to 2016. Therefore the dependence between energy deposition and pulse shape is different for the two datasets and a combination is not possible.

This analysis requires the digitized pulse shape information from the trigger towers. However this information is not needed for a typical physics analysis and is not contained in the standard ATLAS data sets. Therefore dedicated datasets produced for L1Calo purposes that contain the needed information are used. These datasets are available for special pre-selections that are already enriched with certain physics objects.

In the following the single electron and the photon/jet streams are used. The single electron stream contains only events that have at least one *medium* electron candidate with $p_T > 100$ GeV. Events in the photon/jet stream contain at least one *tight* photon candidate with $p_T > 190$ GeV.

6.3.2 Matching procedure

An important first step in the analysis is the matching of each electron candidate to the trigger tower that contains its main energy deposition. For this matching only trigger towers in the electromagnetic layer are considered. In addition $|\eta| < 2.5$ is required. This corresponds to the high-precision physics region of the LAr calorimeter and is the region covered by the ID. A ΔR-matching in η and ϕ is applied between the electron and the trigger towers in the event. For this

$$\Delta R = \sqrt{(\eta_e - \eta_t)^2 + (\phi_e - \phi_t)^2} < 0.15 \tag{6.6}$$

is required. Here (η_e, ϕ_e) are the coordinates of the electron candidate. They are determined in the reconstruction process using the barycenter of the final cluster and track information. (η_t, ϕ_t) are the coordinates of the trigger tower center. They are nominal coordinates in the sense that the center of the trigger tower was defined to be at this location during the design phase with respect to the nominal interaction point.

Initial studies have shown that this coordinate system does not match with the coordinate system of the offline electrons, which is defined with respect to the primary vertex of the event. For this reason the matching requirement $dR < 0.15$ was chosen, which is 1.5 time the trigger tower extension in $\eta \times \phi$ and should cover the mismatch in the coordinate systems. In a second step the correct tower is chosen from all possible matches by selecting the trigger tower with the highest deposited E_T.

6.3.3 Electron Selection

An example for the correlation of a raw electron sample is shown in Figure 6.4. A wide spread of the ADC_{n-2} value for a given electron p_T is visible. This is not expected, since two electrons that deposit the same energy in a trigger tower, also cause pulses of the same height. Therefore an electron identification algorithm is used to select a clean electron sample with the aim of reducing the spread of the ADC_{n-2} value.

The identification algorithm uses the three working points *Loose*, *Medium* and *Tight*. For this study, all three working points have been examined.

The result of the selections is shown in Figure 6.5. The left panel shows the p_T distribution of the selected electrons. The right panel shows the resulting correlation between the ADC_{n-2} sample and p_T. The sharp edge that is visible around 100 GeV is caused by the preselection applied on the data sample as described in Section 6.3.1. It is already enriched with *Medium* electron candidates with $p_T > 100$ GeV.

In the spectra it is visible that already the *Loose* selection provides a strong rejection, especially for p_T below 100 GeV. This leads to a reduced spread for this energy region as shown in Figure 6.5d. The same is true for the working points *Medium* and *Tight*. There is some rejection at higher p_T, but the main rejection happens below 100 GeV.

To achieve a cleaner electron sample an additional selection for Z bosons is used. The Z can decay to an electron-positron pair and the invariant mass of the decay products equals the mass of the Z ($M_Z = 91.2$ GeV). This information can be used to select electrons produced in Z decays, by requiring a pair of electrons with an invariant mass $M_{ee} = M_Z \pm 10$ GeV.

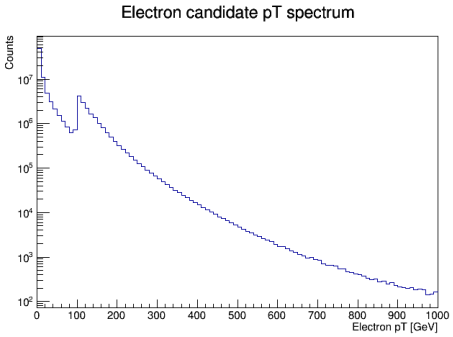

(a) No selection applied.

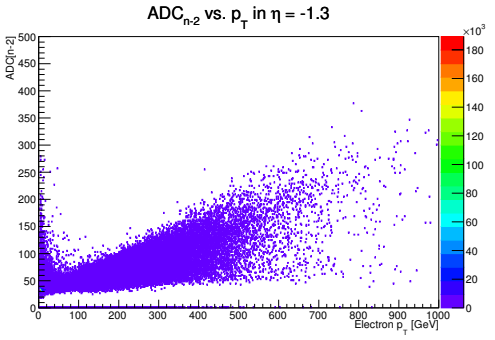

(b) No selection applied.

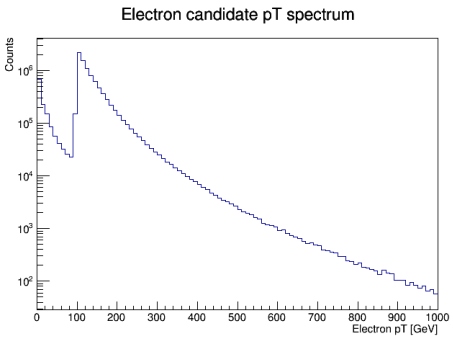

(c) Electrons passing *Loose* selection.

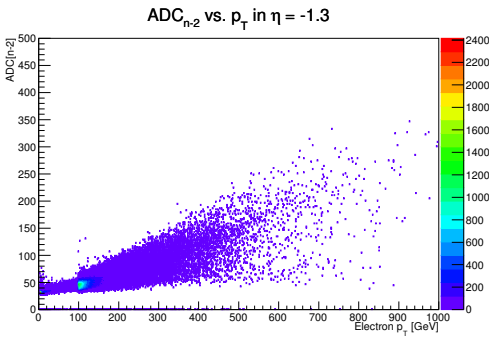

(d) Electrons passing *Loose* selection.

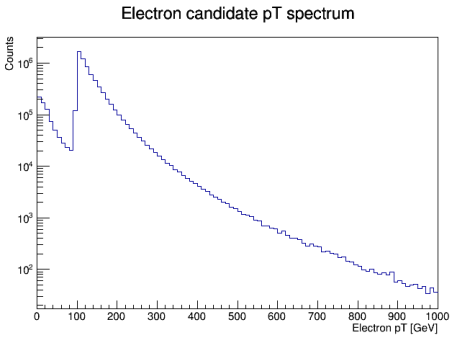

(e) Electrons passing *Medium* selection.

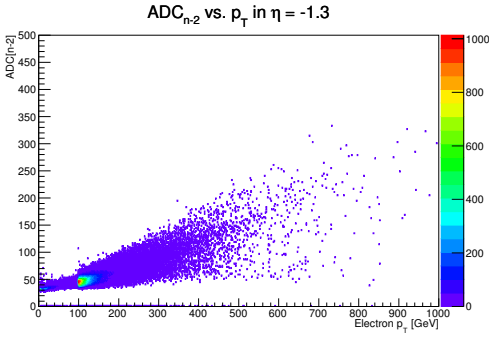

(f) Electrons passing *Medium* selection.

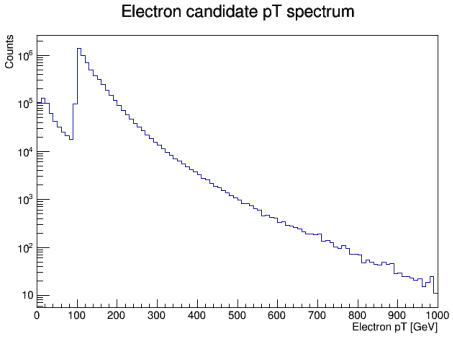

(g) Electrons passing *Tight* selection.

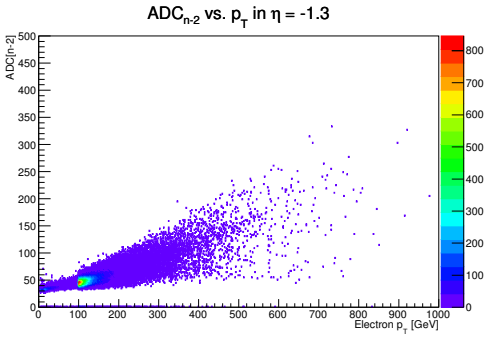

(h) Electrons passing *Tight* selection.

Figure 6.5: Left panel: p_T distribution of selected electron candidates. Right panel: ADC_{n-2} sample as a function of p_T for the corresponding selection.

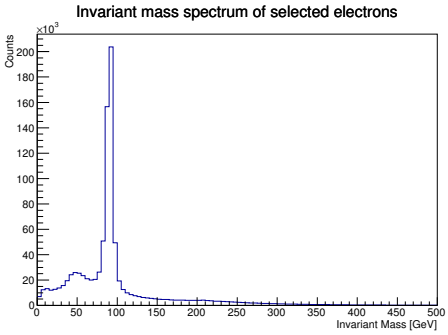

(a) Two *Loose* electrons.

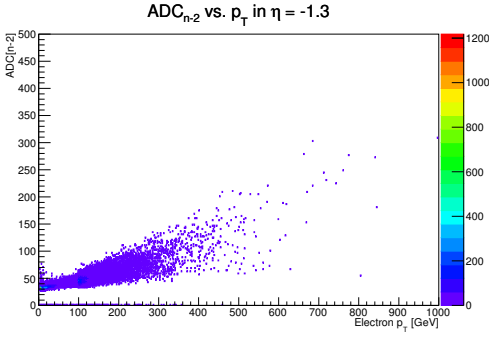

(b) Two *Loose* electrons.

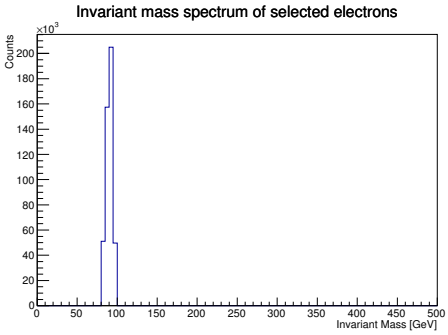

(c) Selection a), cut at $M_{ee} = M_Z \pm 10\,\text{GeV}$.

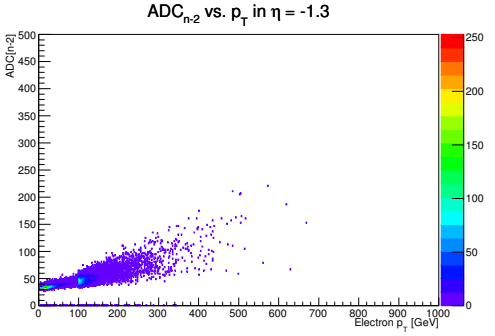

(d) Selection b), cut at $M_{ee} = M_Z \pm 10\,\text{GeV}$.

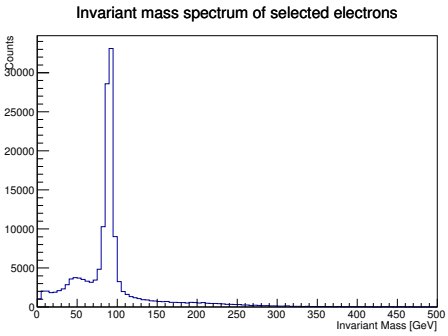

(e) One *Medium* and one *Tight* electron.

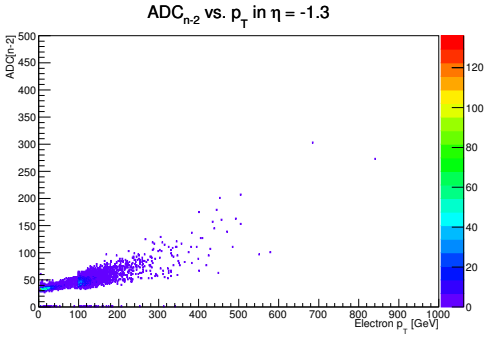

(f) One *Medium* and one *Tight* electron.

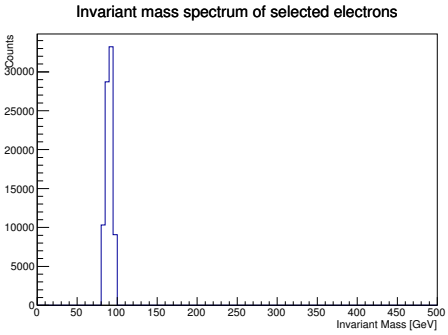

(g) Selection e), cut at $M_{ee} = M_Z \pm 10\,\text{GeV}$.

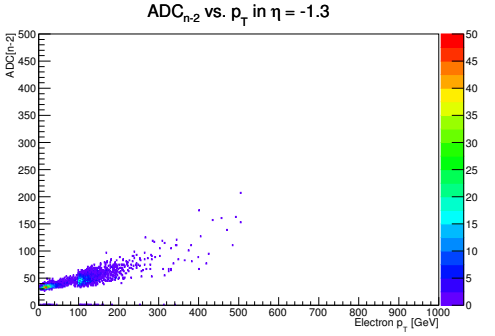

(h) Selection f), cut at $M_{ee} = M_Z \pm 10\,\text{GeV}$.

Figure 6.6: Left panel: invariant mass distribution of selected electron candidates. Right panel: ADC_{n-2} sample as a function of p_T for the corresponding selection.

Different combinations of identification working points can be chosen for the pair. For this study two cases are investigated. One selection requires two *Loose* electrons and one requires a *Tight* and a *Medium* electron. The results of these two selections are shown in Figure 6.6.

The panels on the left show the invariant mass distribution of electrons passing the corresponding selection, the panels on the right show the resulting correlation between ADC_{n-2} and p_T for $\eta = -1.3$. The peak at around 90 GeV in the invariant mass spectrum confirms that Z bosons were selected.

This Z-selection achieves a slightly reduced spread visible in the correlation plot, for example when comparing Figure 6.6d and Figure 6.6b. The figures show the results for the correlation when requiring two *Loose* electrons with and without Z-selection.

A further improvement is seen when requiring a *Tight* and a *Medium* electron (c.f. Figure 6.6f and Figure 6.6h). However, the available statistics are reduced as well, since also electrons that do not originate from a Z-decay are rejected. At this point it would be possible to measure the spread for each selection to quantify the improvement. However none of the selections used so far reduce the spread to an acceptable level and additional cuts are necessary. These are explained in the following chapter.

6.3.4 Additional Cuts

In addition to the electron selection a good run list (GRL) and a cut on electrons splitting their energy between trigger towers are used. The GRL contains information on the readiness status of the ATLAS detector for each run. If a subsystem is disabled or not functioning correctly during a run or part of a run and data quality is affected it will be marked in the GRL. Events not passing the GRL are excluded.

For the cleaned electron sample, there is still a sizable spread in the ADC_{n-2} distribution. This is caused by electrons hitting the border of two trigger towers and splitting their energy between them. Since the energy that is deposited in each tower is lower than the total electron energy, the trigger tower pulses and hence the digitized samples are smaller. For this study those electrons need to be excluded.

The investigation of the splitting between two towers is described in the following. Splitting over three and more towers can be neglected as discussed in [32]. For each trigger tower with a matched electron the neighboring tower with the highest energy is determined . The ratio

$$s = \frac{E_{neigh}}{E_{neigh} + E_{hit}} \tag{6.7}$$

indicates how much energy E_{neigh} was deposited in the highest energetic neighboring tower with respect to the total energy deposited in the primarily hit tower E_{hit} and the neighboring tower E_{neigh}. The variable s is used to quantify the splitting. A distribution of s is shown in Figure 6.7. It is clearly visible that splitting is a sizable effect even to the point that the electron energy is split equally between two towers. The sharp drop at $s = 0.5$ demonstrates the good efficiency of the matching described above. Larger values of s than 0.5 indicate that the energy in the neighboring tower is higher than the energy in the matched tower. This happens very rarely, but does not necessarily indicate a mismatch, since it can also be caused by a second particle impacting in the neighboring tower.

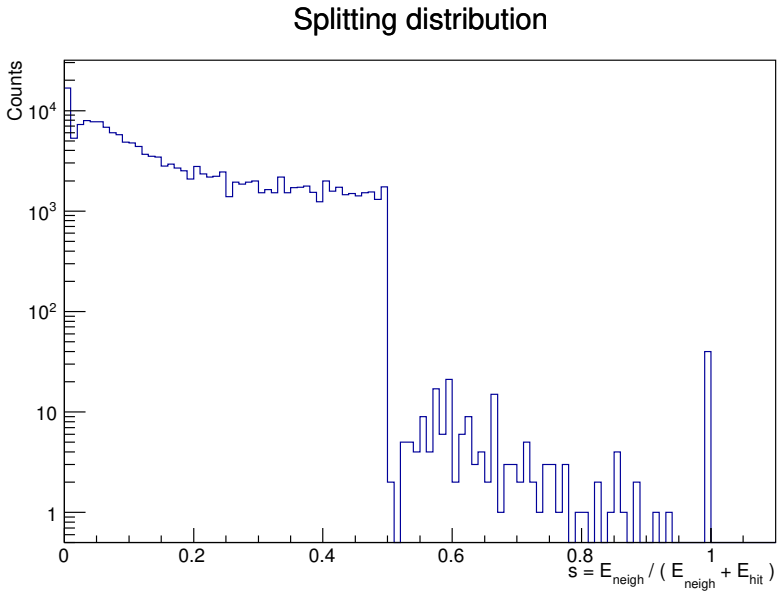

Figure 6.7: Distribution of splitting variable s for electron candidates passing the Z selection with one *Tight* and one *Medium* electron.

The selection of the cut value is a trade-off between the width of the spread and the statistics necessary to see the correlation. In this study requirement $s < 0.05$ is chosen to provide a good reduction of the spread. The results are shown in Figure 6.8. The distribution of s is displayed on the left panels and the correlation after cutting all events with $s > 0.05$ on the right panels. Comparison to Figure 6.6 shows an improvement of the spread, especially using the selection with one *Tight* and one *Medium* electron.

6.3.5 Electron Results

The electron sample obtained with the Z-selection using one *Tight* and one *Medium* electron and the cuts described in the previous section are used to determine the critical p_T for electrons as a function of η. A fitting procedure is used to extrapolate the correlation between ADC_{n-2} and p_T to the critical ADC value, to compensate for the lack of statistics at higher energies. It is assumed that the ADC_{n-2} sample grows linearly with energy. Therefore the fit function

$$f(x) = p_0 x + 32 \tag{6.8}$$

is chosen, where the slope p_0 is a free parameter and the offset is set to the pedestal value. The fit is performed for each η slice. The fit result for $\eta = -1.3$ is shown in Figure 6.9.

The critical p_T is determined from the slope and the critical ADC (cf. Figure 6.3) as

$$p_{T,crit} = \frac{ADC_{crit} - 32}{p_0}. \tag{6.9}$$

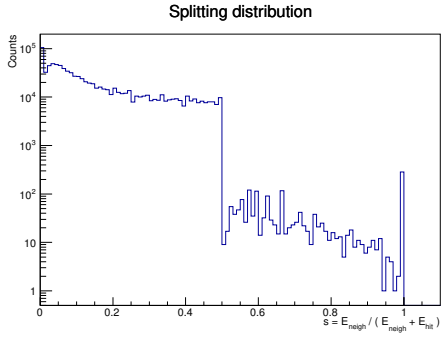

(a) Selection requires two *Loose* electrons.

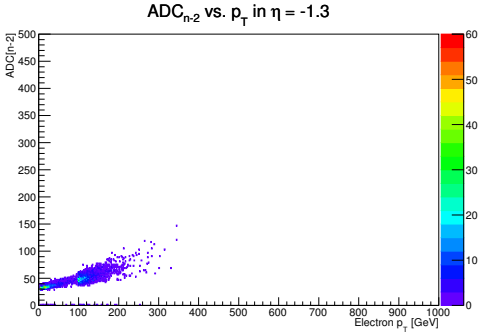

(b) Selection requires two *Loose* electrons.

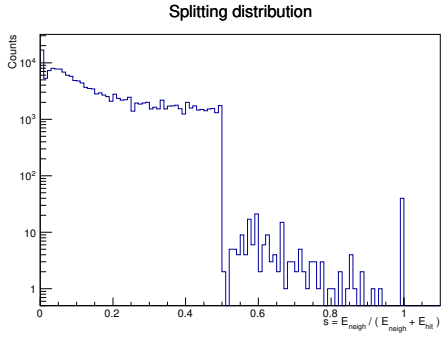

(c) Selection requires one *Tight* and one *Medium* electron.

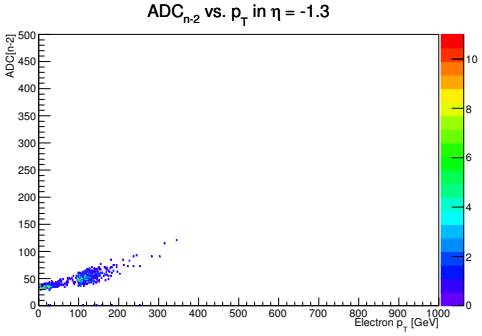

(d) Selection requires one *Tight* and one *Medium* electron.

Figure 6.8: Left panel: Splitting distribution for different electron selections. In both cases a cut around $M_{ee} = M_Z \pm 10\,\text{GeV}$ is applied. Right panel: ADC_{n-2} sample as a function of p_T for the corresponding selection and an additional cut on the splitting. Only electrons with $s < 0.05$ are accepted.

The uncertainty on the critical p_T is calculated from the uncertainty on the slope p_0 using gaussian error propagation. The resulting values for $p_{T,crit}$ are shown in Figure 6.10 (black dots) for $|\eta| < 2.4$, together with the maximum p_T that can be reached by a single electron (red dots) in the same η slice. Neglecting the electron mass, the maximum p_T is given by

$$p_{T,max} = \frac{6.5\,\text{TeV}}{cosh\,(\eta)}. \tag{6.10}$$

It depends on the emission angle of the particle with respect to the beam direction and is limited by maximum energy the $E = 6.5\,\text{TeV}$ that a single particle can obtain at the LHC during Run 2. It follows that PeakFinder mistiming can occur only in the region $0.8 < |\eta| < 1.6$, where the critical p_T is below $p_{T,max}$. The mistimed events listed in Table .1 are indeed nearly all found in that region. However their p_T is below the critical p_T determined here. One possible explanation is a non-linearity of the ADC_{n-2} sample with p_T that is not visible, due to the lack of statistics at higher transverse momenta. This non-linear rise would reduce the critical p_T. To determine if this is the case photons are added to the analysis to improve the statistics.

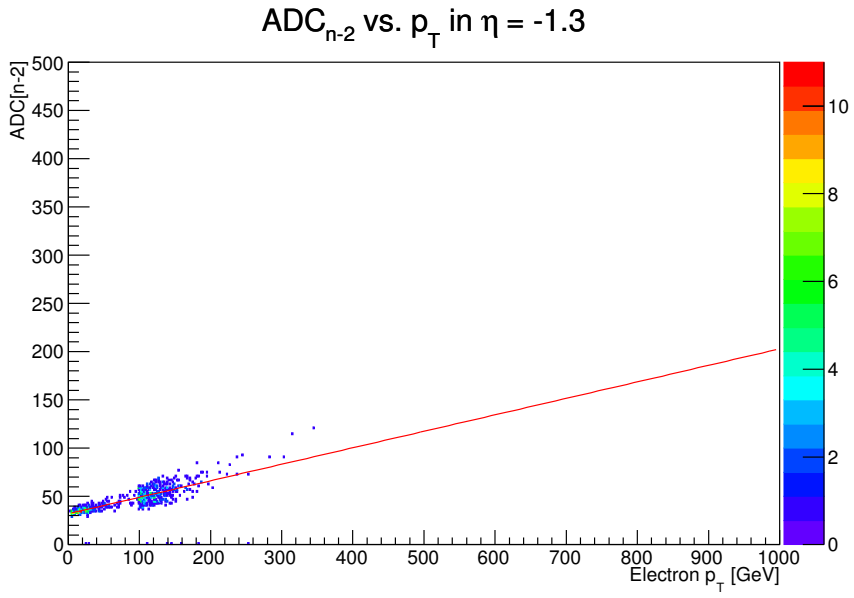

Figure 6.9: Linear fit result for selected electrons. The linear function is used to extrapolate to ADC_{crit} and determine $p_{T,crit}$.

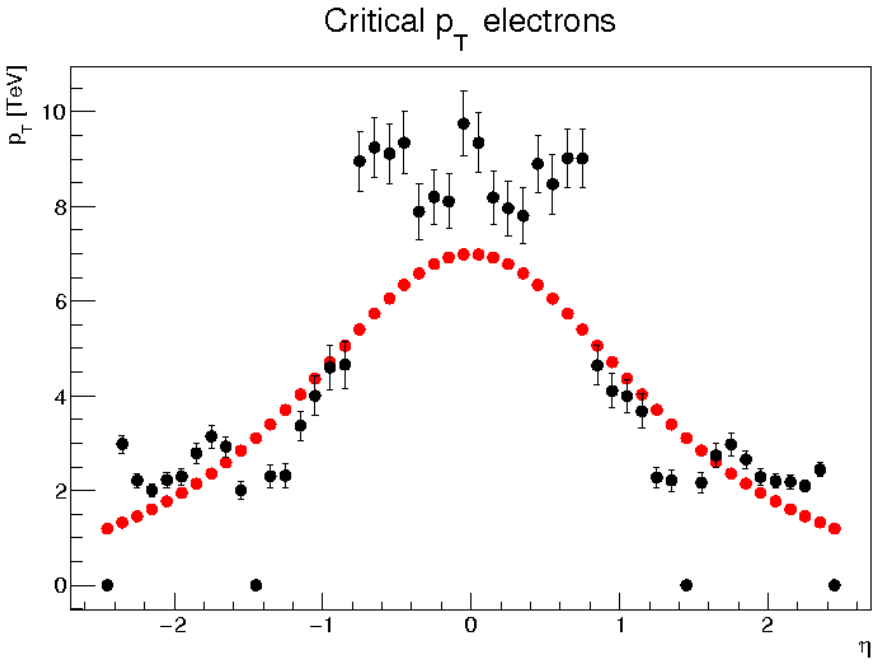

Figure 6.10: The critical p_T for electrons is shown in black. It was determined with a linear fit. The red curve shows the maximum p_T that can be reached for a given η at the maximum LHC energy during Run 2.

6.3.6 Photon Selection

The statistics in the analysis is extended with the inclusion of photons. The selection is similar to that of the electrons. Events are required to pass the GRL and the calorimeter crack region is excluded ($1.37 < |\eta| < 1.52$). An overlap removal is performed to avoid double-counting of electrons and photons. The photon identification has two working points, *Loose* and *Tight*. To obtain a clean photon sample the *Tight* working point is used in this study.

The p_T distribution of the photon candidates before and after selection are shown in Figure 6.11a and Figure 6.11c. The sharp edge in the spectrum is caused by the preselection that has been used to produce the underlying dataset. Each event is required to contain at least one *Tight* photon with $p_T > 190$ GeV. This is also the reason, why the main rejection of the *Tight* selection happens below 190 GeV. The spread in the correlation plots shown in Figure 6.11b and Figure 6.11d is therefore mainly reduced in the energy region below 190 GeV.

As for the electrons, a cut on the splitting variable s is used. Only photons are accepted that fulfill $s < 0.05$. The splitting distribution is shown in Figure 6.11e and the resulting correlation is shown in Figure 6.11f. The spread is reduced by the cut, but still larger than expected. The reason for the remaining spread was found to be a slight ϕ dependence of the pulse shape, which is explained in the following section.

6.3.7 Combined Results

For the final results the electron and photon samples are combined. This yields high enough statistics to consider the correlation between ADC_{n-2} and p_T on trigger tower level. The correlation plots for four single trigger towers are shown in Figure 6.12. The spread on trigger tower level is much smaller than for the correlation plots with all towers in one η slice merged together. This can be seen by comparing the single tower correlation plots in Figure 6.12 with Figure 6.11f.

The reason for the higher spread, when considering η slices, is the ϕ dependence of the pulse shape. It is caused by the different cable length from the detector to the L1Calo receiver system for different trigger towers. A longer cable leads to a stronger attenuation of the signal and to a lower height of the pulse. Therefore the deposition of the same energy in two trigger towers with different ϕ coordinates results in a different height of the ADC_{n-2} sample.

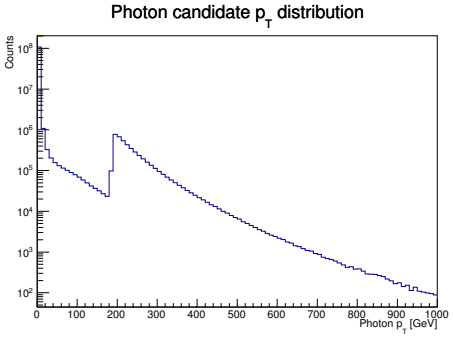

(a) No selection applied.

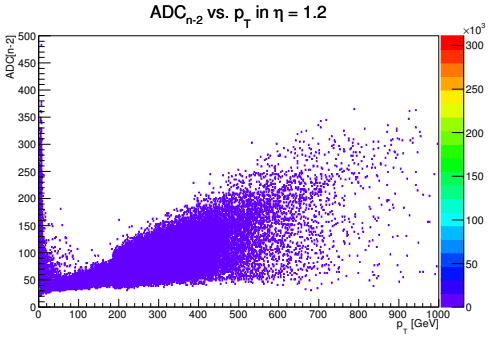

(b) No selection applied.

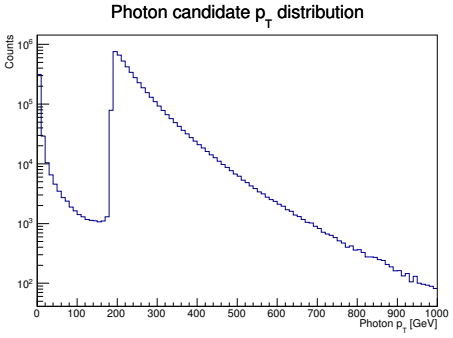

(c) *Tight* selection applied.

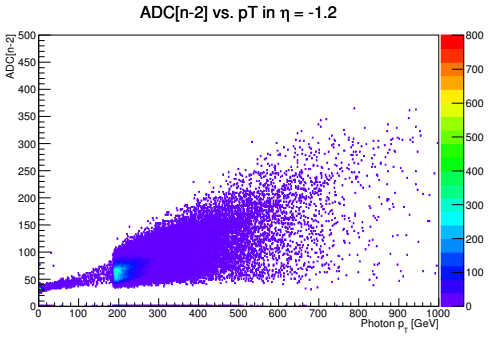

(d) *Tight* selection applied.

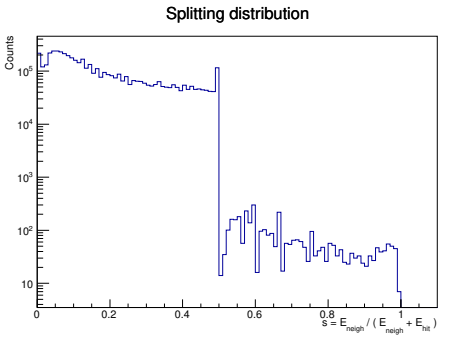

(e) *Tight* selection applied.

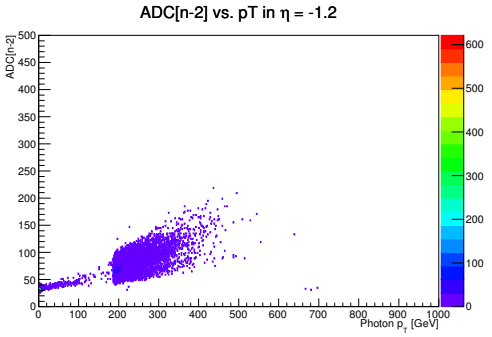

(f) *Tight* selection and cut on splitting ($s < 0.05$) applied.

Figure 6.11: Top left and middle left panel: p_T distribution of selected photon candidates. Bottom left panel: Splitting distribution. Right panel: ADC_{n-2} sample as a function of p_T for the corresponding selection and an additional cut on the splitting. Only photons with $s < 0.05$ are accepted.

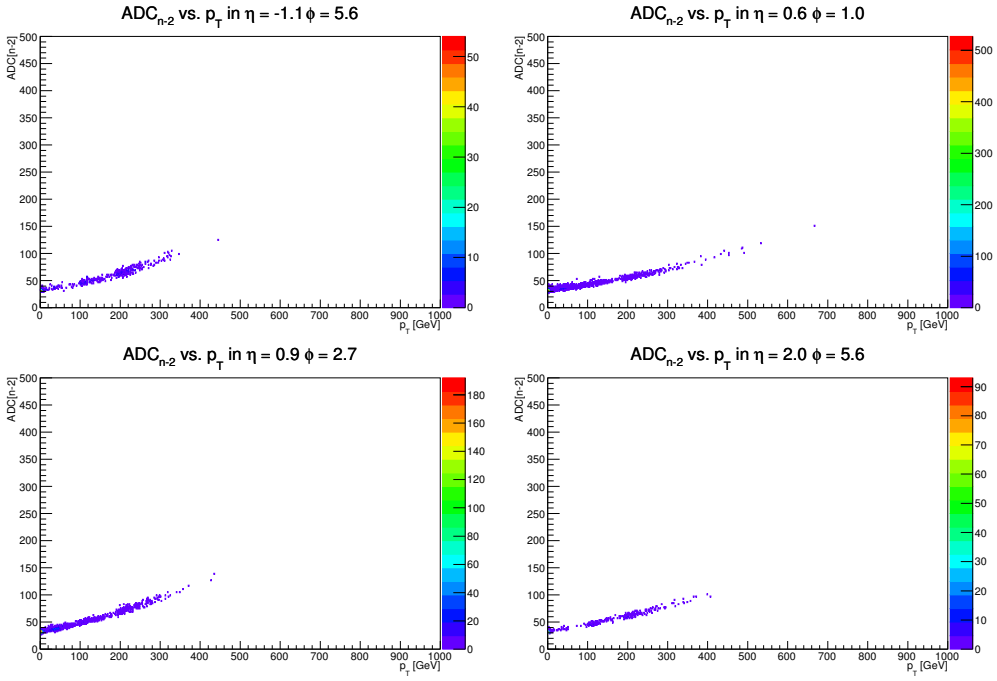

Figure 6.12: ADC_{n-2} sample as a function of p_T for single trigger towers.

With the statistics of the combined electron and photon sample the critical p_T can be determined on trigger tower level. Here, the linear extrapolation procedure explained in Section 6.3.5 is used. An η-ϕ map of the critical p_T is shown in Figure 6.13.

PeakFinder mistiming can only occur in trigger towers if the critical p_T is below this maximum p_T. An η-ϕ map with tower that fulfill this condition, is shown in Figure 6.14. As before the PeakFinder mistiming is mainly expected for $0.8 < |\eta| < 1.6$. However, in contrast to the expectation form the η-averaged results, now also trigger towers with $0.8 < |\eta|$ and $|\eta| > 1.6$ are affected.

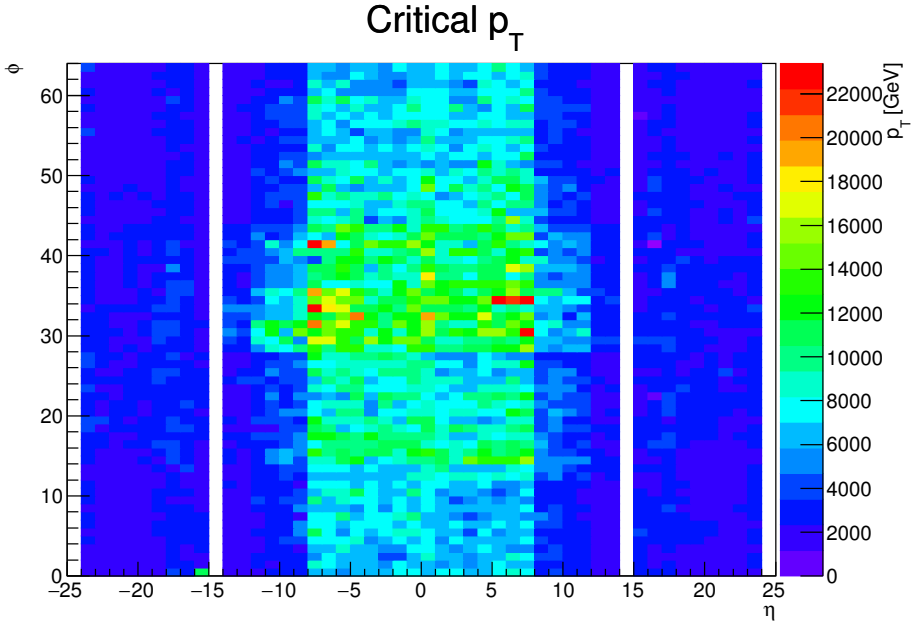

Figure 6.13: The critical p_T for the combined samples on trigger tower level.

Several of mistimed electromagnetic objects that lead to this analysis, were reported to have a lower p_T than the critical p_T (c.f. Table .1). One possible explanation is a stronger than linear rise of the ADC_{n-2} sample with p_T. This would lead to a lower value for $p_{T,crit}$. To estimate this possibility a quadratic fit of the form

$$f(x) = p_0 x + p_1 x^2 + 32 \tag{6.11}$$

is used. To increase the statistics for the fit, all trigger towers with the same η coordinate are combined. For each p_T bin, the average value and the rms of the ADC_{n-2} sample are calculated. The average value is used as the data point for the p_T bin and the Root Mean Square as the uncertainty. This way the spread is correctly taken into account during the fit. The fit result for $\eta = -1.9$ is shown in Figure 6.15. The quadratic coefficient p_1 is non-zero, which confirms a non-linear behavior of the ADC_{n-2} sample.

Figure 6.16 shows the critical p_T determined with the quadratic and linear fits in bins of η. The maximum p_T that can be reached in a given η bin is also shown. The critical p_T

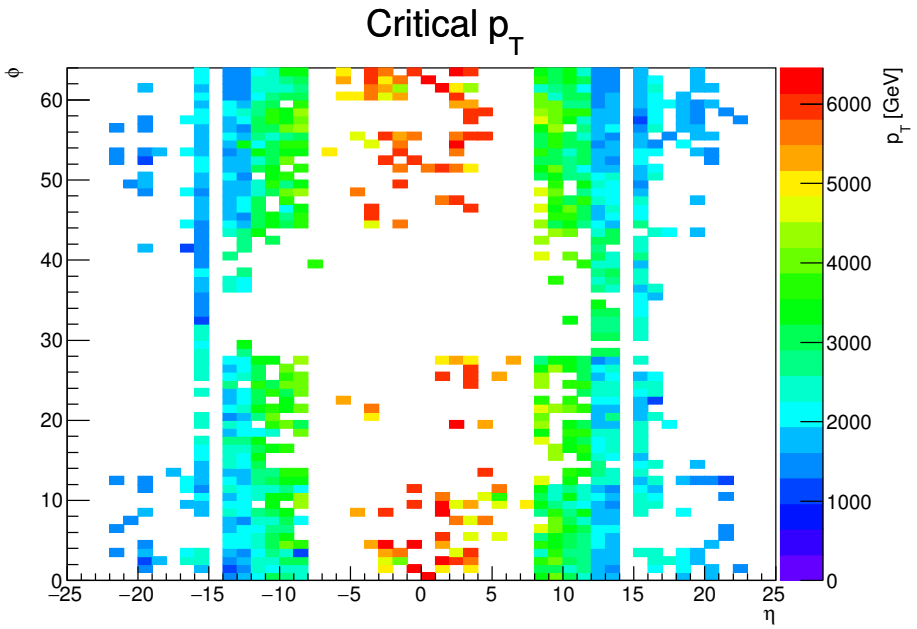

Figure 6.14: The critical p_T for the combined electron and photon sample on trigger tower level. Only towers are filled which have a critical p_T smaller than the maximum p_T possible in the tower.

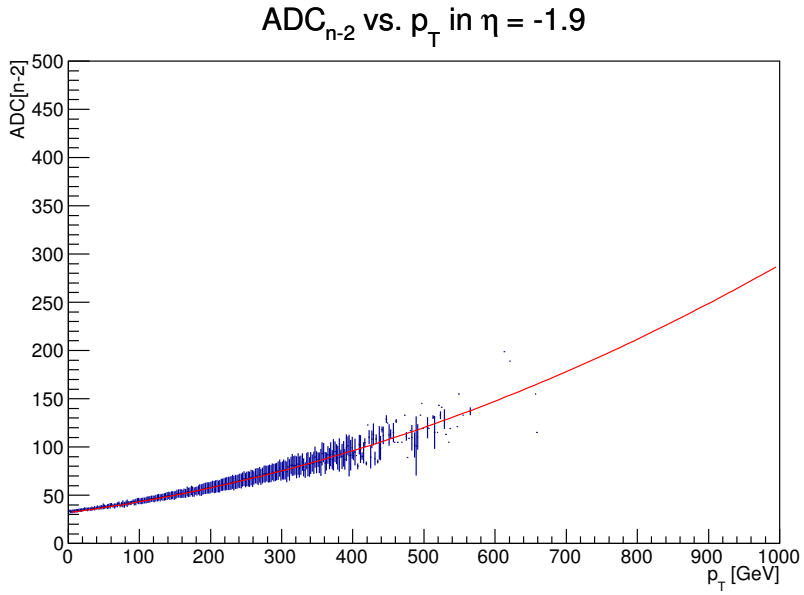

Figure 6.15: Quadratic fit result for $\eta = 1.9$ and combined electron and photon samples.

determined with the linear fit is lower for the combined dataset than for the electron sample

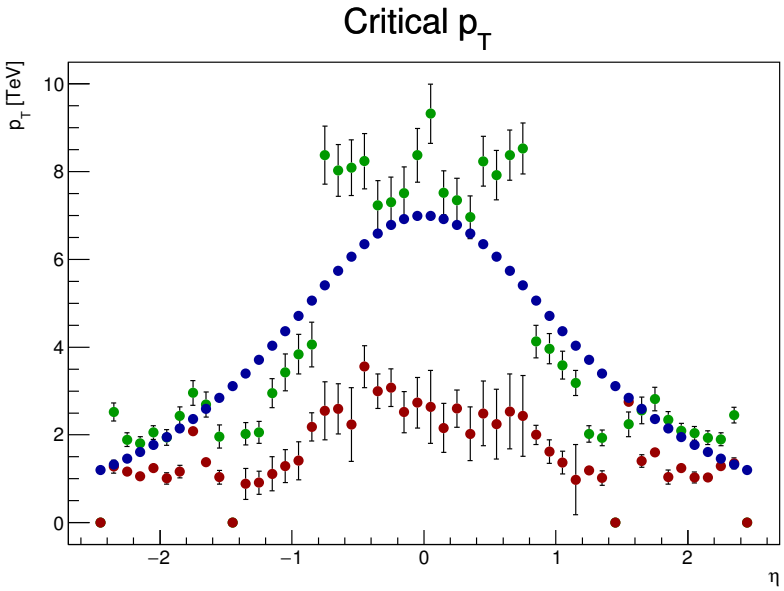

Figure 6.16: The critical p_T as a function of η obtained with a linear fit (green) and a quadratic fit (red). The maximum p_T as a function of η is shown in blue.

alone (c.f. Figure 6.10). This is due to the additional statistics at high p_T that show a stronger than linear rise of the ADC_{n-2} sample.

The critical p_T values obtained from the quadratic fit are considerably lower, below 3 TeV for most of the calorimeter and well below the maximum p_T. This indicates the possibility of PeakFinder mistiming for the whole region of the electromagnetic calorimeter.

However, it is not known, up to which energy the quadratic extrapolation holds. Since only around 120 events were mistimed in the whole 2015 data (Total Luminosity $L = 3.9fb^{-1}$), it is unlikely that the critical p_T is as low as suggested by the quadratic fit. Otherwise more mistimed events would have been expected.

It is not possible to give a final result with the available statistics, since the behavior of the ADC_{n-2} sample at high p_T is not known. However, the results for the critical p_T from the linear and the quadratic extrapolation can be taken as the upper and lower limiting case, with the true critical p_T in between.

The PeakFinder mistiming was solved for the 2016 data taking by the introduction of a new decision logic. The validation of this decision logic is described in the next chapter.

7 Analysis of the PeakFinder Mistiming in Calibration Data

In the previous chapter the PeakFinder mistiming was studied in physics data. The main difficulty was the low statistics at high energies. This made an extrapolation necessary, which is problematic since the behavior of the pulse shape and the ADC samples at very high energies is not precisely known.

One possibility that allows to test the L1Calo BCID algorithms at high energies, independent of the statistics in physics data, are the pulses produced in the calibration boards of the calorimeters. The upper transverse energy limits of these pulses are 3.5 TeV for Tile and 7.5 TeV for LAr and are given by the maximum charge that can be injected. A description of the LAr calibration system can be found in Section 3.2.4, for the Tile calibration system more information is available in [51].

In the first part of this chapter the PeakFinder mistiming is reproduced using the calibration system. In the second part the validation of the new decision logic, which prevents the PeakFinder mistiming is described. This validation was performed with the calibration systems of both ATLAS calorimeters.

7.1 General Properties of the Calibration System

The calibration system works with discrete energy steps. At each energy step the calorimeters are pulsed. This means that a given charge is injected in each cell of the calorimeter. The readout of the injected pulses follows the same path as real physics signals, hence for each time the calorimeter is pulsed an event is generated.

For L1Calo usually a ramp with steps of increasing energy is used. One full run over all steps is called a calibration or "pulser" run, since the system is also referred to as "pulser system". The pulser runs used in this thesis all have 200 events per energy step. An important criterion for the usability of the system is the stability of the energy pulsed in each step. The energy spectrum of a LAr trigger tower in the electromagnetic layer is shown in Figure 7.1 for a low ($E_T < 600\,\text{GeV}$) and a high energy ($1000\,\text{GeV} < E_T < 7000\,\text{GeV}$) pulser run. The small relativ width ($\sigma_E = 0.38\,\text{GeV}$ for 420 GeV) of the peaks in the spectrum demonstrates that the energy steps are very stable. For higher energies the width increases slightly, but the energy step remains well defined ($\sigma_E = 3.75\,\text{GeV}$ for 7200 GeV). All results shown in the following are always produced from one event in a given step. However, it was verified in each case that they are stable for all events in the step.

Apart from the high energies that can be injected, pulser runs have several other advantages over physics data. In each event all L1Calo trigger towers are pulsed at the same time. This allows for systematic studies of the behavior of the BCID algorithms in different η regions and for different energies. Since the pulses are injected by the calibration electronics and their rise time is well known, the L1A that triggers the readout is given directly by the LAr electronics. This feature can be used to verify the correct performance of the L1Calo BCID algorithms, as they take a an independent decision, which can be compared to the correct decision of the LAr electronics.

One caveat however are the pulse shapes of the pulses injected by the calibration system. As described in Section 3.2.4 they are designed to be very similar to physics pulses, but there

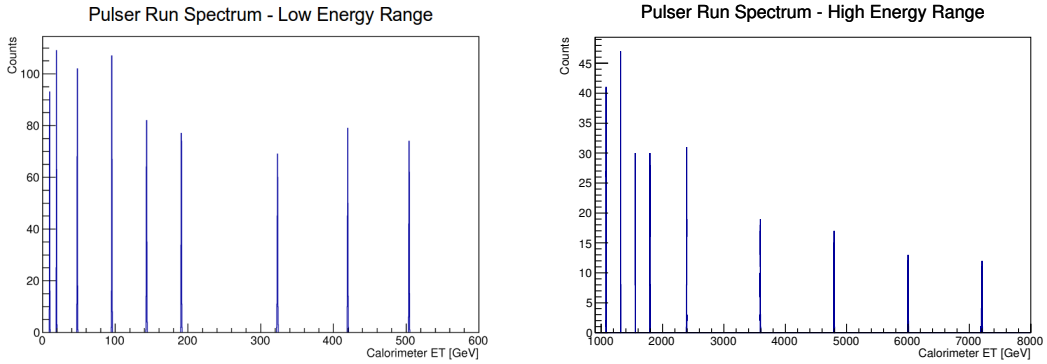

Figure 7.1: Spectra of two pulser runs for one trigger tower in the LAr calorimeter. Each peak contains 200 events.

are still differences due to the different shape of the injected pulse. This has to be kept in mind when interpreting results derived with pulser runs.

7.2 Analysis Strategy

The goal of the pulser analysis is to observe the onset of the PeakFinder mistiming. As explained in the previous section, the LAr electronics issues a trigger for the correct BC. The L1Calo readout that follows the L1A contains the information which BCID algorithms would have identified this BC. It is encoded in a 3 bit word called the "PSE bits", where P stands for the PeakFinder decision, S for the Sat40 decision and E for External BCID decision. If a bit is set, it means that the corresponding algorithm has identified the correct BC (c.f. Section 4.2.3). The decoding of the PSE bits is shown in Figure 7.2. The 3 bit word is converted to a decimal value and displayed in an $\eta - \phi$ map to show the algorithm decisions for all towers in the electromagnetic calorimeter.

Sat40 only	$(010) = 2$
Peakfinder only	$(100) = 4$
Peakfinder & Sat40	$(110) = 6$

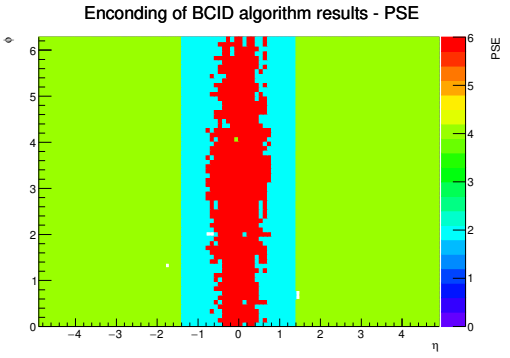

Figure 7.2: Decoding of the PSE bits that contain the decision of the BCID algorithms. The left hand panel shows the most common combinations. The right panel shows an η-ϕ map of the electromagnetic layer of the calorimeter with the decoded decimal value of the PSE bits per trigger tower.

A misidentification of the BC by the PeakFinder is seen in the PSE plot as $P = 0$ ($PSE = 1 \dots 4$). This can have two reasons. Either the PeakFinder fires early on $n-1$, which corresponds to the PeakFinder mistiming. Or the PeakFinder fires late on $n + 1$, which is the expected behavior in the high saturation regime (c.f. Section 4.2.1). To distinguish these two cases additional information is necessary.

It is provided by the LUT output. As explained before the peakfinding scheme guarantees that if a BC is identified, the following BC cannot contain a peak. Hence for the following BC the LUT value is set to zero. Therefore, for early triggers on $n - 1$, the data read out for the correct BC n contains LUT $= 0$. For late triggers of the PeakFinder the Sat40 algorithm is expected to trigger correctly on n and LUT $\neq 0$. It follows that if for a trigger tower the P bit is not set, the S bit is set and $LUT = 0$, the PeakFinder mistiming occured.

7.3 Reproduction of the PeakFinder Mistiming in Calibration Data

To reproduce the PeakFinder mistiming in calibration data, a pulser run with 10 steps in total and energies up to 8 TeV in the EMB was taken. Three selected steps, with low, medium and high energy are discussed here.

The low energy step is shown in Figure 7.3a. The top left plot shows the transverse energy deposition for each tower in the electromagnetic layer of the calorimeter. A clear η -dependence of E_T is visible. It is caused by the varying number of calorimeter cells per trigger tower that changes with η. As each cell is pulsed with the same energy, the total E_T per tower varies with η. In addition different partitions of the calorimeter are pulsed with different energies. The visible fluctuations of single towers are most likely caused by differences in the energy calibration, wrong timing of the injected pulses or defects. Single misbehaving towers are therefore not taken into consideration, but only changes that affect a whole η slice. The E_T for the FCAL is very large. This caused by a wrong energy reconstruction in this area. Therefore the FCAL is excluded from these studies. This is not problematic, since the FCAL is in the very forward region and the particle E_T is typically low. Therefore PeakFinder mistiming is unlikely to occur in this region.

The top right panel of Figure 7.3a shows the PSE bits for the low energy step in the electromagnetic layer of the calorimeter. The P bit is set for all trigger towers and the PeakFinder triggers correctly for whole electromagnetic calorimeter. The injected energies are too low for the Sat40 to trigger on the correct BC, except around $|\eta| = 1.6$, where the S bit is set in addition to the P bit. The proper functionality of the BCID algorithms is also confirmed by the bottom panel of Figure 7.3a, which shows non-zero LUT output for the whole calorimeter.

The situation changes for the medium energy step shown in Figure 7.3b. The energy in the EMB is roughly between 1000 GeV and 1500 GeV. The investigations presented in Section 6.3.7 predict an onset of the PeakFinder mistiming in this energy range. Indeed the PSE plot in the top right panel shows that the PeakFinder did not identify the correct bunch crossing in a band around $|\eta| = 1.0$. Here only the Sat40 triggered correctly, resulting in $P = 2$. The LUT output shown in the bottom panel confirms that PeakFinder mistiming occurs. In the same band around $|\eta| = 1.0$ the towers have $LUT = 0$.

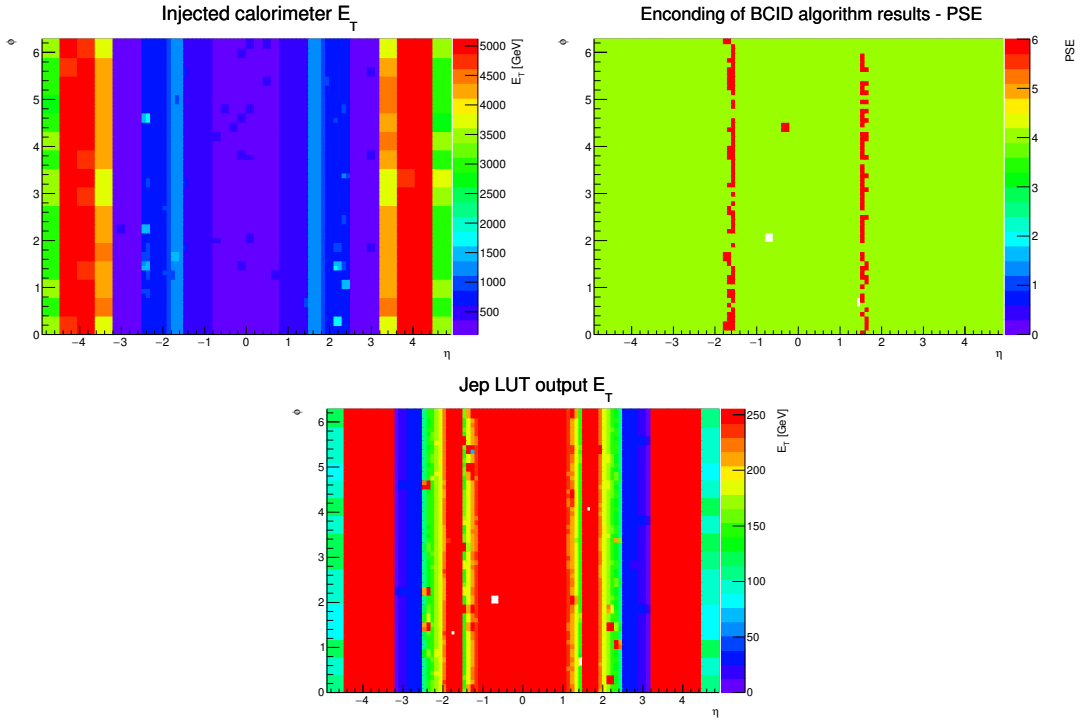

(a) Low energy step.

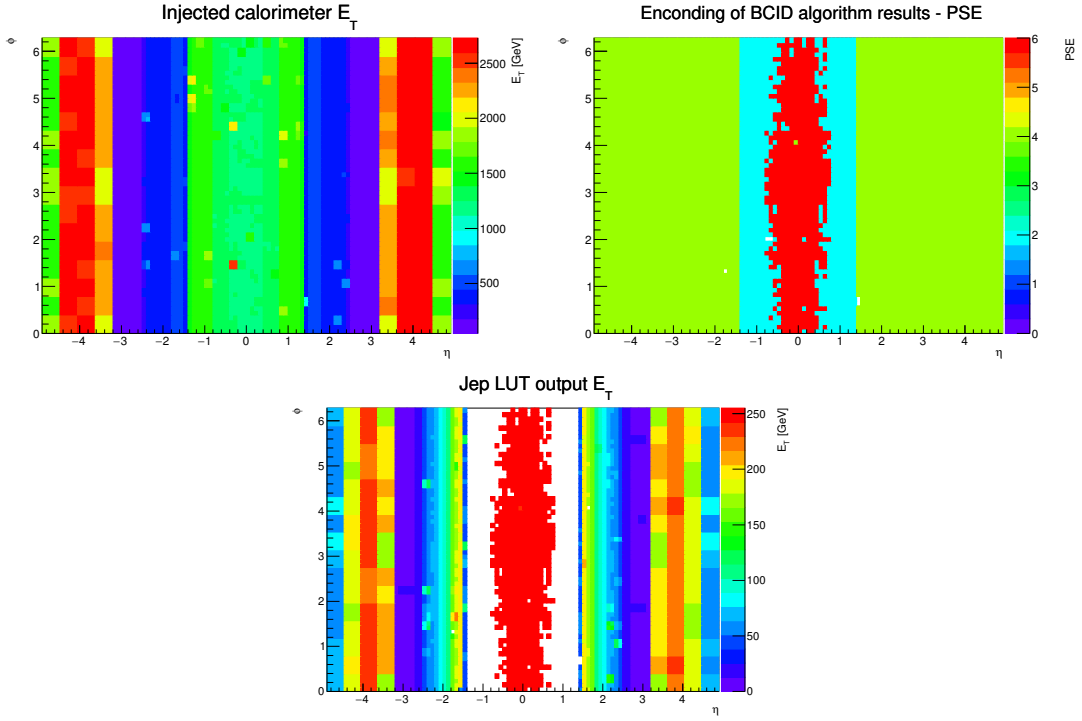

(b) Medium energy step.

Figure 7.3: Results of low (top) and medium (bottom) energy pulser run steps. For each step the E_T per tower (top left panel), the PSE plot (top right panel) and the LUT output per tower (bottom panel) is shown.

The high energy step is displayed in Figure 7.4. The energies shown in the η-ϕ map on the top left are very high, above 6 TeV in the EMB. At these energies the PeakFinder mistiming affects large parts of the calorimeter. Comparing the PSE plot in the top right and the LUT output in the bottom panel, one can see that the mistiming now occurs in the whole EMB and the EMEC inner wheel. This shows the urgency to prevent the PeakFinder mistiming, since interesting physics events with high energy deposits above 1 TeV in single trigger towers are not triggered correctly for an increasing region of the calorimeter. The solution chosen for the this issue is presented in the next section.

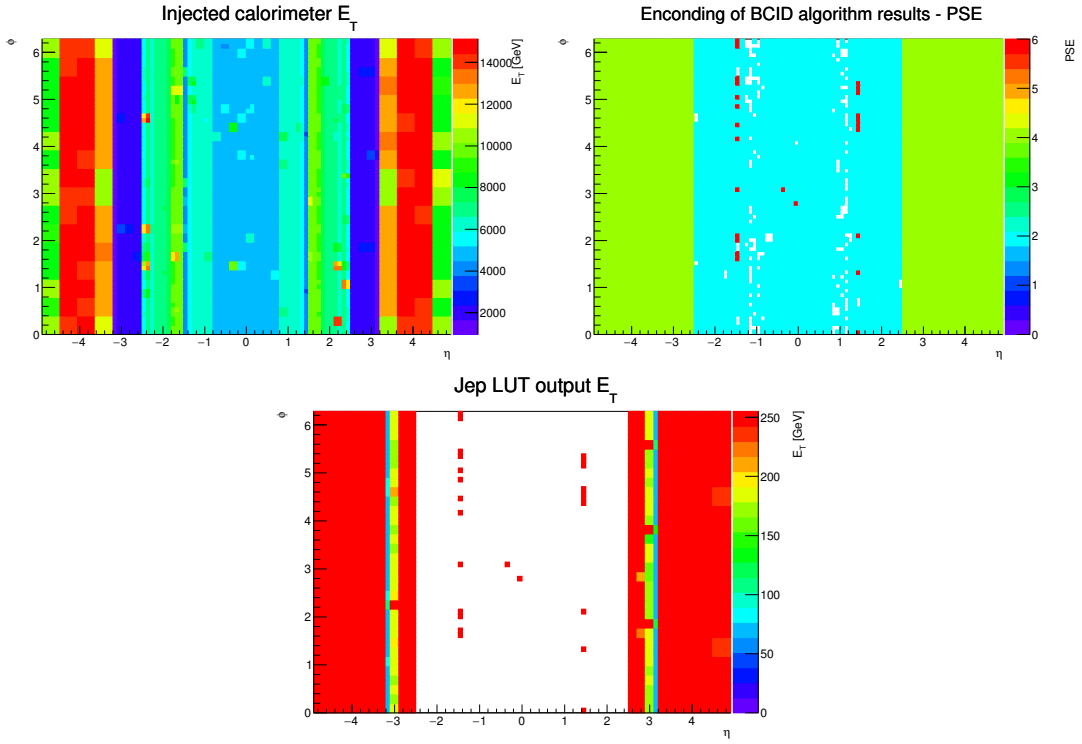

Figure 7.4: Results of the high energy step of a pulser run. The η-ϕ maps show the E_T per tower (top left panel), the PSE plot (top right panel) and the LUT output per tower (bottom panel).

Another interesting feature of Figure 7.4 are the empty histogram bins in the region around $|\eta| = 1.0$ in the PSE plot. These bins correspond to trigger towers, in which both BCID algorithms fail to identify the correct BC. This is discussed in Section 7.5.1.

7.4 Solution of the PeakFinder Mistiming - The New Decision Logic

Before the beginning of the 2016 data taking, a new decision logic was implemented in the firmware of the nMCMs to solve the mistiming issue. It introduces the possibility to disable one of the BCID algorithms depending on the number of saturated samples in the pulse. An example for the function of the decision logic is shown in Figure 7.5.

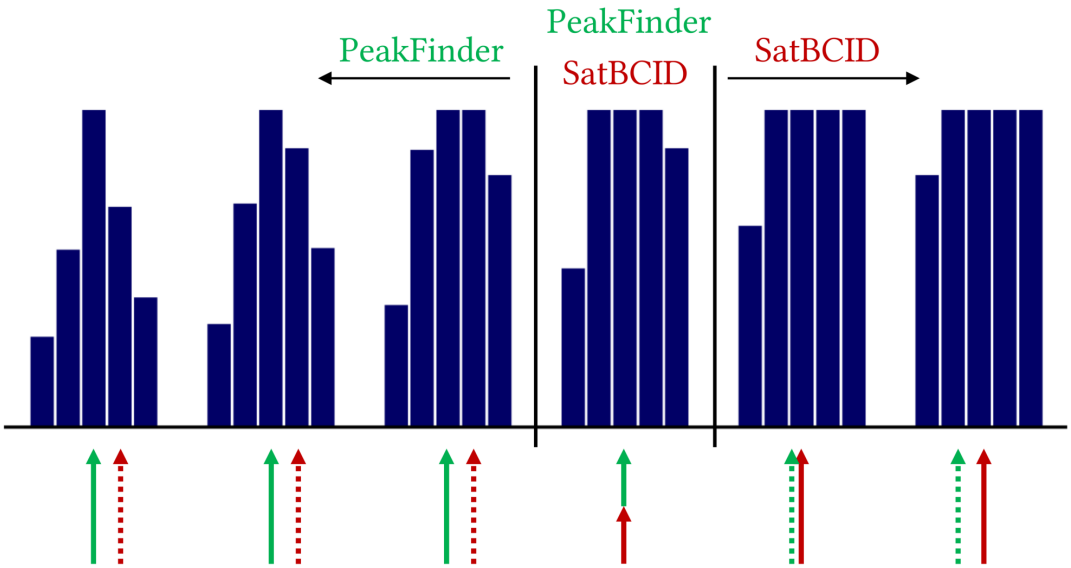

Figure 7.5: Sketch of the new decision logic. BCID algorithm decisions are accepted depending on the saturation of the pulse. In this example the PeakFinder (green) is disabled above three saturated samples, while the SatBCID (red) is disabled below three. For three saturated samples both algorithms are active. The dashed arrows indicate that the corresponding algorithm is disabled.

In the low saturation regime with up to two saturated samples, only the PeakFinder is active. In the intermediate region, with three samples saturated, both the PeakFinder and the Sat40 are active, and the earlier BC is taken. In the high saturation regime above three saturated samples only the Sat40 stays active. This prevents the PeakFinder mistiming. In the hardware the PeakFinder continues to run, however from a predefined number of saturated slices its decision is ignored for the final BCID. Nonetheless, the P bit in the readout is still set.

The nomenclature chosen to describe this restriction of the PeakFinder is PFX, where the PeakFinder is disabled for $\#SatSlices \geq X$. In principle the value X can be chosen independently for each trigger tower. But from the assumption that the PeakFinder mistiming only occurs when at least four ADC samples are saturated, the setting $X = 4$ (PF4) was initially chosen for all calorimeters.

7.5 Validation of the New Decision Logic

The validation of the new decision logic was performed in pulser runs before the start of data taking in 2016. It was validated for all parts of the calorimeter. In the following two section, only the most important results are presented, with a focus on those subcalorimeters where saturation is strongest. These are the EMB, the EMEC and the Tile calorimeter.

7.5.1 LAr calorimeter, electromagnetic layer

Figure 7.6 shows the results for the LAr electromagnetic layer in a medium energy step from a pulser run with the new decision logic enabled in PF4 mode. The top right panel shows a map of the PSE bits and it can be seen that the PeakFinder still decides for the incorrect BC for the EMB and the EMEC inner wheel, where $P = 0$ (light blue regions). However the map of the LUT output shown in the top left panel demonstrates that nearly no mistriggers are caused, since with the PF4 setting active only the Sat40 decision is taken into account for pulses with more than three saturated samples. The bottom panel of Figure 7.6 shows the number of saturated samples per trigger tower. It confirms that for most of the calorimeter the pulses have four or more saturated samples. This shows that the new decision logic works as expected and can prevent the PeakFinder mistiming for pulses with more than three saturated samples.

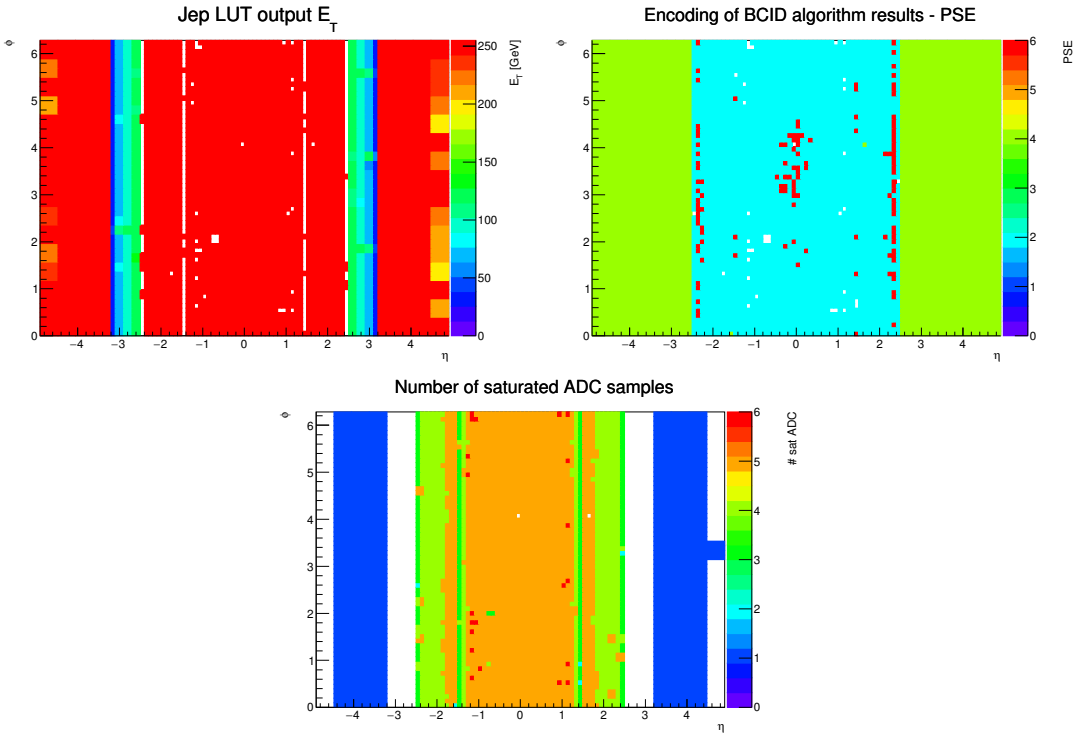

Figure 7.6: Results of the medium energy step of a pulser run with PF4 setting activated. The η-ϕ maps show the LAr electromagnetic layer with the LUT output per tower (top left panel), the PSE plot (top right panel) and the number of saturated ADC samples per tower (bottom panel).

However the slices $|\eta| = 1.4$ and $|\eta| = 2.5$ still exhibit mistriggers as can be seen by the missing LUT values. The bottom panel of Figure 7.6 shows that the pulses in the affected region have only three saturated samples. This is an indication for an earlier onset of the PeakFinder mistiming in these regions.

For further investigations a raw data event was extracted from the pulser run. The pulse

from a trigger tower at $\eta = 1.4$ is shown in Figure 7.7. It has three saturated samples and the real peak must be contained in $ADC_{n=4}$, since the correct trigger is given by the LAr electronics. Using the filter coefficients that were loaded during the pulser run, the PeakFinder decision was calculated and is shown in Table 7.1.

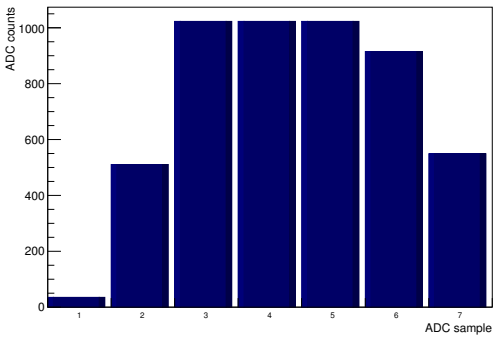

Figure 7.7: Digitized pulse from a tower in $\eta = 1.4$ with misidentified BC.

ADC samples	Filter Coefficients	PeakFinder Sum
$a_{n-3} = 35$		
$a_{n-2} = 511$	$d_{-2} = -10$	
$a_{n-1} = 1023$	$d_{-1} = 5$	$S_{n-1} = 13458$
$a_n = 1023$	$d_0 = 12$	$S_n = 11690$
$a_{n+1} = 1023$	$d_1 = 3$	$S_{n+1} = 7710$
$a_{n+2} = 915$	$d_2 = -4$	
$a_{n+3} = 549$		

Table 7.1: Calculation of the PeakFinder sums for the early triggered pulse shown in Figure 7.7.

The calculation shows that $S_{n-1} > S_n > S_{n+1}$. It confirms that the PeakFinder fires early for the pulse shown in Figure 7.7, even though only three samples are saturated. This could be an indication that the original assumption that the PeakFinder mistiming only occurs for four saturated samples is wrong. In this case the PF4 setting is not sufficient to prevent the PeakFinder mistiming and a PF3 setting is necessary.

However it has to be considered that the pulse shapes in pulser runs are different from physics pulses. In addition the problematic towers are all in $|\eta| = 1.4$, the overlap region between EMB and EMEC, and $|\eta| = 2.5$ the overlap region between the EMEC inner and outer wheel. The trigger towers in these regions contain cells from two different parts of the calorimeter that are behind each other. The delays in the transmission lines for these parts are tuned for physics data taking, where a particle first passes through the inner part and then through the outer part. To synchronize the pulses from both parts, the inner part has a longer delay than the outer part. In pulser runs however, all parts of the calorimeter are pulsed at the same time. This causes a distorted pulse shape, since the pulses do not arrive synchronously.

Hence, a similar mistiming is not to be expected in real physics events. Therefore it was decided to use PF4 in the whole electromagnetic calorimeter.

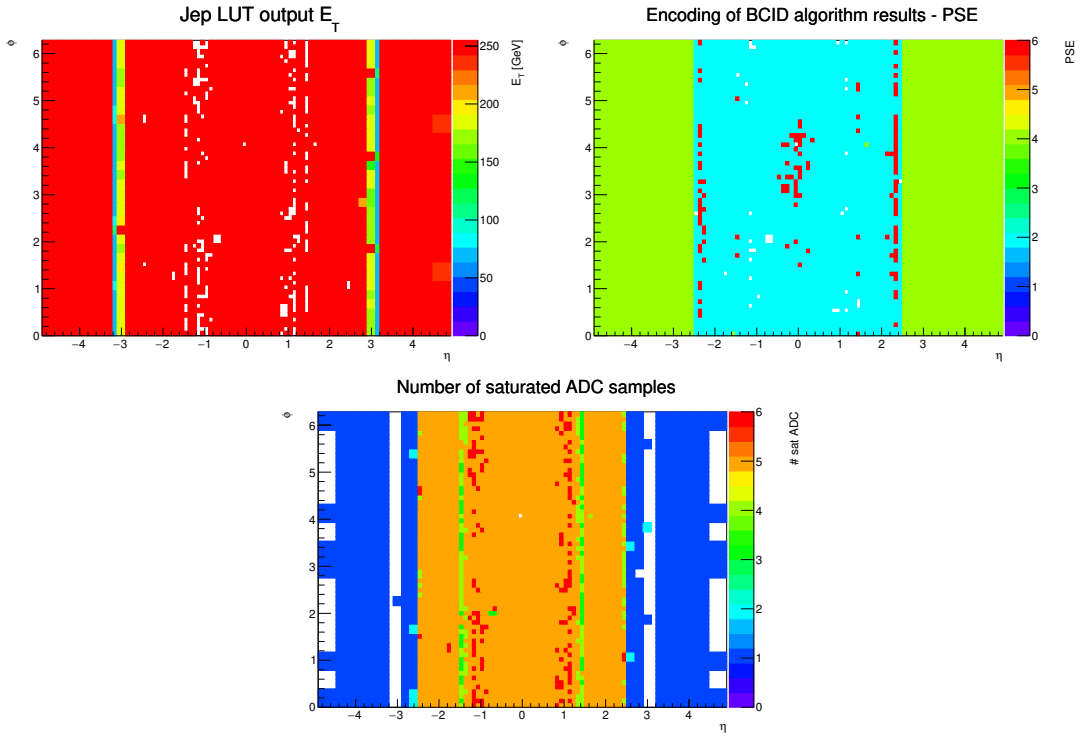

Figure 7.8: Results of the high energy step of a pulser run with PF4 setting activated. The η-ϕ maps show the LAr electromagnetic layer with the LUT output per tower (top left panel), the PSE plot (top right panel) and the number of saturated ADC samples per tower (bottom panel).

The high energy step shown in Figure 7.8 confirms the correct functionality of the decision logic. However it exhibits a new feature in the region around $|\eta| = 1.2$. Both the LUT output and the PSE bits are zero for several towers. Each of these towers has pulses with six saturated ADC samples as shown in the bottom panel of Figure 7.8. Investigation of the pulse shapes shows that this corresponds to two saturated samples before the peak sample. As explained in Section 4.2.1 the Sat40 algorithm is not able to function properly for this $s + 2$ case. Hence the pulsed energy is beyond the upper energy limit of the Sat40 algorithm. However this statement is again limited by the different pulse shapes for pulser runs and physics pulses. It is therefore not evident where the high energy limit of the Sat40 is encountered in physics data.

7.5.2 Tile calorimeter

The PF4 setting was also tested for the Tile calorimeter. The results for a low and a high energy step are shown in Figure 7.9a and Figure 7.9b respectively.

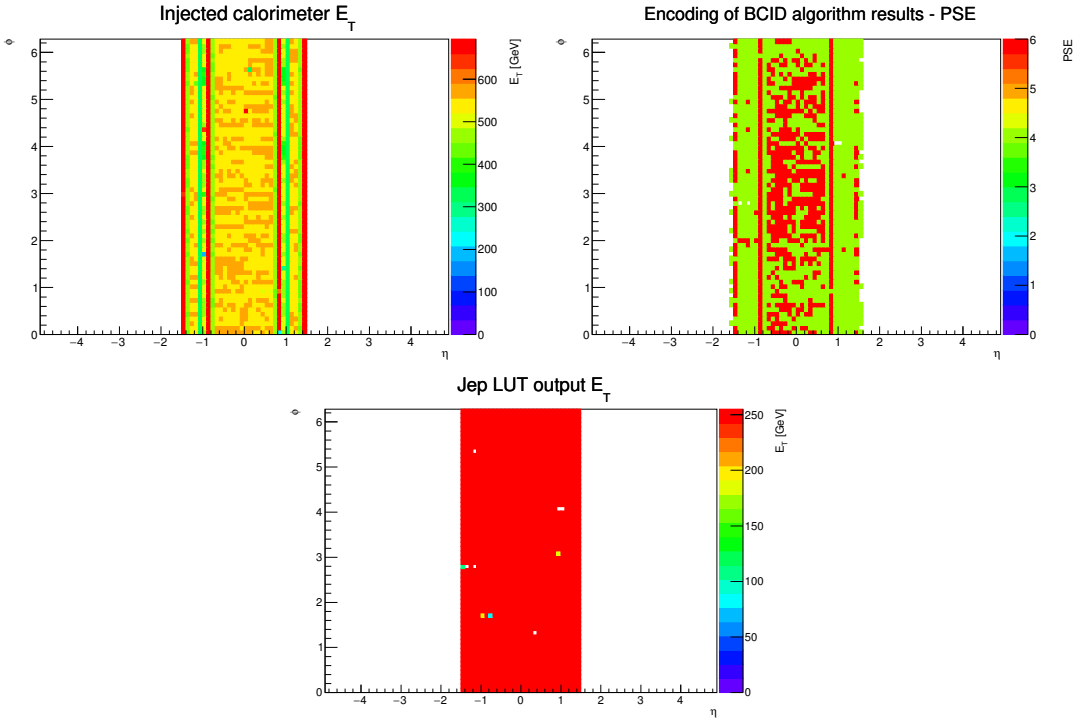

(a) Low energy step.

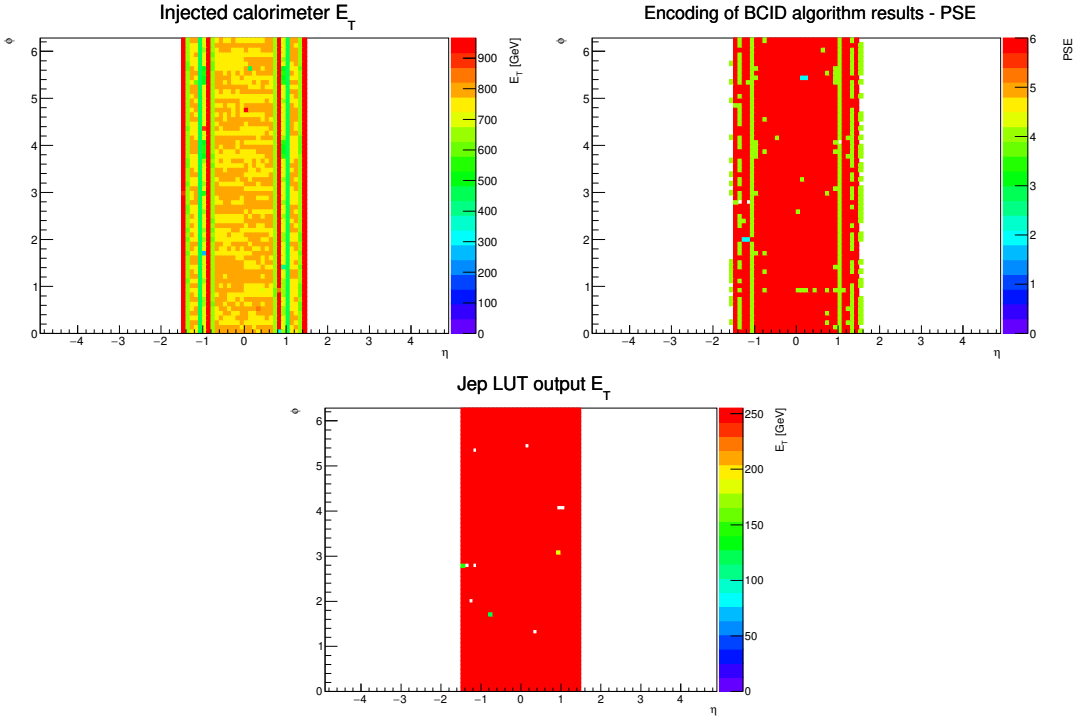

(b) High energy step.

Figure 7.9: Results of two pulser run steps in Tile with PF4 setting. For each step the E_T per tower (top left panel), the PSE plot (top right panel) and the LUT output per tower (bottom panel) is shown.

For both steps, no PeakFinder mistiming occurs in the pulser runs with the new decision logic enabled. This can be seen from the η-ϕ maps of the LUT output shown in the bottom panel, which are fully populated for both cases. The top left panel of Figure 7.9b shows that the highest energies pulsed for Tile in this study are below 1000 GeV. This was due to operational limitations. Since no pulser runs with higher energies were available and the validation of the new decision logic in LAr with PF4 was successful, the initial setting in the 2016 data taking for Tile was chosen to be PF4 as well.

However, already after the first run (299144, taken in spring 2016) with PF4 setting activated, several mistimed Tile events were discovered. One event as extracted from the raw data is examined shortly in the following. It contains a dijet, where one jet deposits enough energy to saturate a trigger tower. This tower causes an early trigger.

Figure 7.10 shows the energy deposition in the trigger towers of the hadronic calorimeter for the triggered BC (n). It contains one saturated tower at $\eta = -0.5$, $\phi = 5.6$ and otherwise low energetic background. Figure 7.11 shows the energy deposition one BC later ($n + 1$). It contains the rest of the dijet event. This situation, one saturated tower alone in the triggered BC and a real physics event one BC later, is a typical indication of PeakFinder mistiming.

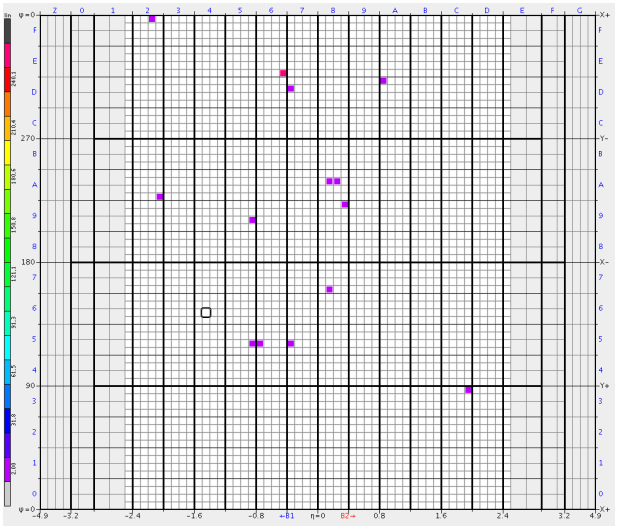

Figure 7.10: Energy deposition in the hadronic layer of the calorimeter for the triggered BC n of an early triggered event. One saturated tower is visible at $\eta = -0.5$, $\phi = 5.6$ and otherwise only low energy background is present.

Therefore it can be concluded that even with the new decision logic and the PF4 setting, PeakFinder mistiming still occurs for Tile. A possible solution is to use the PF3 setting and stop the PeakFinder already for three saturated samples.

This possibility was investigated in a second pulser run. The high energy step of this run with PF3 setting is shown in Figure 7.12. In the LUT output map shown in the left panel several towers have $LUT = 0$, even though the PeakFinder correctly identified the BC. This is seen in the PSE map shown in the right panel, where these towers have $PSE = 4$. A likely explanation is that the Sat40 mistriggered and the correct PeakFinder decision was ignored

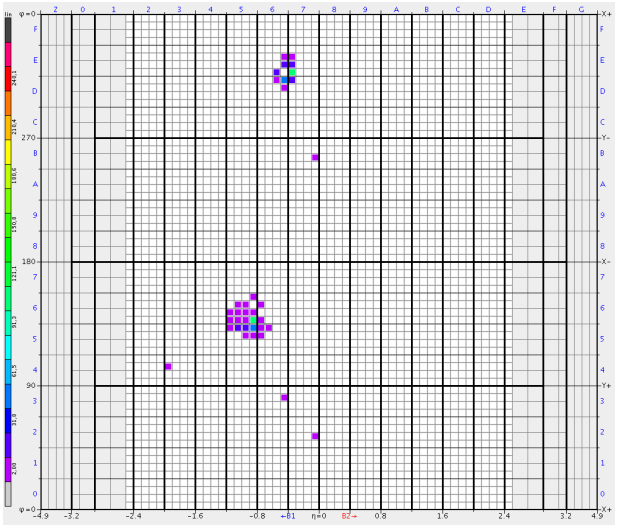

Figure 7.11: Energy deposition in the hadronic layer of the calorimeter for the BC $n+1$ of the event shown in Figure 7.10. The rest of dijet event is seen here with the saturated tower missing. This indicates that the saturated tower caused an early trigger.

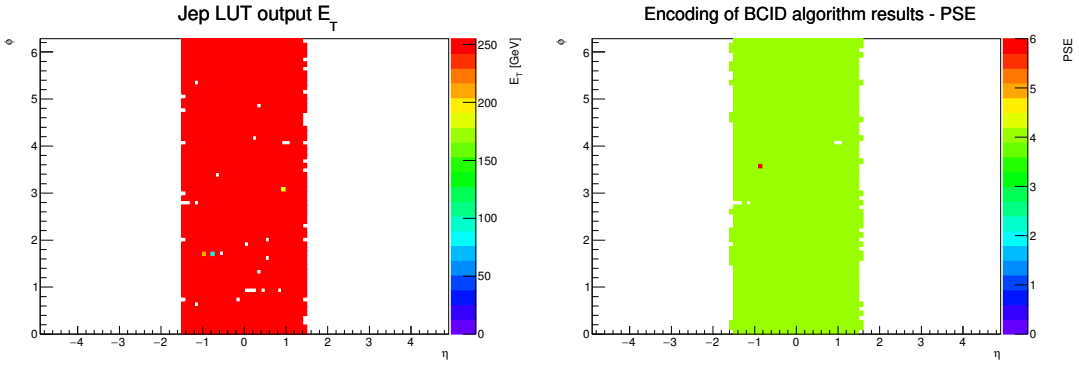

Figure 7.12: Results of the high energy step of a pulser run in the Tile calorimeter with PF3 activated. The η-ϕ maps show the LUT output per tower (left panel) and the PSE plot (right panel).

by the new decision logic since the pulses have three saturated samples. To confirm this, a raw event was extracted from the pulser data and an example pulse is displayed in Figure 7.13. Indeed, three samples are saturated and the PeakFinder is disabled. The Sat40 however triggers late, since it always decides for $s+1$ sample which in this case equals the $n+1$ sample.

In conclusion no setting of the new decision logic is found to be optimal for Tile. In PF4 mode, the PeakFinder mistiming causes early triggers. In PF3 mode, the Sat40 algorithm doesn't always work reliably, since the ADC_{n+2} sample saturates before the ADC_{n-1} sample, causing the Sat40 to trigger too late. However for data taking a decision for one of the settings has to be made.

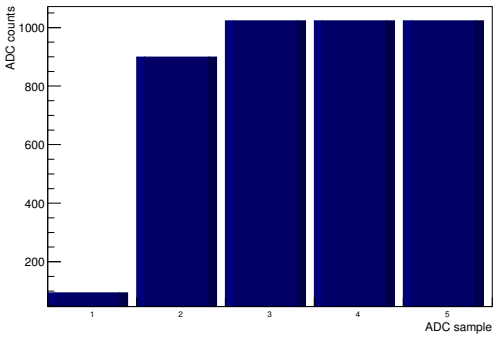

Figure 7.13: Pulse extracted from a tower missing a LUT ouput in the event shown in Figure 7.12. Three samples are saturated and the PeakFinder is disabled for the PF3 setting of the decision logic. The Sat40 triggers the pulse incorrectly, since it always fires on $s + 1$, which is in this case $n + 1$ and therefore one BC late.

Usually late triggers are considered less problematic than early ones. The reason is that even if some for towers in an event the BC is identified late, the whole event can still be triggered correctly, if only one tower with enough energy identifies the BC correctly. Since the hadronic jets detected with the Tile calorimeter spread over several trigger towers, there is a good chance that the correct BC is identified by a tower with sufficient energy and that the late triggers have no negative effect. In case of an early trigger however, parts of the event are always lost. Therefore the decision logic was set to PF3 for Tile during data taking to prevent early triggers at the risk of late ones. This shows that while the new decision logic can effectively prevent the PeakFinder mistiming, it can not stop all mistriggers. A possible solution is the introduction of the Sat80 algorithm described in the next chapter.

8 Commissioning of the Sat80 Algorithm and Pulse Shape Studies

In the last chapter it was shown that even with the new decision logic the combination of PeakFinder and Sat40 is not able to trigger all events correctly. These mistriggers could be prevented by the Sat80 algorithm, described in Section 4.2.1. Like the Sat40 algorithm, it is a threshold algorithm that operates on the leading edge of the pulse. However it uses samples digitized with 80 MHz instead of 40 MHz. This finer granularity allows it in principle to identify the correct BC in the whole saturated energy regime.

As part of this thesis, the Sat80 algorithm was studied using pulser runs. These efforts were part of the commissioning of the Sat80 and are described in the first part of this chapter. The studies showed that the Sat80 is sensitive to non-linearities of the pulse shape as a function of energy. Therefore the second part of the chapter is dedicated to pulse shape studies of physics pulses.

8.1 Validation of the Sat80 Algorithm

In this section the validation of the Sat80 with threshold derived from physics and from pulser run data is presented.

8.1.1 Threshold Derivation

The Sat80 is a threshold algorithm, based on a *low* and a *high* threshold. These thresholds have to be calibrated for the algorithm to operate correctly. The threshold derivation was done elsewhere [52]. However, to demonstrate the importance of the pulse shape on the derivation procedure, it is briefly outlined here. More details can be found in [53].

The decision the Sat80 has to make is whether the peak of the pulse is in ADC_s, ADC_{s+1} or ADC_{s+2}, where s is the first saturated sample. Therefore the values of the thresholds are determined from the pulse shape at different degrees of saturation. The following conditions can be derived, where n is the position of the peak:

$$ADC_{n-2.5}\left[E_{sat}\left(ADC_{n-2}\right)\right] < \textbf{low} < ADC_{n-1.5}\left[E_{sat}\left(ADC_{n}\right)\right] \tag{8.1}$$

and

$$\textbf{high} < min\left\{ADC_{n-1.5}\left[E_{sat}\left(ADC_{n-1}\right)\right] \quad ; \quad ADC_{n-1}\left[E_{sat}\left(ADC_{n}\right)\right]\right\}, \tag{8.2}$$

where $E_{sat}\left(ADC_{n-X}\right)$ is the saturation energy of ADC_{n-X}.

From Equation 8.1 and Equation 8.2 it can be seen that it is necessary to know the behavior of the 80 MHz samples $ADC_{n-1.5}$ and $ADC_{n-2.5}$ as a function of energy. Hence the thresholds cannot be determined from standard ATLAS physics data, which is only read out in $5+1$ mode with 40 MHz samples. Therefore dedicated physics runs are taken in $15+1$ mode with 80 MHz readout to produce data for the threshold derivation. Since in this enhanced readout mode the maximum readout rate is reduced, only a limited number of these runs was taken.

Consequently the statistics at high energies of the available data is not sufficient to determine the thresholds directly. The behavior of the ADC samples must be extrapolated to the energy

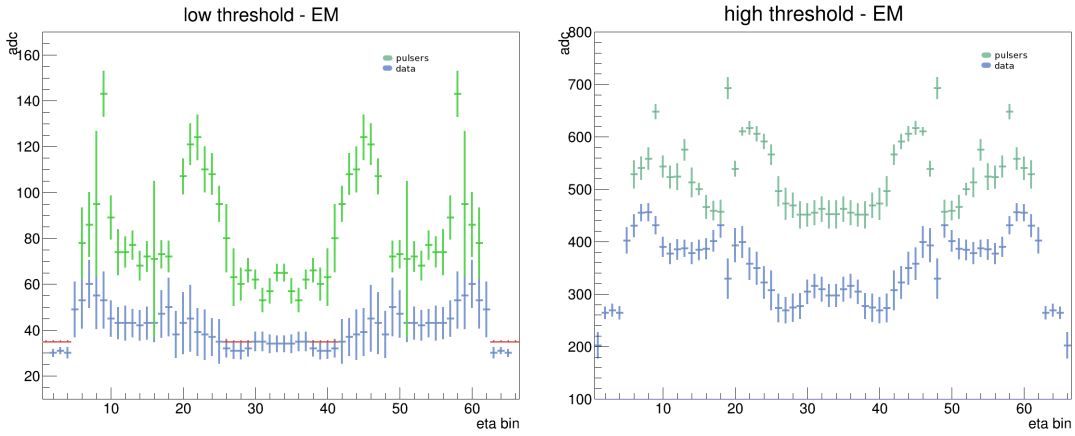

Figure 8.1: Values of the Sat80 thresholds shown in η bins for the electromagnetic calorimeter layer, with the low thresholds in the left panel and the $high$ thresholds in the right panel. Thresholds derived from physics data are shown in blue, thresholds derived from pulser runs are shown in green. Thresholds that have a value lower than the pedestal value of 32 are set to 35. They are shown in red [52].

region where the samples saturate. Since this behahvior is not precisely known a linear rise with energy is assumed.

The resulting thresholds derived from physics data are shown in Figure 8.1. The thresholds vary with η. This is caused by the different pulse shapes of the trigger tower signals in different calorimeter regions.

8.1.2 Validation with Thresholds Derived from Physics Data

For the validation of the Sat80, dedicated pulser runs were taken (see Section 7), where the algorithm was configured with the thresholds derived from physics data.

The L1Calo readout contains the result bit (R) of the Sat80 for each trigger tower. In pulser runs it indicates if the algorithm has identified the correct BC.

The results for a low energy step of a pulser run, with coefficients derived from physics data, are shown in Figure 8.2 for the electromagnetic calorimeter, the top left panel shows an η-ϕ map of the injected calorimeter E_T. The top right panel shows η-ϕ map of the Sat80 result bit and the bottom panel shows an η-ϕ map of the number of saturated 40 MHz ADC samples. It is visible that the algorithm does not perform as expected. In the region $1.2 < |\eta| < 1.4$ several towers are not triggered correctly by the Sat80, even though all towers in this region have at least two saturated ADC samples.

The results for a high energy step are shown in Figure 8.3, with the panels as before. The η-ϕ map of the Sat80 result bit (top right panel) shows that the algorithm does not identify the correct BC in large parts of EMB ($|\eta| < 1.4$). No correlation between the injected calorimeter E_T or the number of saturated samples and the regions of failure of the Sat80 can be seen.

Instead, the reason for this result is the difference in the pulse shapes between physics and calibration pulses especially in the high energy regime. Therefore Sat80 thresholds derived

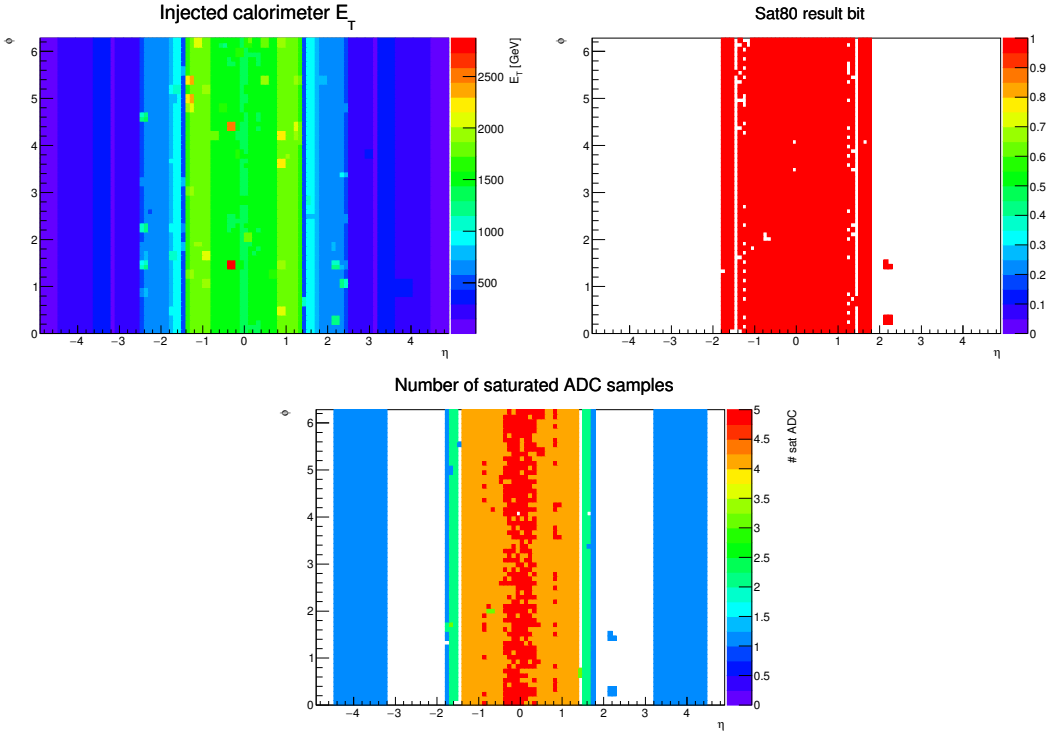

Figure 8.2: Results of the low energy step of a pulser run in the electromagnetic calorimeter. The Sat80 is configured with thresholds determined from physics data. The top left panel shows the E_T per tower, the top right panel the Sat80 result bit and the bottom panel shows the number of saturated 40 MHz ADC samples.

with physics data cannot be used in pulser runs.

8.1.3 Validation with Thresholds Derived from Calibration Data

To continue the validation, dedicated thresholds were derived for pulser runs. The derivation was based on data from a low energy pulser run with $E_T < 400\,\text{GeV}$ [52]. For comparability the same method as for physics data was used, especially the linear extrapolation of the ADC samples to higher energies.

The resulting thresholds are also shown in Figure 8.1 together with the thresholds from physics data. There is a large difference between the two sets over the whole η range for both the low and the high threshold. This confirms that the failure of the Sat80 with physics thresholds in pulser runs is caused by the pulse shape differences between calibration and physics pulses.

A new pulser run was taken, with the Sat80 algorithm configured with the dedicated thresholds for pulser runs. The results for a low and a high energy step of this pulser run in the electromagnetic calorimeter are shown in Figure 8.4. The left panels show the injected calorimeter E_T and the right panels show the Sat80 result bit. As before, the performance of the Sat80

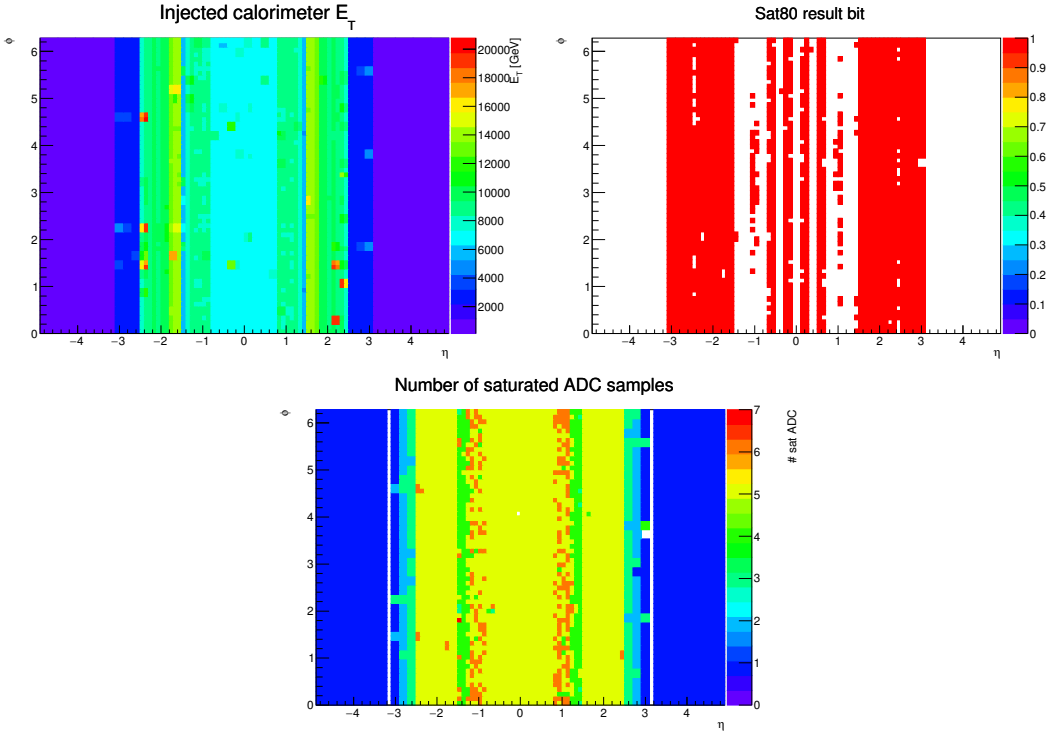

Figure 8.3: Results of the high energy step of a pulser run in the electromagnetic calorimeter. The Sat80 is configured with thresholds determined from physics data. The top left panel shows the E_T per tower, the top right panel the Sat80 result bit and the bottom panel shows the number of saturated 40 MHz ADC samples.

degrades with energy. In the low energy step the Sat80 misidentifies the BC only for a few towers. These towers are mostly in the region $0.8 < |\eta| < 1.4$, where the calorimeter E_T is higher than 1200 GeV. Indeed, in the steps with lower E_T, not shown here, the Sat80 identifies the BC correctly in the whole EMB. The high energy step however exhibits misidentification in large parts of the EMB and the EMEC inner wheel.

These misidentifications are not expected with the dedicated thresholds for pulser runs and further investigation is needed. The pulse from the trigger tower with coordinates $\eta = 0.65$ and $\phi = 0.25$ from the high energy step shown in Figure 8.4 is examined in the following. The Sat80 misidentified the BC for this tower. The pulse is shown in Figure 8.5. It has 15 ADC samples digitized with 80 MHz. The 40 MHz samples, the first saturated sample s and the correct BC n are designated. In pulser runs the correct BC is always the central sample of the pulse, as the trigger is given by the LAr electronics.

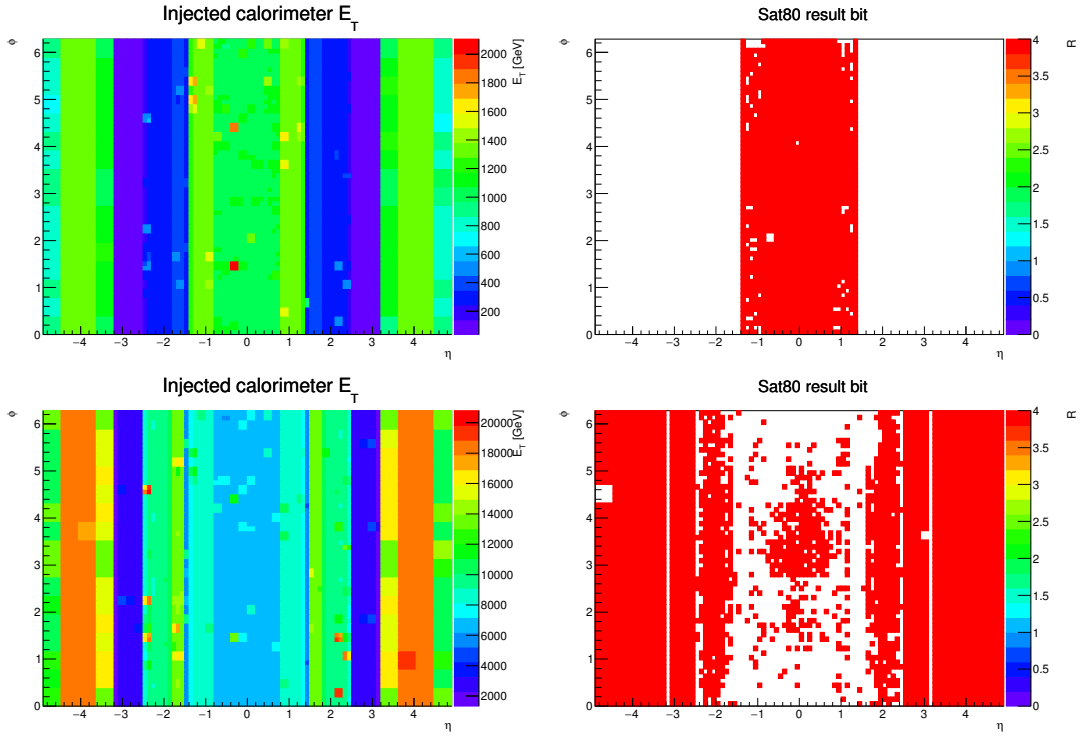

Figure 8.4: Results of a pulser run in the electromagnetic calorimeter. The Sat80 is configured with thresholds determined from pulser run data. The top panel shows a low energy step and the bottom panel shows a high energy step. The left hand plots contain the calorimeter E_T and the right hand plots show the Sat80 result bit.

The pulse shown in Figure 8.5 has the first saturated 40 MHz sample s is in ADC_{n-1}. Therefore this pulse should be triggered as $s+1$ by the Sat80. The thresholds for this tower are $low = 55$ and $high = 430$ (c.f.Figure 8.1). With knowledge of the thresholds, the ADC samples and Equation 4.10, the Sat80 decision can be calculated

$$ADC_{s-1} = 848 > 472 = high \tag{8.3}$$
$$ADC_{s-1.5} = 270 > 174 = low \tag{8.4}$$

$$\Rightarrow \quad \text{BC} = s = n-1.$$

Consequently the Sat80 identifies the BC as $n-1$, which is one BC too early. This implies that the dedicated thresholds are not correct for this highly saturated pulse.

To understand this, the behavior of the pulse shape in pulser runs was studied. The ADC samples that are important for the threshold derivation are shown in Figure 8.6 for the trigger tower that contains the misidentified pulse. The central sample ADC_n displayed in panel a) and the sample ADC_{n-1} shown in panel b) rise linearly until saturation. This is the expected

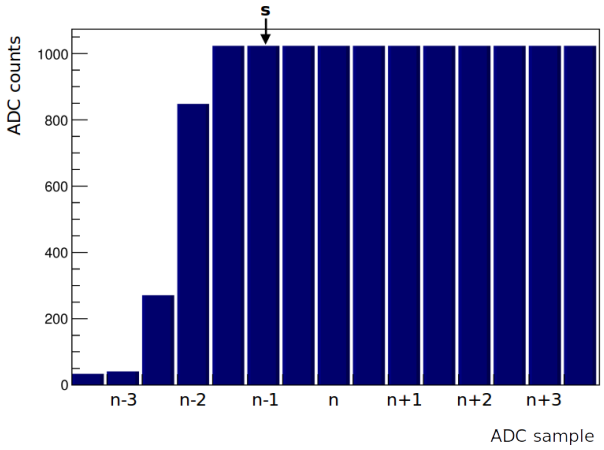

Figure 8.5: Pulse from a mis-triggered trigger tower ($\eta = 0.65, \phi = 0.25$) in a pulser run with the Sat80 active with thresholds optimized for pulser pulses.

behavior. In contrast the samples shown in panel c)-e), corresponding to $ADC_{n-1.5}$, ADC_{n-2} and $ADC_{n-2.5}$ exhibit an increasing non-linearity.

This non-linearity is in contrast to the original assumption of a linear rise of the ADC samples with energy, made for the threshold derivation. It is the reason why the Sat80 performs well for energies below 1200 GeV, where the ADC samples still rise linearly with energy, but fails for higher energies where the non-linear behavior starts to dominate. This has important consequences on the threshold derivation, discussed in the next section.

8.1.4 Threshold Derivation for Non-linear Pulse Shapes

It is possible to derive new thresholds that take the non-linearities into account. This is done by performing piecewise-linear fits shown in Figure 8.6. The fit results are given in Table 8.1.

ADC Sample	Fit range [GeV]	Slope $\left[\frac{\text{ADC counts}}{\text{GeV}}\right]$	Offset [ADC counts]
ADC_n	2500 to 7000	3.00	47.2
ADC_{n-1}	0 to 480	2.10	43.0
$ADC_{n-1.5}$	0 to 700	1.27	−32.9
ADC_{n-2}	0 to 1500	0.38	20.67
ADC_{n-2}	2500 to 7000	0.03	677.8
$ADC_{n-2.5}$	2500 to 7000	0.03	88.1

Table 8.1: Fit results from the piece-wise linear fits shown in Figure 8.6.

The $high$ threshold is determined by Equation 8.2. The saturation energies of ADC_n and ADC_{n-1} taken from the respective linear fits are $E_{Sat}\,(n) = 324.3$ GeV and $E_{Sat}\,(n-1) = 465.2$ GeV. The corresponding ADC values that give the upper bound for the $high$ threshold are $ADC_{n-1}\,(E_{Sat}\,(n)) = 724$ and $ADC_{n-1.5}\,(E_{Sat}\,(n-1)) = 557$. In the latter case a

linear fit is used, since $E_{Sat}\,(n-1)$ is still in the linear regime. From the bounds the threshold is chosen as $high = 555$, with a safety margin of 2 ADC counts to take fluctuations due to e.g. noise into account. The original threshold ($high = 472$) is compatible with this result, as it is lower than both upper bounds. The reason why it is lower by more than 70 ADC counts is that it was determined such that the upper bounds of all trigger towers with $\eta = 0.65$ are fulfilled. This agreement is expected, since from the ADC samples used to determine the high threshold only ADC_{n-1} shows a minimal non-linearity.

The low threshold is determined by Equation 8.1. The saturation energy for ADC_n is determined as before. For ADC_{n-2} this is more complicated. From Figure 8.6d is clear that the sample does not saturate even for the highest expected energy during Run 2 $E_T = 7000\,\text{GeV}$. To still be able to derive thresholds, the saturation energy is defined as $E_{Sat}\,(n-2) = 7000\,\text{GeV}$. It follows that $ADC_{n-1.5}\,(E_{Sat}\,(n)) = 379$ and $ADC_{n-2.5}\,(E_{Sat}\,(n-2)) = 284$, where the latter has been determined with a linear fit above 2500 GeV. Since the low threshold must be between these two bounds, it is chosen as the arithmetic mean $low = 332$. It is considerably larger than the original threshold $low = 174$, due to the non-linearity of ADC_{n-2}.

With these new thresholds that take into account the non-linear pulse shape the pulse in Figure 8.5 can be reexamined. The calculation of the Sat80 decision now yields

$$ADC_{s-1} = 848 > 555 = high \tag{8.5}$$
$$ADC_{s-1.5} = 270 < 332 = low \tag{8.6}$$

$$\Rightarrow \quad \text{BC} = s + 1 = n.$$

This shows that the new thresholds give the correct Sat80 decision for this tower even for very high energies. It was verified that the Sat80 works correctly with the new thresholds also for lower energies. This study demonstrates that it is possible to derive thresholds such that the Sat80 works even in the case of non-linear pulse shapes.

8.2 Pulse Shape Studies in Data

In the previous section it was shown that the thresholds of the Sat80 algorithm are sensitive to non-linearities of the pulse shape in pulser runs. These non-linearities can have two main reasons. Firstly, the pulse injected by the calibration system could become non-linear for very high charges, when the system reaches its limit. Secondly, the analog input chain (c.f. Section 3.2.3) from LAr to L1Calo could introduce the non-linearities. Also a combination of both is possible.

If the non-linearities are caused by the analog input chain, they are expected to appear also in physics pulses. Due to possible consequences on the Sat80 it is necessary to study the linearity of the pulse shape in physics data. For this purpose the electron and photon selection and the matching to trigger towers developed for the studies described in Section 6 are used.

The statistics available from the 2016 ATLAS dataset are sufficient to study the pulse shapes on trigger tower level. The behavior of the five 40 MHz ADC samples around the peak is shown in Figure 8.7 for the trigger tower with coordinates ($\eta = 0.9$,$\phi = 2.7$). Similar to the pulses in

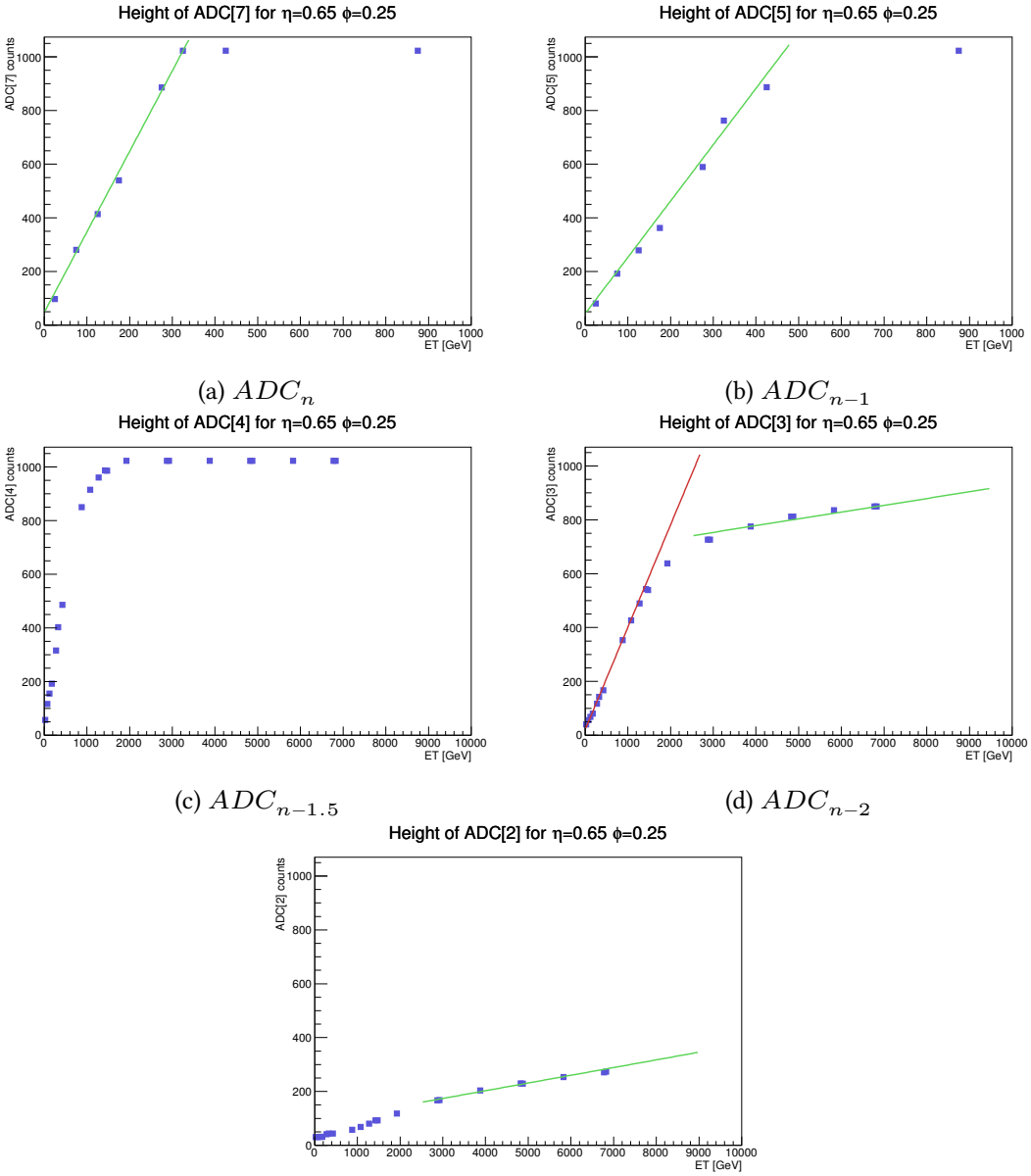

(a) ADC_n

(b) ADC_{n-1}

(c) $ADC_{n-1.5}$

(d) ADC_{n-2}

(e) $ADC_{n-2.5}$

Figure 8.6: Height of the ADC samples, which are important for the Sat80 threshold derivation, as a function of E_T. The pulses are taken from a trigger tower in the electromagnetic calorimeter with coordinates $\eta = 0.65$ and $\phi = 0.25$.

pulser runs, the central sample ADC_n behaves linearly until it saturates. The same is true for the samples in the falling edge of the pulse ADC_{n+1} and ADC_{n+2}.

The sample before the peak ADC_{n-1} behaves mostly linear, but shows a slight non-linearity before reaching saturation. As discussed before in Section 6.3.7, the sample ADC_{n-2} has too

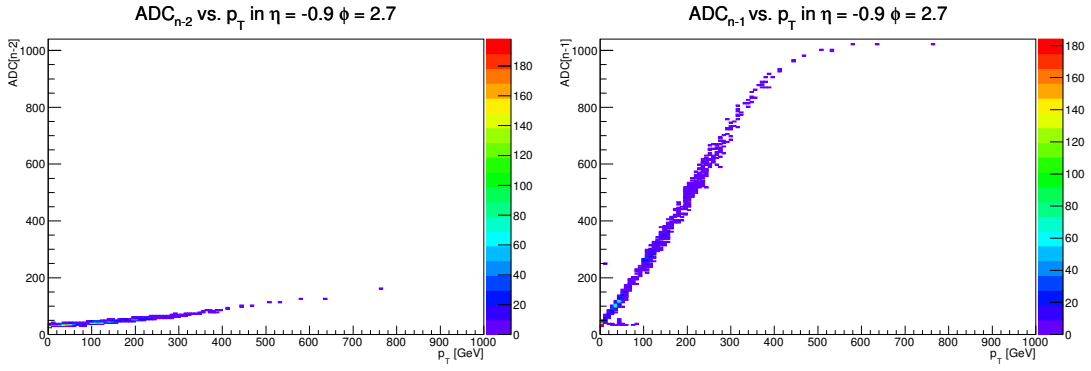

(a) ADC_{n-2}

(b) ADC_{n-1}

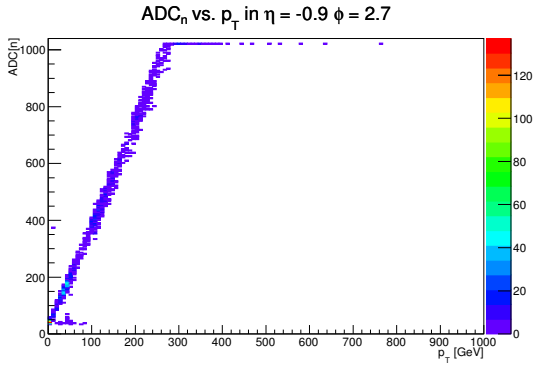

(c) ADC_n

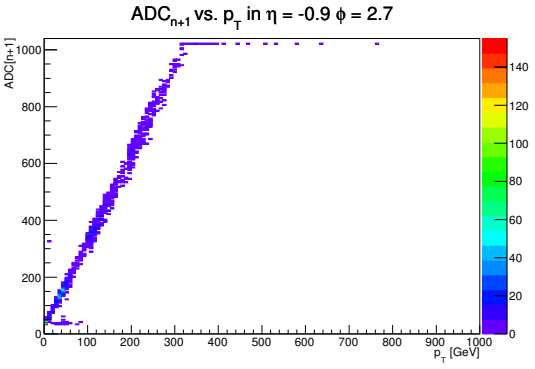

(d) ADC_{n+1}

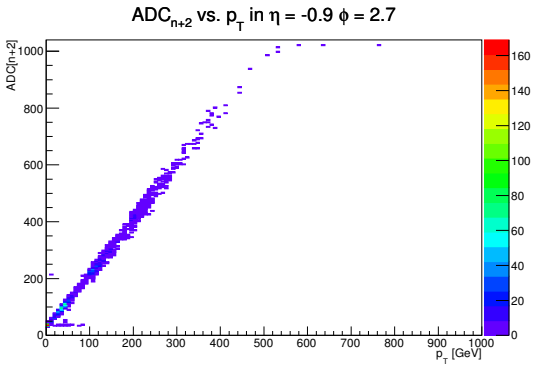

(e) ADC_{n+2}

Figure 8.7: Height of the ADC samples as a function of p_T for LAr pulses in physics data.

low statistics at higher energies to make a definitive statement about its linearity.

To parametrize the behavior of the ADC samples with energy, several fits have been performed. For ADC_n, ADC_{n+1} and ADC_{n+2} a linear function of the form

$$ADC_{n+x}\left(p_T\right) = m_x p_T + c_x \qquad x \in \{0, 1, 2\} \tag{8.7}$$

is used. It was found that a generalized logistic function given by

$$ADC_{n-2}\left(p_T\right) = A + \frac{K - A}{C + Qe^{-B(p_T - p_0)}}, \tag{8.8}$$

can account for the non-linearity in ADC_{n-1}. This function describes very well the non-linearity before saturation, while the linear part is not perfectly described. However, for the saturation studies done here a description of the linear part is not so important. The results of the fitting procedure are shown in Figure 8.8 for all trigger towers in $\eta = -0.9$ combined.

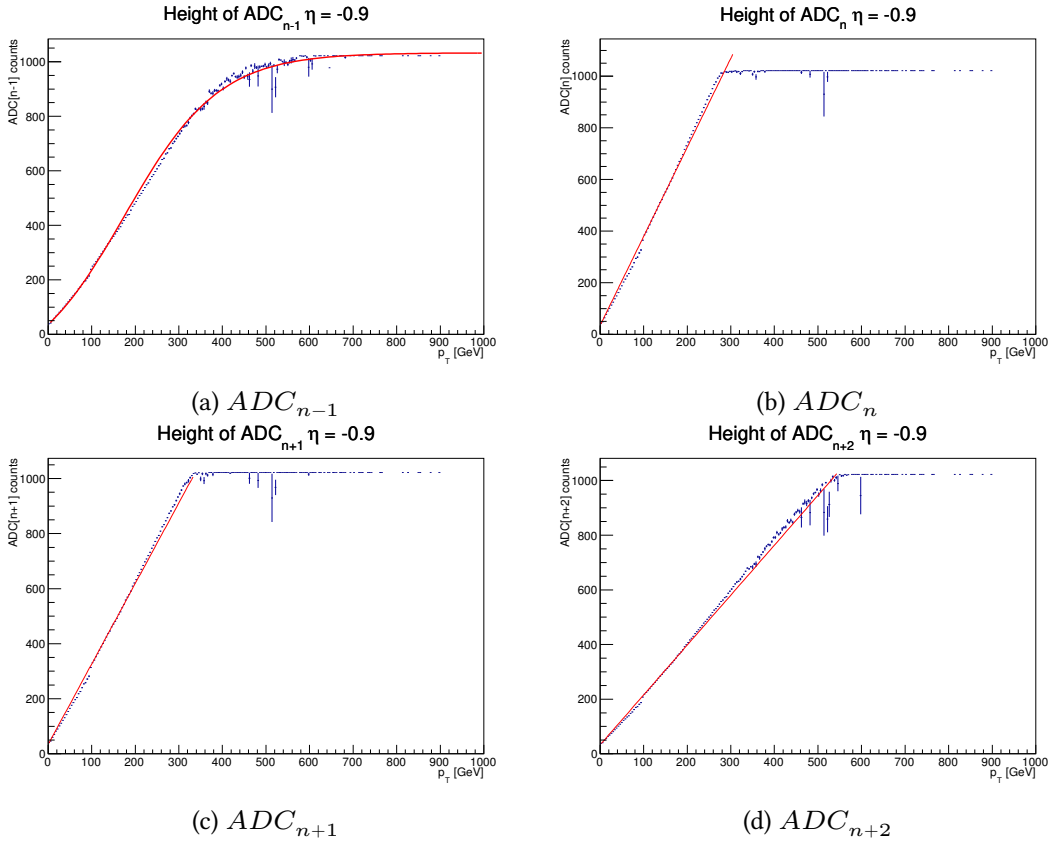

(a) ADC_{n-1} (b) ADC_n

(c) ADC_{n+1} (d) ADC_{n+2}

Figure 8.8: Height of the ADC samples as a function of p_T for physics pulses in the electromagnetic calorimeter. All trigger towers in $\eta = -0.9$ are combined. Linear fits are performed for ADC_n, ADC_{n+1} and ADC_{n+2} and a generalized logistic fit is performed for ADC_{n-1}. ADC_{n-2} is not fitted, since the statistics at high p_T are too low to choose a sensible fit function.

The knowledge of the functional behavior of the ADC samples is very useful. One possible use case are comparative studies of the pulse shapes in physics data and pulser runs. This would be especially interesting, since studies using pulser runs are often limited by the pulse shape differences to physics data. The functional behavior determined here can be used to define transfer functions between the different pulses.

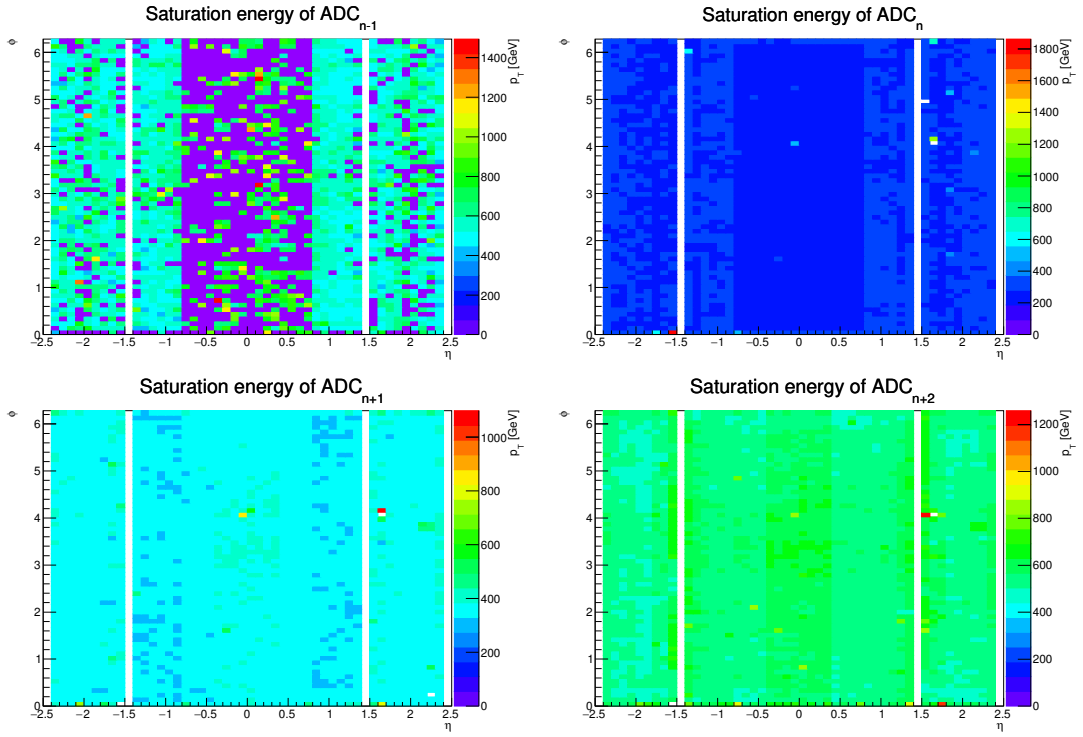

Figure 8.9: Saturation energy for different ADC samples in the electromagnetic layer of the calorimeter. For ADC_{n-1} not all towers contain enough statistics to achieve a conversion of the fit.

Another use case, presented here, is the determination of the saturation energies for or the samples ADC_{n-1}, ADC_n, ADC_{n+1} and ADC_{n+2} on trigger tower level. The results are shown in Figure 8.9. To improve the convergence of the generalized logistic fit to the ADC_{n-1} sample, it is performed first in bins of η. The resulting fit parameters are used to initialized the fit parameters on trigger tower level. This strategy is works well, since the pulse shapes for trigger towers in the same η region are similar. The saturation energies can be employed to determine how many ADC samples are saturated for a given energy in a given trigger tower.

The study of saturated pulses in physics data presented here shows a non-linearity in the ADC_{n-1} sample. The ionization pulse in the calorimeter is not expected to show non-linear behavior, therefore the non-linearities are likely caused in the analog input chain from LAr to L1Calo. A possible reason are saturation effects in the analog components that are known to occur for high energetic pulses [30].

With the current dataset it is not possible to further study the influence of the non-linearities on the Sat80 algorithm. This has two reasons. Firstly the statistics at higher p_T are too low. This is especially problematic for the ADC_{n-2} sample where the complete behavior up to saturation energies is not known. Secondly in standard ATLAS data taking, the 80 MHz samples are not read out.

8.3 Pulse Shape Studies in Simulation

Simulations are a possibility to overcome the limitations of pulse shape studies in data. However it is important to understand if a given simulation reproduces the real system accurately enough. A simulation should take into account all steps of the analogue input chain from the triangular output pulse of the calorimeter to the receiver system of L1Calo (c.f. Section 3.2.3).

A simplified way to describe the effect of the analogue input chain on the initial calorimeter signal is the use of transfer functions in Laplace space that model the different components in the chain [30]. For a time dependent, continuous input signal $i_{phys}(t)$ and output signal $o_{phys}(t)$ of a component X, with Laplace transforms

$$I(s) = \int_{-\infty}^{\infty} i_{phys}(t)\, e^{-st} dt, \quad s \in \mathbb{C} \tag{8.9}$$

$$O(s) = \int_{-\infty}^{\infty} o_{phys}(t)\, e^{-st} dt, \quad s \in \mathbb{C} \tag{8.10}$$

the transfer function $H(s)$ is defined as

$$H_X(s) = \frac{O(s)}{I(s)}. \tag{8.11}$$

So to model the component X, the input signal is transformed into Laplace space and multiplied by the transfer function. The desired output signal is the inverse Laplace transform of the product given by

$$o_{phys}(t) = \int_{-\infty}^{\infty} H_X(s)\, I(s)\, e^{st} ds. \tag{8.12}$$

The triangular output pulse of the LAr calorimeter is shown in Figure 3.5. The Laplace transform of a pulse with energy E_0 is given by

$$I_{LAr}(s) = E_0 \left(\frac{1}{s} - \frac{1 - e^{-st_{dr}}}{t_{dr} s^2} \right), \tag{8.13}$$

where t_{dr} is the drift time of the charges and the decay time of the triangular pulse. Typically the drift time is $t_{dr} = 450$ ns for LAr (cf. Figure 3.5).

For this simplified simulation four transfer functions are used, one each for the preamplifier (H_{pamp}), the shaper (H_{shape}), the tower builder board (H_{tbb}) and the receiver (H_{rec}). The functions are given by

$$H_{pamp}(s) = \frac{R_f}{1 + C_f R_f s} \tag{8.14}$$

$$H_{shape}(s) = \frac{\tau_{sh} s}{(1 + \tau_{sh} s)^3} \tag{8.15}$$

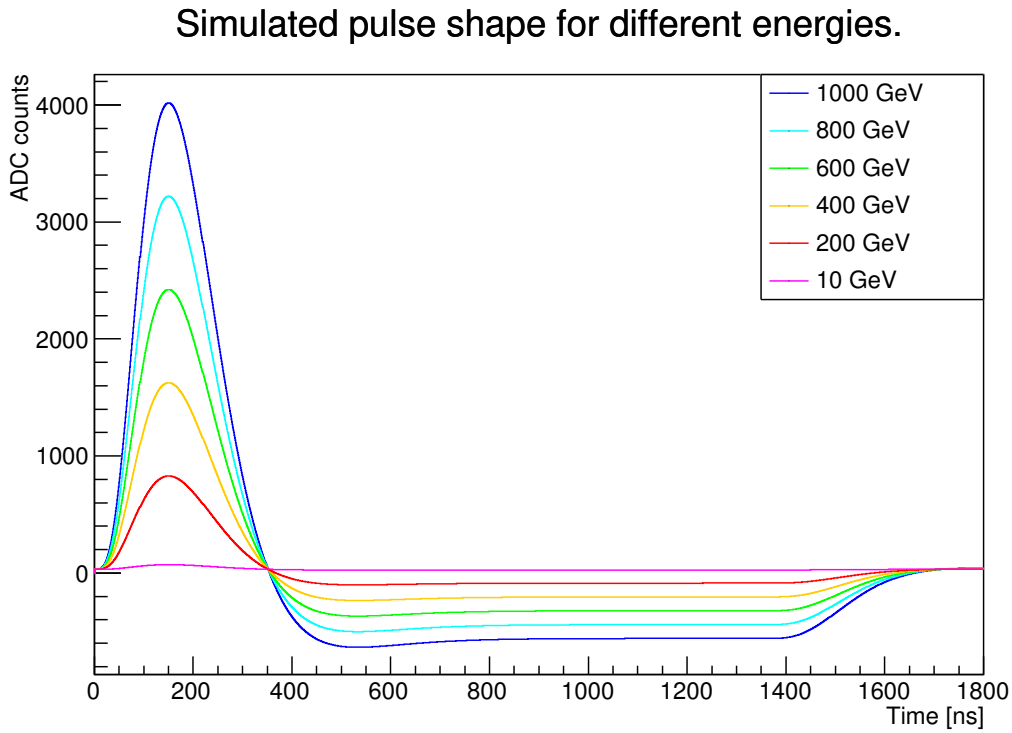

Figure 8.10: Simulated LAr pulse shape in the trigger towers for different energies.

$$H_{tbb}(s) = \frac{1+\tau_{tbb,1}s}{1+\tau_{tbb,2}s} \tag{8.16}$$

$$H_{rec}(s) = \frac{1}{1+\tau_{rec}s} \tag{8.17}$$

and the final transfer function is given by

$$H(s) = G_{sh}G_{lsb}G_{rec}H_{pamp}(s)\,H_{shape}(s)\,H_{tbb}(s)\,H_{rec}(s)\,. \tag{8.18}$$

The constant factors depend on the hardware and are shown in Table 8.2. The final transfer function can be used to calculate the height of the pulse for a given energy E_0 after the receiver for a given time t, with the rise of the triangular pulse starting at $t = 0$.

Figure 8.10 shows several simulated pulses of different energies. The conversion from E_T to ADC counts is done as described in Section 4.2, with one ADC count corresponding to 0.25 GeV. Comparing the pulse shape with Figure 3.5 shows that the general shape of the pulse is well reproduced.

In the next step, the pulses are digitized. The rise time of the pulses is fixed in the simulation and the peak is reached after 50 ns. Therefore the pulse can be digitized at fixed times. Five samples are taken, one each at 0 ns, 25 ns, 50 ns, 75 ns and 100 ns.

An example for the digitization is shown in Figure 8.11. The first five samples correspond to the typical L1Calo readout. The sample height is limited to 1023, which corresponds to

Constant	Value
R_f	880 Ω
C_f	2.4 pF
τ_{sh}	16 ns
$\tau_{tbb,1}$	40 ns
$\tau_{tbb,2}$	25 ns
τ_{rec}	5 ns
G_{sh}	9.8
G_{lsb}	1.02
G_{rec}	1.75

Table 8.2: Constant factors used in analytical pulse shape simulation, taken from [30, 54].

digital saturation. The behaviour of the ADC samples with energy is shown in Figure 8.12. For these plots several thousand pulses of different energies are simulated and digitized. The sample ADC_{n-2} does not rise with energy in the simulation, since the simulated pulse is injected exactly at the same time as the digitization for this sample happens. At this point the pulse height remains zero for all energies. For the remaining ADC samples the sample height increases perfectly linear with energy.

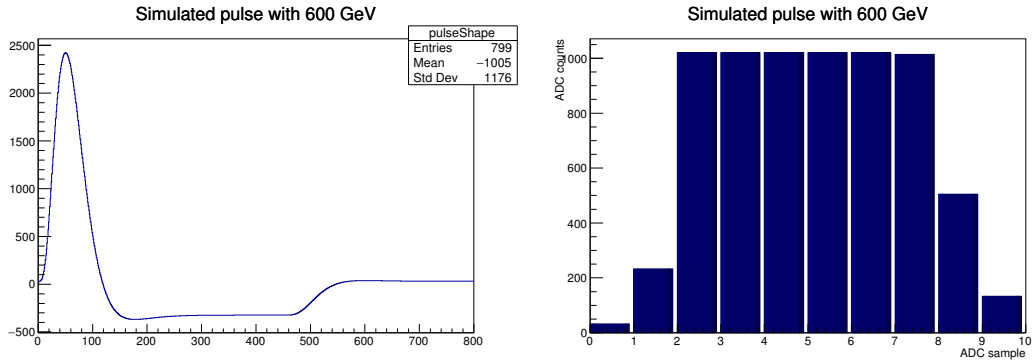

Figure 8.11: Example of the digitization of a highly saturated LAr trigger tower pulse. The first five ADC samples would be read out by L1Calo.

This can be understood by considering Equation 8.13. The energy is a multiplicative factor independent of s. It follows that for an energy mE_0, the shape of the output pulse is given by $mo_{phys}(t)$, where $o_{phys}(t)$ is the pulse corresponding to the energy E_0.

This shows that the analytical simulation cannot be used to reproduce the non-linearity found in data and that further studies are necessary. One possibility is the use of a SPICE simulation [55] of the analog input chain that was provided by LAr community. It takes saturation effects in the electronics into account.

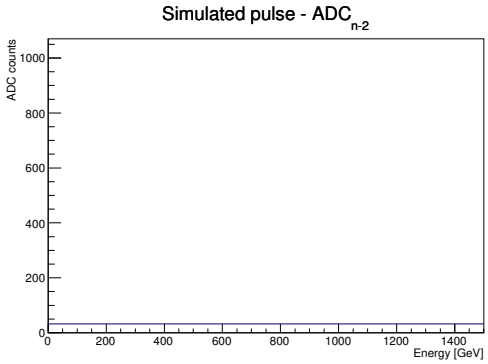

(a) ADC_{n-2}

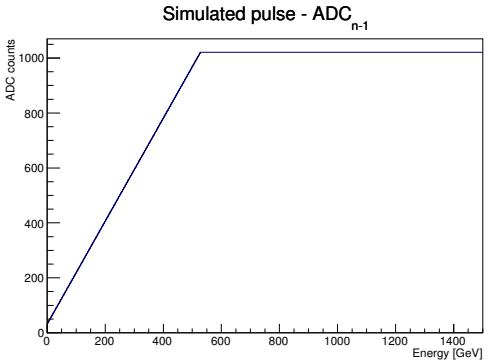

(b) ADC_{n-1}

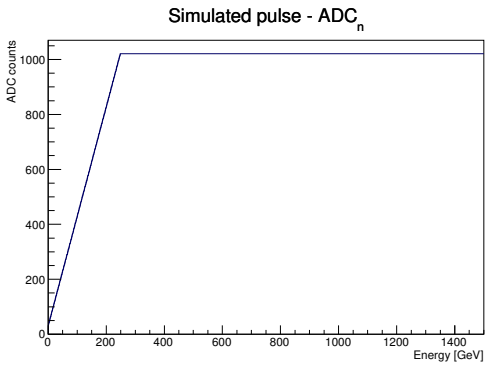

(c) ADC_{n}

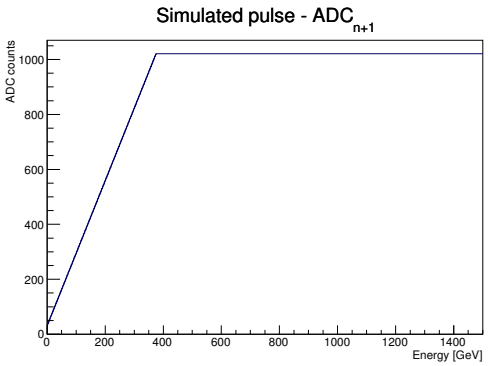

(d) ADC_{n+1}

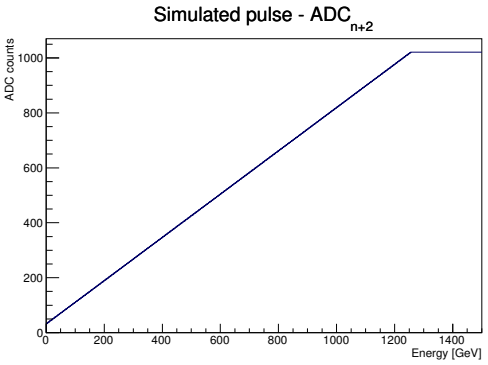

(e) ADC_{n+2}

Figure 8.12: Height of the ADC samples as a function of E_T for LAr pulses from the analytical simulation.

9 Monitoring

A part of the work for this thesis was done at CERN. During this time daily operations of L1Calo played an important role. One tool used in operations is the ATLAS monitoring, a large set of histograms that report on the status of the various ATLAS subsystems. These histograms are automatically produced and filled from the ATLAS data streams.

Since the reconstruction of the large data sets recorded by ATLAS in the main physics stream can take several days, a special stream is available for monitoring purposes. This "express stream" contains a subset of the recorded events and is usually streamed at 20 Hz. The events in the express stream are reconstructed in "quasi-realtime" and the histograms are accessible via a web interface. They help to detect and diagnose problems in a still ongoing run and allow an assessment of the data quality. [56].

The analysis code used to produce the histograms must be provided by each subsystem. For L1Calo and specifically the PPM the monitoring is close to the hardware, to control the correct function of readout and algorithms. Some of this monitoring code was written or modified as part of this thesis. New histograms for the Sat80 monitoring were added and bugs in the existing PPM monitoring simulation were fixed. The latter requires a deep understanding of the simulation code, as well as the hardware, since problems that show up in the monitoring histograms need to be investigated quickly and thoroughly to decide whether the error is real and needs intervention or if it is caused by a bug in the software. The results are described in this chapter.

9.1 Monitoring the Sat80 Algorithm

The L1Calo readout contains information about which algorithms identified the triggered BC. This is explained in Section 4.2.3 and used in the previous chapters. The information is stored in a 3 bit word called the "PSE bits". For the comissioning of the Sat80 algorithm the PSE bits were changed to "PSR bits", where the decision result bit of the external BCID (E) algorithm was replaced by the decision result bit of the Sat80 (R). To account for these changes the monitoring histogram shown in Figure 9.1 was modified to include the Sat80 result bit.

The PSR bits are decoded and the event is categorized depending on the algorithms that fired. Several categories are used, including only Sat40 or Sat80 (satBC), only the PeakFinder (peakF), satBC & peakF, the Sat80 alone or in conjuction with Sat40/PeakFinder (sat80BC) and only the Sat80. The y-axis of Figure 9.1 shows to the height of the central ADC sample (ADC_n).

A direct simulation of the Sat80 decision is not possible in standard ATLAS data taking, since it requires the readout of the 80 MHz samples that is not available. However the firmware encodes some information about the Sat80 decision in a 3 bit word that can be used in certain cases to verify the readout of the Sat80 decision. This word contains the information whether the $ADC_{n-1.5}$ and $ADC_{n-2.5}$ passed the low or $high$ threshold. The encoding scheme of the different cases in the firmware is shown in Figure 9.2.

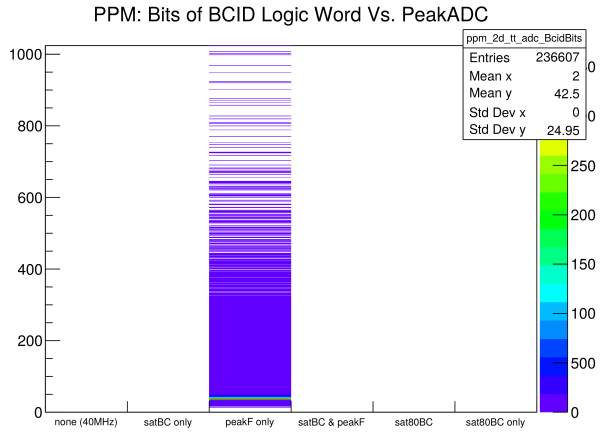

Figure 9.1: Decoding of the PSR bits in the ATLAS monitoring. The histogram shows the decisions taken by the BCID algorithms alone or in combination with each other. The y-axis shows the height of the central sample (ADC_n).

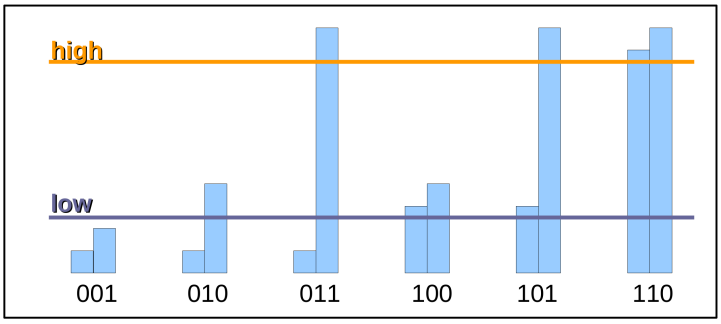

Figure 9.2: Encoding of the height of $ADC_{n-2.5}$ (left) and $ADC_{n-1.5}$ (right) relative to the *low* and *high* threshold [57].

Since only 3 bit are available, the number of cases that can be encoded is limited to eight. Therefore they are chosen such that $ADC_{n-2.5} < ADC_{n-1.5}$. This is motivated by the typical pulse shape in the trigger towers. All other cases, where $ADC_{n-2.5} > ADC_{n-1.5}$, cause the bits to be set to 111. In case that there is no saturated ADC, the bits are set to 000. In the monitoring these bits are decoded as shown in Figure 9.3, which was produced using a physics run in the 2016 data taking with proton-proton collisions. The information provided by the bits can be used to partially recalculate the Sat80 decision and to monitor the corect behavior of the algorithm.

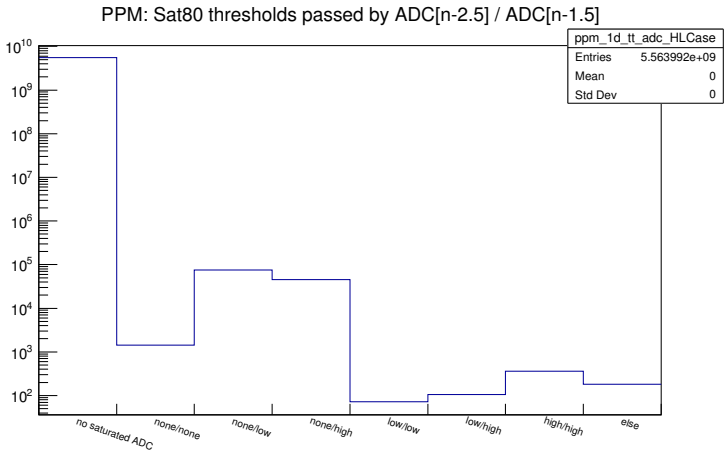

Figure 9.3: Decoding of the bits that contain information about the position of $ADC_{n-2.5}$ and $ADC_{n-1.5}$ relative to the Sat80 thresholds in the monitoring.

9.2 PPM Simulation Errors

As part of the L1Calo monitoring, all processing steps on the PPM (c.f. Section 4.2) are simulated as complete as possible for each trigger tower in each event after the raw data is recorded. Starting from the ADC samples this simulation includes pedestal subtraction, FIR filters, BCID algorithms and LUT E_T calculation. Information that can not be reproduced in the simulation, like the value of the dynamic pedestal correction, is taken from the readout. The conditions database that contains the L1Calo configuration for each run is also used during the simulation to access information like the LUT slope or the noise cuts.

The simulation compares its results with the results found by the hardware for the same input. A "simulation error" occurs when these results do not agree. The comparison is done for the LUT output and the BCID decision. In the course of the work for this thesis several different simulation errors happened during data taking and were debugged. A selection is presented in this section.

9.2.1 $7+1$-readout

As explained in Section 4.2.3 the normal readout mode in physics data taking is $5+1$. There are however some special runs that use an extended readout mode. During run 310 574 the $7+1$ readout mode was active. This run showed a large number of CP LUT mismatches. Figure 9.4 shows an η-ϕ map of mismatches per trigger tower, where the hardware produced a non-zero LUT value and the simulation expected zero. Ideally this histogram should be empty.

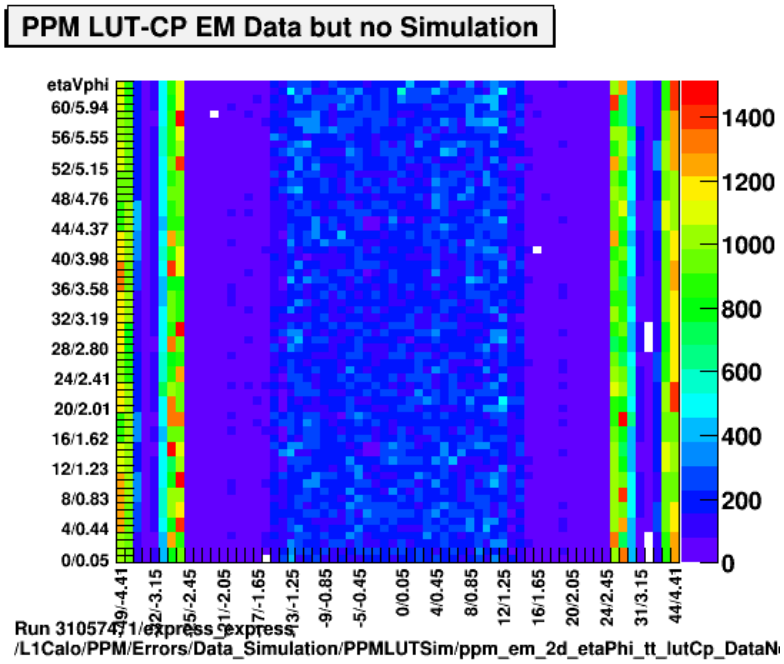

Figure 9.4: η-ϕ map of the electromagnetic layer showing the number of "LUT-CP data but no simulation" errors per trigger tower.

During the same run also errors of the opposite kind occured, where the simulation expects a non-zero LUT value, but finds zero in the readout. This is shown in Figure 9.5.

These errors did not appear in previous or subsequent runs that used $5 + 1$ readout mode and were indeed found to be related to the $7 + 1$ readout mode.

As stated in Section 4.2.1 the PeakFinder needs seven ADC samples to take a decision. It calculates three sums S_{n-1}, S_n and S_{n+1} and subtracts the pedestal correction values ped_{n-1}, ped_n and ped_{n+1}. The corrected sums are then put in a PeakFinder algorithm to see if the central sum is a local maximum

$$S_{n+1} - ped_{n+1} \leq S_n - ped_n > S_{n-1} - ped_{n-1}. \tag{9.1}$$

If the condition is fulfilled, n is identified as the BC.

The simulation errors occurred because the simulation was configured to simulate the PeakFinder decision in $7 + 1$ readout mode. However the readout of the pedestal correction is tied to the readout of the LUT value (c.f. Section 4.2.3) and in $7 + 1$ mode only ped_n is available, whereas

$$ped_{n-1} = ped_{n+1} = 0. \tag{9.2}$$

Therefore the PeakFinder cannot be simulated correctly, since not all necessary information is available. As the simulation effectively checks if

$$S_{n+1} \leq S_n - ped_n > S_{n-1} \tag{9.3}$$

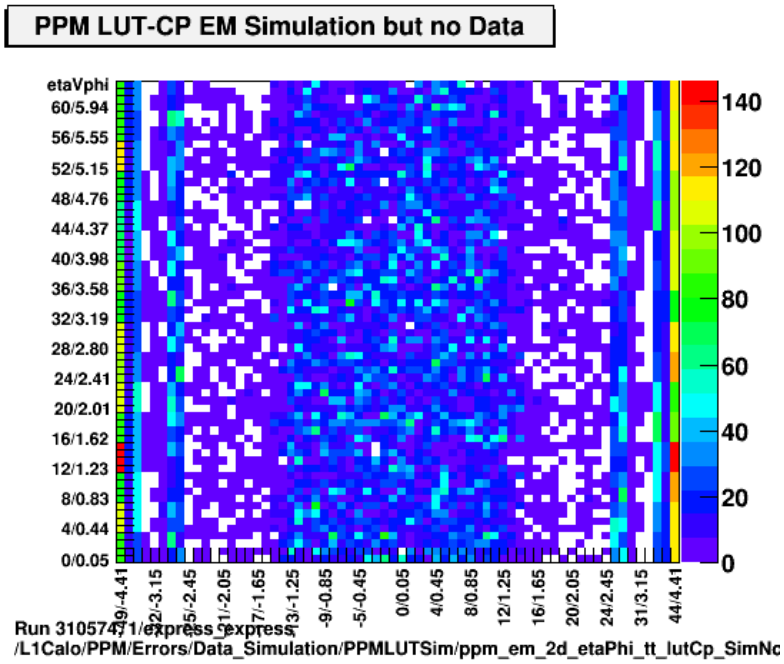

Figure 9.5: η-ϕ map of the electromagnetic layer showing the number of "LUT-CP simulation but no data" errors per trigger tower.

it is quite likely that it does not take the correct decision (n) for $ped_n > 0$. This explains the errors in Figure 9.4 and Figure 9.5. In the first case (data non-zero, simulation zero), the simulated PeakFinder identifies a different BC than the real PeakFinder in the hardware. However one would not expect the simulation to always calculate a LUT value of zero, but rather a non-zero LUT value different from the one found in data. This is a second bug in the simulation. In cases where the PeakFinder BCID is different in simulation and hardware, the LUT variable is initialized as $LUT = 0$ and never filled. The second case (data zero, simulation non-zero) is more complicated. Here one needs to remember that the simulation runs over all trigger towers in the event, not only the one that caused the trigger. Some trigger towers contain pulses which originate from background or noise and do not peak on the correct BC. Hence for these pulses the PeakFinder doesn't fire on the BC the event was triggered on. Since a LUT value for a tower is only read out, if a BCID algorithm triggered for the tower, the LUT value in data is zero. The simulated PeakFinder "mis-identifies" the BC for these pulses and finds it to be identical to the BC that triggered the event and calculates a LUT value. This causes the LUT mismatch. Both bugs were fixed in the code and the monitoring simulation is now performing correctly in $7+1$ readout. The PeakFinder is now only simulated, if at least seven ADC samples and three pedestal correction values are available.

9.2.2 Activation of Sat80

Near the end of the 2016 data taking during run 310 473 the Sat80 algorithm was activated for active triggering and replaced the Sat40. In the same run BCID simulation errors appeared.

They are shown in Figure 9.6.

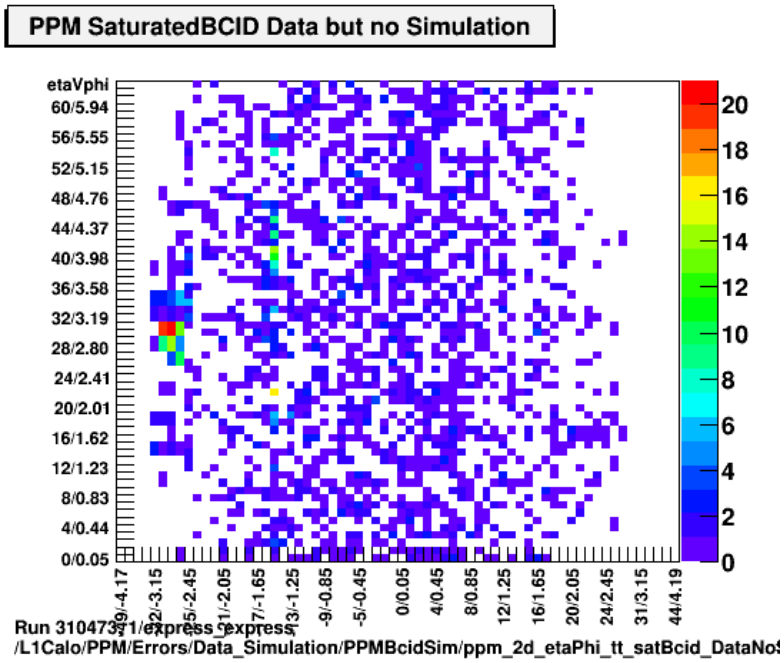

Figure 9.6: η-ϕ map of the electromagnetic layer showing the number of "Saturated BCID data but no simulation" errors per trigger tower.

These errors appear when the simulated saturated BCID algorithm and the saturated BCID algorithm running in the hardware do not agree. In this case the simulated algorithm is the Sat40, while the algorithm in data is the Sat80. All errors that appear are of the "Data but no Simulation" type. They are caused by the differences between Sat40 and Sat80. While the Sat80 can trigger correctly on pulses with the BC in the first saturated sample (s-case, c.f. Section 4.2.1), the Sat40, in its current configuration, can only trigger pulses with the BC in the second saturated sample ($s + 1$-case). In this sense these are "good" simulation errors, since they show the improved performance of the Sat80 as compared to the Sat40. Since the Sat80 cannot be simulated as described above, the monitoring has been modified such that the saturated BCID simulation is disabled when the Sat80 is active.

9.2.3 Pedestal Correction Overflow

Further simulation errors occured during another special run with an unusual pile-up situation. The run was divided in a low pile-up and a high pile-up part. For the low pile-up part matched FIR filters were loaded. Since a change of filters during a run is difficult they were also kept for the high pile-up part, where autocorrelation FIR filters would be optimal (c.f. Section 4.2.1).

All errors are non-zero LUT mismatches, which means that the simulation and the harware calculated different LUT outputs. An η-ϕ map of the errors is shown in Figure 9.7.

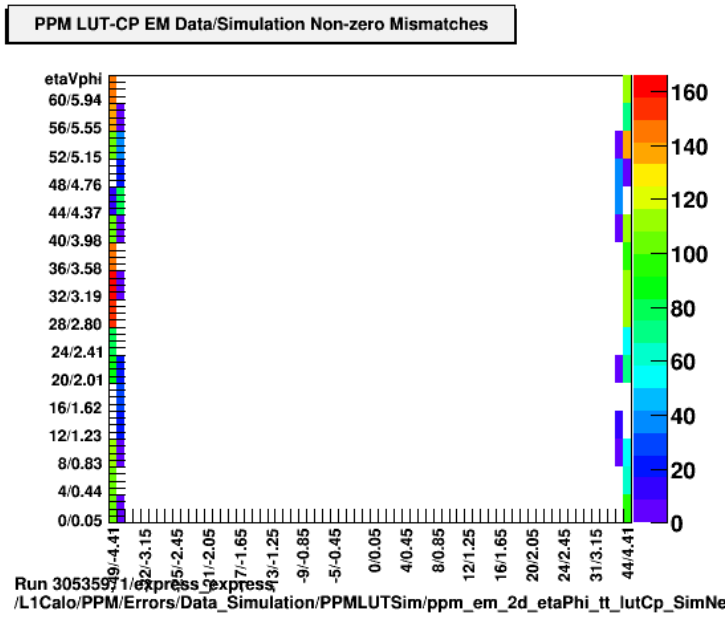

Figure 9.7: η-ϕ map of the electromagnetic layer showing the number of "LUT-CP data/simulation non-zero mismatch" errors per trigger tower. The errors only appear in the forward calorimeter region.

All errors appear during the high pile-up part of the run in the very forward detector region in the FCAL, where the pile-up is largest. However it was found that all calculations done by the simulation are correct, so the errors must be caused by incorrect input data to the simulation. An exctracted event showed that the pedestal correction in several towers in the forward region is exactly 511 and that this value is never exceeded. A map of the pedestal correction is shown in Figure 9.8. Indeed it is the case that while the pedestal correction is a 16 bit number for internal calculations of the hardware, in the detector readout that is also used for the simulation it is restricted to 9 bit, to reduce the amount of information that has to be read out. This corresponds to a range of ped =−512 to 511. The LUT input is given by

$$LUT_{\text{in}} = S_n - ped_n, \tag{9.4}$$

with S_n the FIR sum. If the pedestal correction ped_n becomes larger than 511 then

$$LUT_{\text{in,Simulation}} \neq LUT_{\text{in,Hardware}} \tag{9.5}$$

and since the LUT is strictly monotonous it follows that

$$LUT_{\text{out,Simulation}} \neq LUT_{\text{out,Hardware}}. \tag{9.6}$$

This explains the simulation errors during this special run. The overflow of the pedestal correction is not observed during "normal" physics running, where autocorrelation FIR filters are used. These filters compensate much better for the pile-up than the matched filters and lead to a smaller pedestal correction.

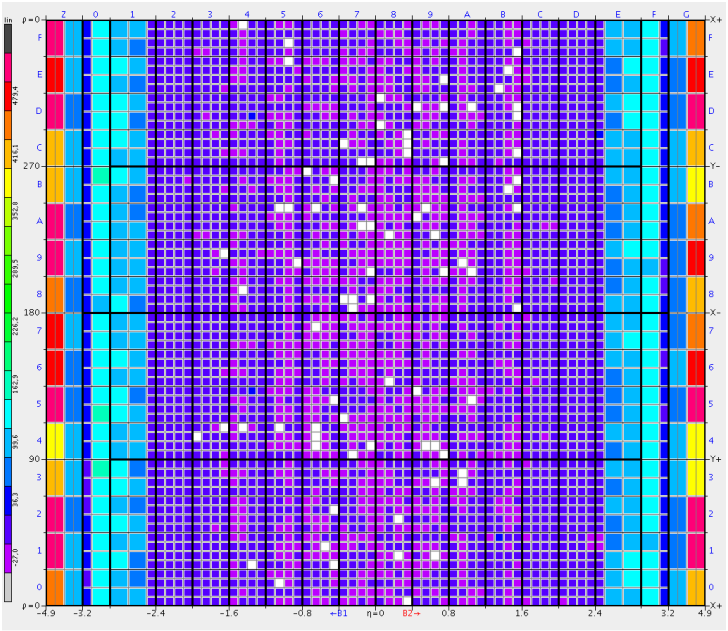

Figure 9.8: η-ϕ map of the electromagnetic layer showing the value of the pedestal correction. For several towers in the FCAL the pedestal correction saturates at 511.

To fix the simulation errors in future runs with high pile-up and matched filters, the LUT simulation is now disabled for towers with $ped = 511$ or $ped = -512$. In addition histograms were added to the L1Calo monitoring that are filled if the pedestal correction overflows (underflows). An example of such a histogram is shown in Figure 9.9. It demonstrates that the overflow happens in the forward region, where the pile-up is highest.

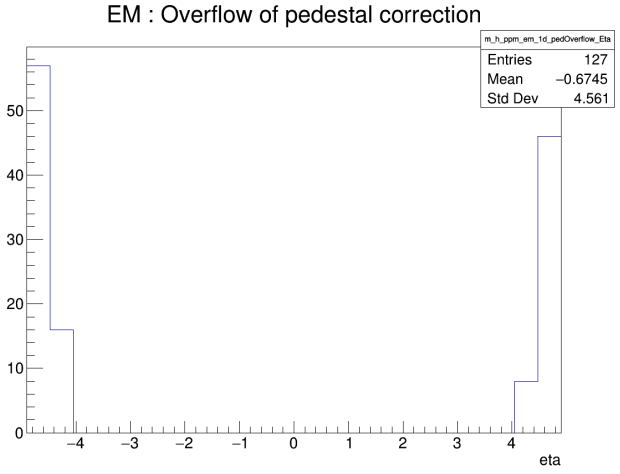

Figure 9.9: Monitoring of the pedestal overflow as a function of η.

10 Summary

The ATLAS detector at the Large Hadron Collider has a very efficient trigger system. It reduces the input rate of collision events by a factor of 10^6 to an output rate of 1 kHz which is recorded to permanent storage. The trigger selects those events that are interesting for physics analysis and might lead to new discoveries. The Level-1 Calorimeter Trigger is one of the main components of the ATLAS trigger system. It operates on calorimeter information with reduced granularity and identifies significant energy depositions. It relies on the association of the calorimeter signals to the correct bunch-crossing. This crucial process is called bunch-crossing identification. It ensures that the detector information is read out for the event that caused the trigger. For energies above 256 GeV, the analog-to-digital converters that digitize the calorimeter signals in the trigger start to saturate and information on the peak of the signal is lost. Two algorithms, the PeakFinder and the SatBCID, cover the full energy range for the bunch-crossing identification. The PeakFinder is optimized for non-saturated pulses but works also in light saturation, the SatBCID is optimized for saturated pulses.

In this thesis several studies of the bunch-crossing identification algorithms were performed. The misidentification of the bunch-crossing by the PeakFinder for several highly energetic physics events was investigated. This misidentification happened for strongly saturated pulses outside of the optimal regime of the PeakFinder. The critical energy where the PeakFinder is likely to fail was determined using energy depositions from electrons and photons in the calorimeter. The calorimeter regions where this energy is particularly low were identified.

The misidentifications by the PeakFinder were solved by improving the interplay between PeakFinder and SatBCID and deactivating the PeakFinder for highly saturated pulses. This was accomplished by the introduction of the "new decision logic" that decides which of the algorithms is active. The new decision logic was validated as part of this thesis for both the Liquid Argon and the Tile calorimeter. The validation uses calibration pulses injected in the calorimeter electronics. These pulses allow to test the bunch-crossing identification algorithms for very high energies. Due to the successful validation the new decision logic was activated in ATLAS data taking in the beginning of 2016 and reduced the rate of mistimed events from 36 events per fb^{-1} to approximately 1 event per fb^{-1}.

The remaining rate of mistimed events could be reduced to zero by the introduction of a new and improved algorithm for saturated calorimeter signals. This "enhanced SatBCID" was tested and studied in this thesis using the calibration pulses. It was discovered that the algorithm is sensitive to non-linearities in the pulse shape at high energies. These non-linearities are especially strong in calibration pulses and prevent the algorithm from performing a correct bunch-crossing identification.

A modified configuration for the algorithm was devised that takes the non-linearities into account. It could be shown that this modified configuration allows the algorithm to operate correctly over the whole energy range for calibration pulses.

Furthermore first studies on the linearity of physics pulses were conducted. These studies showed a slight non-linearity of the pulse shape. Due to insufficient statistics at high energies, further studies are needed, possibly using simulated pulses.

The enhanced SatBCID algorithm was activated for operation in October 2016. Since then no more mistriggered events were observed.

List of Figures

List of Tables

References

[1] Lyndon Evans and Philip Bryant. "LHC Machine". In: *Journal of Instrumentation* 3.08 (2008), S08001. URL: http://stacks.iop.org/1748-0221/3/i=08/a=S08001.

[2] Jean-Paul Burnet et al. *Fifty years of the CERN Proton Synchrotron: Volume 1*. Geneva: CERN, 2011. URL: http://cds.cern.ch/record/1359959.

[3] Simone Gilardoni et al. *Fifty years of the CERN Proton Synchrotron: Volume 2*. Comments: 58 pages, published as CERN Yellow Report https://cds.cern.ch/record/1597087?ln=en. Geneva: CERN, 2013. URL: http://cds.cern.ch/record/1597087.

[4] Django Manglunki et al. "Ions for LHC: Towards Completion of the Injector Chain". In: CERN-AB-2008-058 (Sept. 2008), 4 p. URL: http://cds.cern.ch/record/1124319.

[5] F Blas et al. "Conversion of the PS complex as LHC proton pre-injector". In: CERN-PS-97-048-DI (June 1997), 3 p. URL: https://cds.cern.ch/record/328735.

[6] Christiane Lefèvre. "The CERN accelerator complex. Complexe des accélérateurs du CERN". Dec. 2008. URL: https://cds.cern.ch/record/1260465.

[7] G Rumolo et al. "Expected performance in the injectors at 25 ns without and with Linac4". In: (2014). URL: https://cds.cern.ch/record/1977350.

[8] Gianluigi Arduini et al. "Status of the LHC proton beam in the CERN SPS". In: CERN-SL-2002-054-OP (June 2002), 3 p. URL: http://cds.cern.ch/record/593245.

[9] The ATLAS Collaboration et al. "The ATLAS Experiment at the CERN Large Hadron Collider". In: *Journal of Instrumentation* 3.08 (2008), S08003. URL: http://stacks.iop.org/1748-0221/3/i=08/a=S08003.

[10] The CMS Collaboration et al. "The CMS experiment at the CERN LHC". In: *Journal of Instrumentation* 3.08 (2008), S08004. URL: http://stacks.iop.org/1748-0221/3/i=08/a=S08004.

[11] G. Aad et al. "Observation of a new particle in the search for the Standard Model Higgs boson with the {ATLAS} detector at the {LHC}". In: *Physics Letters B* 716.1 (2012), pp. 1–29. ISSN: 0370-2693. DOI: http://dx.doi.org/10.1016/j.physletb.2012.08.020. URL: http://www.sciencedirect.com/science/article/pii/S037026931200857X.

[12] The ALICE Collaboration et al. "The ALICE experiment at the CERN LHC". In: *Journal of Instrumentation* 3.08 (2008), S08002. URL: http://stacks.iop.org/1748-0221/3/i=08/a=S08002.

[13] The LHCb Collaboration et al. "The LHCb Detector at the LHC". In: *Journal of Instrumentation* 3.08 (2008), S08005. URL: http://stacks.iop.org/1748-0221/3/i=08/a=S08005.

[14] Georges Aad et al. "The ATLAS Inner Detector commissioning and calibration". In: *Eur. Phys. J. C* 70.arXiv:1004.5293. CERN-PH-EP-2010-043 (June 2010). Comments: 34 pages, 25 figures, 787–821. 34 p. URL: https://cds.cern.ch/record/1262789.

[15] F. HÃ¼gging. “The {ATLAS} Pixel Insertable B-layer (IBL)”. In: *Nuclear Instruments and Methods in Physics Research Section A: Accelerators, Spectrometers, Detectors and Associated Equipment* 650.1 (2011). International Workshop on Semiconductor Pixel Detectors for Particles and Imaging 2010, pp. 45–49. ISSN: 0168-9002. DOI: http://dx.doi.org/10.1016/j.nima.2010.12.113. URL: http://www.sciencedirect.com/science/article/pii/S0168900210028937.

[16] A. Andronic and J.P. Wessels. “Transition radiation detectors”. In: *Nuclear Instruments and Methods in Physics Research Section A: Accelerators, Spectrometers, Detectors and Associated Equipment* 666 (2012). Advanced Instrumentation, pp. 130–147. ISSN: 0168-9002. DOI: http://dx.doi.org/10.1016/j.nima.2011.09.041. URL: http://www.sciencedirect.com/science/article/pii/S0168900211018134.

[17] Mark Thomson. *Modern particle physics*. eng. Hier auch später erschienene, unveränderte Nachdrucke. Cambridge [u.a.]: Cambridge University Press, 2013, XVI, 554 S. ISBN: 978-1-107-03426-6 and 1-107-03426-4.

[18] ATLAS Electromagnetic Liquid Argon Endcap Calorimeter Group et al. “Construction, assembly and tests of the ATLAS electromagnetic end-cap calorimeters”. In: *Journal of Instrumentation* 3.06 (2008), P06002. URL: http://stacks.iop.org/1748-0221/3/i=06/a=P06002.

[19] G. Aad et al. “Electron reconstruction and identification efficiency measurements with the ATLAS detector using the 2011 LHC proton–proton collision data”. In: *The European Physical Journal C* 74.7 (2014), p. 2941. ISSN: 1434-6052. DOI: 10.1140/epjc/s10052-014-2941-0. URL: http://dx.doi.org/10.1140/epjc/s10052-014-2941-0.

[20] G. Aad et al. “Readiness of the ATLAS liquid argon calorimeter forÂ LHCÂ collisions”. In: *The European Physical Journal C* 70.3 (2010), pp. 723–753. ISSN: 1434-6052. DOI: 10.1140/epjc/s10052-010-1354-y. URL: http://dx.doi.org/10.1140/epjc/s10052-010-1354-y.

[21] Bernardo Sotto-Maior Peralva. “Calibration and Performance of the ATLAS Tile Calorimeter”. In: *Proceedings, International School on High Energy Physics : Workshop on High Energy Physics in the near Future. (LISHEP 2013): Rio de Janeiro, Brazil, March 17-24, 2013*. 2013. arXiv: 1305.0550 [physics.ins-det]. URL: https://inspirehep.net/record/1231740/files/arXiv:1305.0550.pdf.

[22] A Artamonov et al. “The ATLAS Forward Calorimeter”. In: *Journal of Instrumentation* 3.02 (2008), P02010. URL: http://stacks.iop.org/1748-0221/3/i=02/a=P02010.

[23] The ATLAS collaboration. “Monitoring and data quality assessment of the ATLAS liquid argon calorimeter”. In: *Journal of Instrumentation* 9.07 (2014), P07024. URL: http://stacks.iop.org/1748-0221/9/i=07/a=P07024.

[24] The Liquid Argon Back End Electronics collaboration (A Bazan et al). “ATLAS liquid argon calorimeter back end electronics”. In: *Journal of Instrumentation* 2.06 (2007), P06002. URL: http://stacks.iop.org/1748-0221/2/i=06/a=P06002.

[25] N J Buchanan et al. "Design and implementation of the Front End Board for the readout of the ATLAS liquid argon calorimeters". In: *Journal of Instrumentation* 3.03 (2008), P03004. URL: http://stacks.iop.org/1748-0221/3/i=03/a=P03004.

[26] N J Buchanan et al. "ATLAS liquid argon calorimeter front end electronics". In: *Journal of Instrumentation* 3.09 (2008), P09003. URL: http://stacks.iop.org/1748-0221/3/i=09/a=P09003.

[27] H Abreu et al. "Performance of the electronic readout of the ATLAS liquid argon calorimeters". In: *Journal of Instrumentation* 5.09 (2010), P09003. URL: http://stacks.iop.org/1748-0221/5/i=09/a=P09003.

[28] Martin Aleksa et al. *ATLAS Combined Testbeam: Computation and Validation of the Electronic Calibration Constants for the Electromagnetic Calorimeter*. Tech. rep. ATL-LARG-PUB-2006-003. ATL-COM-LARG-2006-003. Geneva: CERN, Apr. 2006. URL: https://cds.cern.ch/record/942528.

[29] J. Colas et al. "Electronics calibration board for the {ATLAS} liquid argon calorimeters". In: *Nuclear Instruments and Methods in Physics Research Section A: Accelerators, Spectrometers, Detectors and Associated Equipment* 593.3 (2008), pp. 269–291. ISSN: 0168-9002. DOI: http://dx.doi.org/10.1016/j.nima.2008.05.031. URL: http://www.sciencedirect.com/science/article/pii/S0168900208007407.

[30] P Borgeaud et al. *The LArg Tower Builder Board: calculation, simulation, measurements*. Tech. rep. ATL-LARG-2002-001. Geneva: CERN, May 2002. URL: https://cds.cern.ch/record/685385.

[31] Georges Aad et al. *Technical Design Report for the Phase-I Upgrade of the ATLAS TDAQ System*. Tech. rep. CERN-LHCC-2013-018. ATLAS-TDR-023. Final version presented to December 2013 LHCC. Sept. 2013. URL: https://cds.cern.ch/record/1602235.

[32] R Achenbach et al. "The ATLAS Level-1 Calorimeter Trigger". In: *Journal of Instrumentation* 3.03 (2008), P03001. URL: http://stacks.iop.org/1748-0221/3/i=03/a=P03001.

[33] Andrew Daniells. "L1Calo Calibration for Run 2". In: *ATLAS TDAQ Week, Copenhagen*. 2014.

[34] DL Rees. *Bunch-Crossing Identification Design Issues*. Tech. rep. ATL-DAQ-97-071. ATL-D-PN-71. Geneva: CERN, Aug. 1997. URL: http://cds.cern.ch/record/685792.

[35] J Garvey and D Rees. *Bunch Crossing Identification for the ATLAS Level - 1 Calorimeter Trigger*. Tech. rep. ATL-DAQ-96-051. ATL-D-PN-51. Geneva: CERN, May 1996. URL: http://cds.cern.ch/record/685770.

[36] W.E. Cleland and E.G. Stern. "Signal processing considerations for liquid ionization calorimeters in a high rate environment". In: *Nuclear Instruments and Methods in Physics Research Section A: Accelerators, Spectrometers, Detectors and Associated Equipment* 338.2 (1994), pp. 467–497. ISSN: 0168-9002. DOI: http://dx.doi.org/10.1016/0168-9002(94)91332-3. URL: http://www.sciencedirect.com/science/article/pii/0168900294913323.

[37] Vasiliki Kouskoura et al. *L1Calo Performance Plots*. Tech. rep. ATL-COM-DAQ-2015-150. Geneva: CERN, Sept. 2015. URL: https://cds.cern.ch/record/2053123.

[38] Falk Bartels. "Kalibration des Finite-Impulse-Response-Filters im PreProcessor des ATLAS Level-1 Calorimeter Triggers für den LHC Run-2". Bachelorarbeit. Universität Heidelberg, 2015.

[39] N Morange et al. *Study and validation of the BCID of the L1Calo at very high transverse energies*. Tech. rep. ATL-COM-DAQ-2011-021. Geneva: CERN, Mar. 2011. URL: https://cds.cern.ch/record/1335085.

[40] K.A. Olive and Particle Data Group. "Review of Particle Physics". In: *Chinese Physics C* 38.9 (2014), p. 090001. URL: http://stacks.iop.org/1674-1137/38/i=9/a=090001.

[41] Claus Grupen and Boris A. Shwartz. *Particle detectors*. eng. 2nd ed. Cambridge monographs on particle physics, nuclear physics, and cosmology ARRAY(0x3f21e68). Previous ed.: published as by Claus Grupen with the cooperation of Armin Böhrer and Ludek Smolík. 1996. Cambridge [u.a.]: Cambridge University Press, 2008, XXIII, 651 S. ISBN: 0-521-84006-6 and 978-0-521-84006-4. URL: http://www.myilibrary.com?id=125440.

[42] Konrad Kleinknecht. *Detektoren für Teilchenstrahlung*. ger. 4., überarb. Aufl. Lehrbuch : Physik. Wiesbaden: Teubner, 2005, IX, 245 S. ISBN: 3-8351-0058-0 and 978-3-8351-0058-9. URL: http://deposit.ddb.de/cgi-bin/dokserv?id=2673865&prov=M&dok_var=1&dok_ext=htm.

[43] P. Adragna et al. "Measurement of pion and proton response and longitudinal shower profiles up to 20 nuclear interaction lengths with the {ATLAS} Tile calorimeter". In: *Nuclear Instruments and Methods in Physics Research Section A: Accelerators, Spectrometers, Detectors and Associated Equipment* 615.2 (2010), pp. 158–181. ISSN: 0168-9002. URL: http://www.sciencedirect.com/science/article/pii/S0168900210001051.

[44] Hans-Christian Schultz-Coulon. *The Physics of Particle Detectors*. 2011.

[45] Johanna Stachel. *The Physics of Particle Detectors*. 2014.

[46] W Lampl et al. *Calorimeter Clustering Algorithms: Description and Performance*. Tech. rep. ATL-LARG-PUB-2008-002. ATL-COM-LARG-2008-003. Geneva: CERN, Apr. 2008. URL: http://cds.cern.ch/record/1099735.

[47] *Electron efficiency measurements with the ATLAS detector using the 2015 LHC proton-proton collision data*. Tech. rep. ATLAS-CONF-2016-024. Geneva: CERN, June 2016. URL: https://cds.cern.ch/record/2157687.

[48] G. Aad et al. "Electron performance measurements with the ATLAS detector using the 2010 LHC proton-proton collision data". In: *The European Physical Journal C* 72.3 (2012), p. 1909. ISSN: 1434-6052. DOI: 10.1140/epjc/s10052-012-1909-1. URL: http://dx.doi.org/10.1140/epjc/s10052-012-1909-1.

[49] Morad Aaboud et al. *Measurement of the photon identification efficiencies with the ATLAS detector using LHC Run-1 data*. Tech. rep. CERN-EP-2016-110. arXiv:1606.01813. Comments: 40 pages plus author list (57 pages total), 17 figures, 2 tables, submitted to Eur. Phys. J. C, All figures including auxiliary figures are available at http://atlas.web.cern.ch/Atlas/GROUPS/PHYSICS/PAPERS/PERF-2013-04/. Geneva: CERN, June 2016. URL: https://cds.cern.ch/record/2158117.

[50] *Photon identification in 2015 ATLAS data*. Tech. rep. ATL-PHYS-PUB-2016-014. Geneva: CERN, Aug. 2016. URL: https://cds.cern.ch/record/2203125.

[51] Bernardo Sotto-Maior Peralva. *Calibration and Performance of the ATLAS Tile Calorimeter*. Tech. rep. arXiv:1305.0550. Comments: 4 pages, 7 figures, LISHEP 2013, 17-24 March 2013, Rio de Janeiro. May 2013. URL: https://cds.cern.ch/record/1545496.

[52] Claire Antel. *Personal Communication*. Private Communication.

[53] Jan Jongmanns. "Algorithmen für das neue Multichip-Modul des PräProzessors des ATLAS-Kalorimeter-Triggers". MA thesis. 2012.

[54] Andrei Khomich. *Personal Communication*.

[55] Laurence W. Nagel and D.O. Pederson. *SPICE (Simulation Program with Integrated Circuit Emphasis)*. Tech. rep. UCB/ERL M382. EECS Department, University of California, Berkeley, Apr. 1973. URL: http://www2.eecs.berkeley.edu/Pubs/TechRpts/1973/22871.html.

[56] D Charlton et al. *Sign-off Procedure for Bulk Data Reconstruction*. Tech. rep. ATL-COM-GEN-2008-002. Geneva: CERN, May 2008. URL: https://cds.cern.ch/record/1103504.

[57] Jan Jongmanns. *Personal Communication*.

Danksagung

An dieser Stelle möchte ich allen danken, die zum Gelingen dieser Arbeit beigetragen haben.

Zuerst gilt mein Dank meinem Betreuer Herrn Prof. Dr. Hans-Christian Schultz-Coulon, der mir die Durchführung dieser Arbeit im Rahmen des 4+4 Programms in seiner Forschungsgruppe ermöglichte. Dank seiner motivierenden Art und großzügigen Unterstützung kann ich auf ein erfolgreiches erstes Jahr zurückblicken, in dem ich sehr viel dazugelernt habe. Insbesondere danke ich ihm für meinen neunmonatigen Aufenthalt am CERN. Während dieser Zeit lernte ich viele interessante Menschen kennen und durfte am täglichen Betrieb von L1Calo mitwirken.

Weiterhin danke ich Frau Prof. Dr. Stephanie Hansmann-Menzemer für die Übernahme der Zweitkorrektur dieser Arbeit.

Mein besonderer Dank geht an Dr. Martin Wessels und Dr. Rainer Stamen für Ihre Betreuung und Unterstützung. Sie standen mir immer mit Rat und Tat zur Seite und hatten ein offenes Ohr für Fragen jeglicher Art – auch während meiner Zeit am CERN.

Außerdem möchte ich mich bei der kombinierten ATLAS+ILC Gruppe für die tolle Atmosphäre bedanken. Diese herrschte nicht nur während der Arbeit, bei Kaffeepausen und Meetings, sondern auch außerhalb bei zahlreichen gemeinsamen Unternehmungen. Besonders bedanken möchte ich mich bei Silvia, Jan, Claire, Hanno, Valerie und Julia für die produktive Zusammenarbeit, sowie das Probelesen meiner Arbeit und die hilfreichen Kommentare.

Pavel und Thomas danke ich für ihre Unterstützung bei der Administration der KIP ATLAS Rechnerfarm. Sie hielten mir während der Schreibphase den Rücken frei und das System am Laufen.

Meinen Freunden Lena, Michael, Nils und Stefanie danke ich für ihre Kommentare und Verbesserungsvorschlägen zu meiner Arbeit. Auch haben sie mich stets daran erinnert, dass es ein Leben außerhalb der Physik gibt.

Ganz besonders danke ich Stefanie für ihre Motivation und Geduld mit meinen teils unorthodoxen Arbeitszeiten. Meinen Eltern danke ich für die jahrelange, hingebungsvolle Unterstützung, die mich bis hierher getragen hat.

Erklärung:

Ich versichere, dass ich diese Arbeit selbstständig verfasst habe und keine anderen als die angegebenen Quellen und Hilfsmittel benutzt habe.

Heidelberg, den 23.12.2016 .....